



저작자표시-비영리-변경금지 2.0 대한민국

이용자는 아래의 조건을 따르는 경우에 한하여 자유롭게

- 이 저작물을 복제, 배포, 전송, 전시, 공연 및 방송할 수 있습니다.

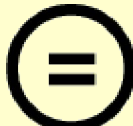
다음과 같은 조건을 따라야 합니다:



저작자표시. 귀하는 원 저작자를 표시하여야 합니다.



비영리. 귀하는 이 저작물을 영리 목적으로 이용할 수 없습니다.



변경금지. 귀하는 이 저작물을 개작, 변형 또는 가공할 수 없습니다.

- 귀하는, 이 저작물의 재이용이나 배포의 경우, 이 저작물에 적용된 이용허락조건을 명확하게 나타내어야 합니다.
- 저작권자로부터 별도의 허가를 받으면 이러한 조건들은 적용되지 않습니다.

저작권법에 따른 이용자의 권리와 책임은 위의 내용에 의하여 영향을 받지 않습니다.

이것은 [이용허락규약\(Legal Code\)](#)을 이해하기 쉽게 요약한 것입니다.

[Disclaimer](#)



Doctoral Dissertation

Development of an ultrashort deep- and
extreme ultraviolet beamline and its
application to photoelectron holography

Tsendsuren Khurelbaatar

Department of Physics

Pohang University of Science and Technology

2021



Development of an ultrashort deep- and extreme ultraviolet beamline and its application to photoelectron holography



Development of an ultrashort deep- and extreme ultraviolet beamline and its application to photoelectron holography

by

Tsendsuren Khurelbaatar

Department of Physics

Pohang University of Science and Technology

A dissertation submitted to the faculty of the Pohang University
of Science and Technology in partial fulfillment of the
requirements for the degree of Doctor of Philosophy in Physics

Pohang, Republic of Korea

07. 15. 2021

Approved by

Dong Eon Kim (Signature)

Academic advisor



Development of an ultrashort deep- and extreme ultraviolet beamline and its application to photoelectron holography

Tsendsuren Khurelbaatar

The undersigned have examined this dissertation and hereby
certify that it is worthy of acceptance for a doctoral degree from
POSTECH

07. 15. 2021

Committee Chair

김동언

(Seal)

Member

주태하

(Seal)

Member

신희득

(Seal)

Member

윤건수

(Seal)

Member

김승철

(Seal)



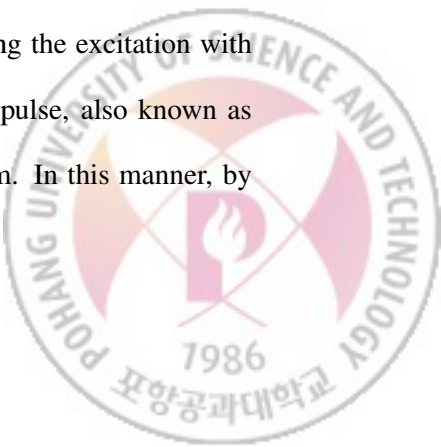
DPH Tsendsuren Khurelbaatar
20142396 Development of an ultrashort deep- and extreme ultraviolet
beamline and its application to photoelectron holography.

Department of Physics , 2021, 111p
Advisor: Dong Eon Kim.
Text in English.

ABSTRACT

Motion in the microcosm is extremely rapid. For instance, a chemical reaction can be completed in a few femtoseconds ($1 \text{ fs} = 10^{-15} \text{ s}$). Due to the extremely short time scale at which chemical reactions occur, only the initial and final products are known; the reaction pathways and intermediate products, on the other hand, remain unknown.

To observe these ultrafast processes on their time scales, science requires measurement technology that is faster than the processes to be observed. Development of ultrashort pulsed laser technology enabled the detection of these processes in real time. For example, the so-called "pump-probe" spectroscopy technique enables the tracking of ultrafast dynamics in atoms and molecules following the excitation with a short laser pulse called the pump pulse. A delayed second pulse, also known as the probe pulse, probes the current state of the evolving system. In this manner, by



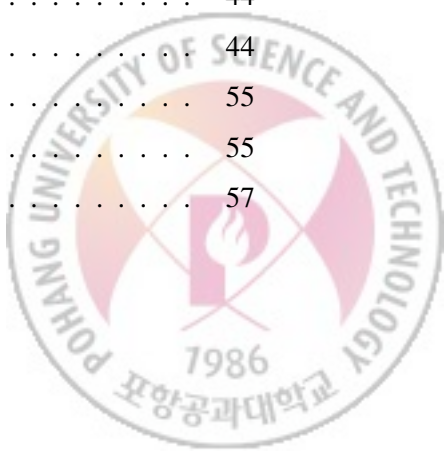
varying the time interval between the pump-probe pulses with multiple repetitions, a dynamical evolution of the system can be obtained. The available shortest pulse duration, however, was limited to capturing only nuclear dynamics with this technique. A new regime in ultrafast optical science called attosecond physics emerged at the turn of the 21st century. In the extreme ultraviolet regime, the high-order harmonic generation method has enabled previously unattainable ultrashort pulse durations of a few hundred attoseconds ($1 \text{ as} = 10^{-18} \text{ s}$).

Attosecond pulses enable us to probe dynamics beyond the Born-Oppenheimer approximation, in which electronic states are not stationary and influential. We need to investigate how nonstationary electronic states are coupled to nuclear motion and then understand how manipulating the electronic motion can be used to trigger the nuclei to move selectively, thereby implementing a chemical reaction pathway. To aid in our knowledge and control of ultrafast dynamics in a new paradigm, an intense few-cycle deep-ultraviolet beamline was built in conjunction with ultrashort near-infrared and extreme ultraviolet pulses enabling time-resolved studies using various combinations of these light sources.



Contents

I. Introduction	1
II. Fundamentals	3
2.1 Atoms in intense laser fields	3
2.2 Ultrashort laser pulses	6
III. Few-cycle pulse generation	12
3.1 Femtosecond oscillator	13
3.2 Multi-pass amplifier	14
3.3 Carrier-envelope-phase stabilization	16
3.3.1 Oscillator CEP	17
3.3.2 Amplifier CEP	19
3.4 Supercontinuum generation	22
3.4.1 Experimental setup	26
3.4.2 CEP after pulse compression	31
3.4.3 Pulse characterization	34
IV. Development of an ultrashort DUV/XUV beamline	38
4.1 Motivation	38
4.2 Design of the beamline	39
4.3 Third-order harmonic generation	44
4.3.1 Experiments	44
4.4 High-order harmonic generation	55
4.4.1 The simple man's model	55
4.4.2 Experiment	57

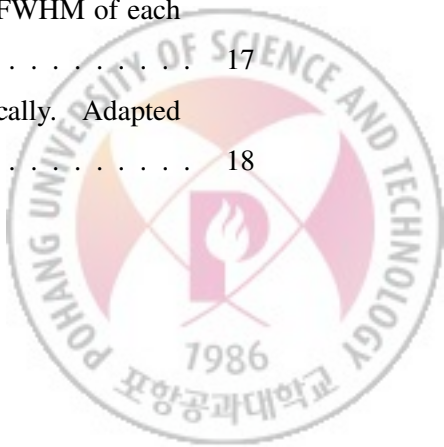


4.5	Delay-line setup for time-resolved experiments	60
4.5.1	Interferometer setup	63
4.5.2	Active phase stabilization	66
4.6	VMI spectrometer	73
4.6.1	Introduction	73
4.6.2	VMI spectrometer design	75
4.6.3	VMI spectrometer operation mode and alignment	77
4.6.4	VMI-TOF operation mode and calibration	79
V.	The beamline applications for photoelectron holography experiments	85
5.1	Motivation	85
5.2	PH experiments with a multicycle laser	86
5.3	PH experiments with a few-cycle laser	88
VI.	Conclusions and outlook	97
Summary (in Korean)		100
References		103

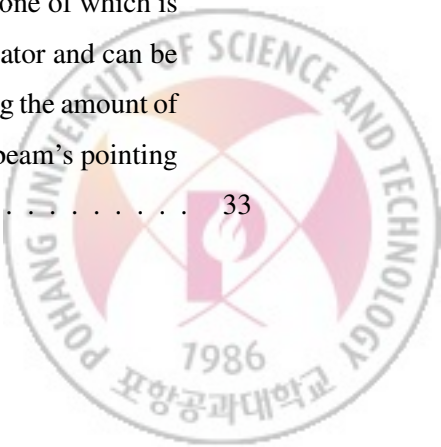


List of Figures

2.1 Ionization dynamics. The laser field has no discernible effect on the Coulomb potential in the perturbative regime ($\gamma > 1$), and (a) MPI or (b) ATI result in photoionization via multiple photon absorption (red arrows). In the strong field regime ($\gamma < 1$), the Coulomb potential is distorted significantly by the laser field, allowing (c) tunnel ionization or (d) OTBI to occur.	6
3.1 The chirped pulse amplification (CPA) method is illustrated schematically. The output of the ultrashort but low energy seed oscillator is time stretched and amplified with a multipass amplifier. The resulting high energy, relatively long pulse is recompressed using a grating compressor. It produces a high-energy, short pulse in the NIR spectral domain.	12
3.2 The 3 mJ, 3 kHz multipass laser amplifier system.	15
3.3 The output spectrum of the femtosecond oscillator is shown alongside the output spectrum of the amplifier with the central wavelength of 790 nm. The oscillator spectrum's bandwidth supports pulses with a duration of less than 7 fs, whereas the amplified output spectrum supports only pulses with a duration of 28 fs.	16
3.4 Pulse trains emerging from the femtosecond oscillator with different CEP. Left to right; 0, $\pi/2$, π , $3\pi/2$ respectively. The FWHM of each pulse is 4 fs.	17
3.5 The self-referencing technique is depicted schematically. Adapted from Ref. [16]	18



3.6	The schematic setup of the f-to-2f interferometer. Adapted from Femtopower HE/HR laser user manual (Femtolasers GmbH).	20
3.7	Amplifier CEP measurement and stabilization. The average amplifier CEP drift is less than 250 mrad RMS over 3 hours of measurement.	21
3.8	Pulse propagation simulations at various propagation distances. The left panel, shows the spectra, while the right panel depicts FTL pulses generated by the spectra. SPM and SS were both taken into account in the simulation.	25
3.9	Supercontinuum generation setup. Inside the chamber, a 100 cm long, 400 μm inner diameter HCF is installed and filled with 3 bar neon gas. Before the entrance, a beam position locking system is implemented, and after the HCF setup, a pulse compression setup is shown.	27
3.10	A glass tube was installed near the laser-fiber coupling. By looking through the glass tube, the laser can be safely coupled to the fiber. Plasma formation in front of the fiber tip is also shown, which must be avoided at all times.	28
3.11	Experimental and simulated supercontinuum generation output spectra. The spectrum supports sub-4 fs pulse duration.	29
3.12	Few-cycle pulse compression scheme.	30
3.13	F-to-2f interferometer configuration. The wedge's reflection is picked up and routed into the setup for measuring CEP jitter. HWP: half-wave plate	32
3.14	Spectral interference fringes are used to extract CEP information.	32
3.15	The piezo stretcher actuator is used to compensate for the amplifier system's CEP drift. It is made up of two glass prisms, one of which is fixed and the other of which is attached to a piezo actuator and can be moved relative to the other prism. This enables changing the amount of glass material (dispersion) without changing the laser beam's pointing or beam parameters.	33

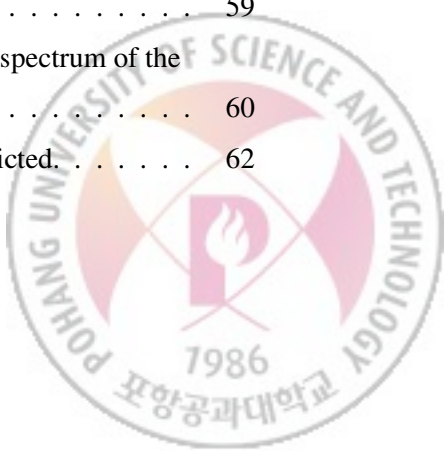


3.16 Dispersion scan setup. Ultrashort pulses are sent to an ultrathin (5 μm) BBO crystal and the generated SHG signal is measured with a spectrometer while the dispersion is scanned. The dispersion scan was performed using a glass wedge in the beam path.	34
3.17 D-scan measurement of a few-cycle waveform generated by a hollow-core fiber statically filled with Ne at 3.0 bar. (a) Measured trace (b) Retrieved trace. (c) Corresponding spectrum (black) and the reconstructed spectral phase (blue). The spectrum spans from 450 to 950 nm and supports a Fourier transform-limited pulse duration of 3.3 fs. (d) Reconstructed intensity envelope (solid curve) exhibiting a pulse duration of 3.4 fs. The reconstructed envelope is nearly identical to the Fourier transform-limited envelope (dashed curve).	36
3.18 Reconstructed electric field of a few-cycle waveform (solid curve) with a period of only 3.4 fs (\sim 1.2 optical cycles) and its field envelope (dashed curve).	37
4.1 Layout of the experimental setup. A scheme for collinear generation is illustrated, as well as a method for active stabilization. The upper-layer contains a reference in-loop (IL) interferometer for active phase stabilization: the lower-layer contains the main interferometer for the pump-probe experiment using a DUV and XUV beam. THG: Third-order harmonic generation, HHG: High-order harmonic generation, DBS: dichroic beam splitter, BS: He-Ne beamsplitter, M: silver mirror, RM: triple rhodium mirror (75° angle of incidence per segment), DM: dichroic mirror, TM: Toroidal mirror, HWP: Half-wave plate, QWP: Quarter wave plate, PD: Photodiode	40
4.2 Schematic illustration of the source chamber. The gas cell for THG and HHG is housed in a small chamber, nested inside a larger main chamber. TMP: turbo molecular pump	41

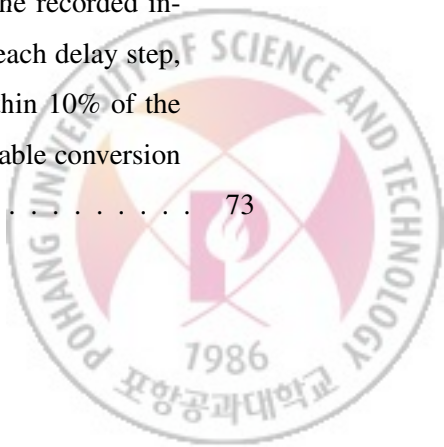
4.3	Ceramic gas cell for the THG and HHG experiment.	42
4.4	(a) Schematic experimental setup. A gas cell for THG is housed in a small chamber, nested inside a larger main chamber. (b) Geometry of the laser beam near the focus. z_0 represents the gas cell position. A negative z_0 value means the gas cell is positioned before the laser focus and vice versa. The laser focus is at $z_0 = 0$ mm	45
4.5	(a) Spectra of NIR laser before and after transmission through the gas cell, measured when the gas cell was positioned at the tightest focus position. The gas cell was supplied with argon gas. The transmitted NIR spectrum is showing a spectral blueshift (higher photon energy). (b) Mean photon energies of the transmitted NIR laser as a function of the cell position. The amount of blueshift was used to determine the best focus position $z_0 = 0$ mm, which is 18.25 mm stage position. . .	46
4.6	DUV pulse energies and spectra versus gas cell position relative to the laser focus: (a), (c) Ne gas and (b), (d) Ar gas. DUV pulse energies at the best gas cell position for different gas pressures: (e) Ne and (f) Ar.	48
4.7	Neutral density and THG yield. (a) and (b) show the variation of neutral-atomic densities and laser intensity for different cell positions. (c) and (d) are estimated THG yields, indicating that the maximum deep-UV yield is expected when the cell is placed off the laser focus in the case of Ar. For Ne (a), 25% of the neutral atoms are expected to be ionized when the cell is positioned at the laser focus. For Ar (b), the neutral atoms are totally depleted.	49
4.8	Power logging of the generated DUV is shown. During the 30-min measurement, pulse energy stability was less than 2% (RMS).	50



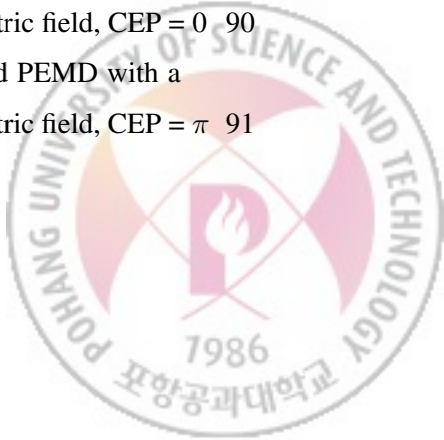
4.9	(a) and (c) experimental spectra taken at the dashed lines in Figs. 4.6 (c) and (d), respectively. (b) and (d) DUV spectra obtained from the simulation performed using the experimentally observed laser parameters. More details on the simulation results are given in Fig. 4.10. The dashed lines in (b) and (d) show an analytical solution of the third-harmonic spectrum obtained by Fourier transforming the cube of the fundamental laser $E(t)$ in the temporal domain.	52
4.10	Simulated nonlinear DUV generation dynamics in Ar. The left column [(a), (b), (c), and (d)] and the right column [(e), (f), (g), and (h)] panels are the results for the two different cell positions: $z_0 = -14$ mm and $+14$ mm, respectively. (a) and (e) show the z -dependent on-axis ($r = 0$) electron densities after the laser has passed. (b) and (f) are the two-dimensional (r and z) electron density profiles. The spectra of propagating fundamental [(c) and (g)] and the third-order harmonic [(d) and (h)] were taken from the on-axis ($r = 0$). In (c) and (g), the mean photon energies of the fundamental laser are indicated by the dashed lines in order to visualize the blueshift.	54
4.11	The three-step simple man's model, which includes tunnel ionization, free acceleration, and high-energy photon emission upon recombination.	56
4.12	Schematic drawing of the interaction chamber. A VMI and a flat-field grating spectrometer are shown. The XUV beam is indicated by the violet color.	58
4.13	Generated HHG spectrum measured in the interaction chamber with two different filters. An Al filter is used to calibrate the HHG spectrum using its well known absorption edge.	59
4.14	(a) Driving few-cycle NIR laser spectrum. (b) Energy spectrum of the generated DUV and (c) XUV light.	60
4.15	The vibration isolation technique is schematically depicted.	62



4.16 Noise sources in the laboratory. With the frequency domain analysis, noise sources can be identified using a conventional interferometer. The most significant noise contribution comes from prominent characteristic peaks at 60 Hz (mains line) and 30 Hz (scroll pump) as well as slow temperature-induced drift below 1 mHz.	63
4.17 (a) Custom-designed coupled Al mirror mount for the double-layer interferometer setup. (b) Actively-stabilized continuous delay scan scheme based on Pancharatnam's phase in the upper-layer (reference) interferometer. BS: beamsplitter, PZT: piezoelectric transducer stage, PD: photodiode, POL: polarizer, PID: proportional-integral-derivative controller, RCP: right-handed circular polarization, LCP: left-handed circular polarization.	66
4.18 Frequency-domain analysis of the optical delay timing jitter and drift. (a) Power spectral density of the timing drift for the upper layer (red), lower layer (OOL) with PID control (blue), and lower layer (OOL) without PID control (green). The instrument noise floor for the respective interferometers is shown in lighter colors. (b) Integrated timing jitter calculated from the PSD shown in (a). Temperature-related long-term drift is notable below \sim 0.4 mHz.	69
4.19 Time-domain measurement of the drift, which is significantly reduced by the active stabilization on longer time scales.	71
4.20 Phase-locked delay scan and stability of the double-layer interferometer over an optical delay range of 200 fs. (a) Normalized fringe amplitude in the lower-layer interferometer as a function of optical delay. (b) Timing jitter calculated from the fluctuations in the recorded interference signal within 2 s of measurement time for each delay step, yielding an average of 12.9 as RMS. Data points within 10% of the interference extrema have been removed due to unreliable conversion between amplitude and timing.	73



4.21 Conceptual and actual VMI setup is depicted. (a) Conceptual VMI design. (b) Actual VMI setup developed and used in the chemical physics beamline. Adapted from Ref. [57]	76
4.22 Imaging in spatial and VMI modes. ATI photoelectrons from xenon gas imaged in (a) spatial mode. (b) PEMD from molecular oxygen is recorded (raw data) in VMI mode when photoionized with a few-cycle NIR laser field. ATI peaks along the laser polarization axis such as those in (b) are useful for VMI energy calibration.	78
4.23 Examples of waveform averaging with different numbers of averaging using multi-record feature in the ADQ14 digitizer. (a) No averaging applied, raw data. (b) 10-waveforms averaged. (c) 50-waveforms averaged.	80
4.24 TOF and mass-to-charge ratio relation calculated from the experimental result. The calibration coefficient (k) was found to be 0.7850. . . .	82
4.25 Mass spectrum of molecular nitrogen (N_2). Molecular ion signals N^{2+} , N^+ , N_2^+ are identified along with other residual gas ion signals in the interaction chamber.	83
4.26 Measured mass spectrum from the PENNA molecule when irradiated with a few-cycle NIR laser.	84
 5.1 N_2 PEMD with a multicycle laser pulse. (a) Measured PEMD with a 30-fs NIR laser field. (b) Simulated driving laser electric field	87
5.2 TDSE simulation of N_2 PEMD with a multicycle laser pulse. (a) Parallel aligned. (b) Alignment averaged.	88
5.3 N_2 PEMD with a few-cycle laser pulse. (a) Measured PEMD with a 3.4-fs NIR laser field. (b) Simulated driving laser electric field, CEP = 0	90
5.4 N_2 PEMD with a few-cycle laser pulse. (a) Measured PEMD with a 3.4-fs NIR laser field. (b) Simulated driving laser electric field, CEP = π	91



5.5 N ₂ PEMD with a few-cycle laser pulse. (a) Measured PEMD with a 3.4-fs NIR laser field. (b) Simulated driving laser electric field, CEP = $\pi/2$	92
5.6 TDSE simulation of N ₂ PEMD with a few-cycle laser pulse. (a) CEP = 0. (b) CEP = $\pi/2$	93
5.7 SFA simulation of N ₂ PEMD with a few-cycle laser pulse CEP = 0. (a) Direct and rescattering orbits. (b) Direct orbits only.	94
5.8 SFA simulation of N ₂ PEMD with a few-cycle laser pulse CEP = $\pi/2$. (a) Direct and rescattering orbits. (b) Direct orbits only.	95
5.9 Relevant electron trajectories are shown when the (a) CEP = 0, (b) CEP = $\pi/2$. Forward-rescattering electron trajectories resulting in a asymmetric PEMD. Contributions from back-rescattering electron trajectories are negligible.	96



I. Introduction

Spectroscopy is a fundamental technique for extracting information from atoms and molecules and in general, it can be categorized into static and dynamic. In static spectroscopy, the structure of the matter can be identified by measuring the absorbed or emitted frequency spectrum ($\omega_{ij} = (E_i - E_j)/\hbar$) of the electromagnetic radiation by comparison with theoretical predictions. Depending on the measured frequency, where it appears in the electromagnetic spectrum, conventional names are given; microwave, optical or x-ray spectroscopy etc. On the other hand, it is intriguing to reveal not only the matter structure itself, but also their dynamical change.

Generally, the timescale over which ultrafast processes evolve during these dynamical and structural changes is determined by the excitation energy of the system. One of quantum mechanics' most fundamental laws, the time-energy uncertainty principle connects the duration of a time interval Δt during which a transition between two quantum states to their separation by an energetic gap ΔE ,

$$\Delta t \approx \frac{\hbar}{(E_i - E_j)} = \frac{\hbar}{\Delta E} \quad (1.1)$$

where ΔE is the energy difference between the two eigenstates. The larger the energy separation between the two eigenstates, the faster is the particle's motion in the superposition state. The energy spacing and the change from one state to another are closely connected with the absorption and emission of photons. For a simple diatomic molecule, this scheme indicates that the rotational, vibrational, and electronic levels cover large energy ranges from a few μeV up to several eV, and the corresponding transition times extend between picoseconds and attoseconds.

Ahmed Zewail received the 1999 Nobel Prize in Chemistry for his work on studying nuclear dynamics during chemical reactions using ultrashort laser pulses with the "pump-probe" technique. However, electron dynamics within molecules and con-

densed matter are faster than even nuclear rearrangements of molecules, and are responsible for a wide variety of important phenomena in nature.

Due to the fact that the majority of a molecule's chemical activity is derived from its most loosely bound valence electrons, it is critical to track these most reactive regions of the electron density. To investigate such purely electronic motion prior to its coupling to nuclear dynamics, it is critical to realize the concept of sudden ionization. Attosecond laser sources are capable of delivering the extreme time resolution required to observe ultrafast processes in atoms and molecules. However, the use of extreme ultraviolet (XUV) ionizing radiation in the first step may prevent studying neutral states and on the other hand, the majority of attosecond laser sources are used in conjunction with femtosecond near-infrared (NIR) lasers. By inducing a multi-photon process, the involvement of an NIR laser in the ionization process results in the failure of the sudden ionization approximation. In contrast to the NIR laser, ultrashort UV and XUV pulses can approximate sudden ionization. Thus, with these ultrashort UV and XUV pulses, by tracking the instantaneous positions of the atomic nuclei and the electron density associated with the valence electrons, one can gain complete access to the chemically relevant dynamical changes of the target molecule. As a result, ultrashort UV and XUV pulses are highly desirable light sources for inclusion in ultrafast laser spectroscopy.



II. Fundamentals

2.1 Atoms in intense laser fields

Albert Einstein introduced the concept of light quanta or photons in 1905 with his seminal work on the photoelectric effect in metals. According to his formulation, the kinetic energy of photo-electrons emitted from a metal surface increased linearly with the frequency of light, but not with the intensity of light.

$$\hbar\omega = E_I + \frac{1}{2}mv^2 \quad (2.1)$$

where \hbar is the Planck constant, ω is the angular frequency of light, E_I is the ionization energy of the atom. This description of the phenomenon is adequate at low intensities, where the electric field strength is significantly less than the Coulomb fields that bind the electrons to the nucleus, and can be considered a weak perturbation. The invention of lasers and subsequent developments made it possible to study light-matter interactions at high intensities. When the laser intensity is sufficiently high, atoms can absorb more than two photons simultaneously and undergo a transition from the bound state to the higher lying continuum state (see Fig 2.1 (a)). This process is called *multi-photon ionization* (MPI). The first MPI was observed in 1965 by Delone and Voronov [1] where they focused 694.3 nm (1.78 eV) laser pulses into xenon gas ($E_I = 12.13$ eV), thus 7 photons were required for the ionization.

$$7\hbar\omega = E_I + \frac{1}{2}mv^2 \quad (2.2)$$

In a perturbative treatment, the n -photon ionization rate Γ_n is proportional to the n -th power I^n of the laser intensity I .

$$\Gamma_n = \sigma_n \cdot I^n \quad (2.3)$$

where n is the number of photons, I is the laser intensity and σ_n is the generalized n -photon ionization cross-section. The cross-section depends upon the medium and decreases as the number of photons (or intensity) required for multiphoton ionization increases. If the laser intensity is increased even further, similar to the MPI process, the atomic or molecular system can absorb more photons than the minimum number required to reach the ionization threshold ($n\hbar\omega \geq E_I$). After passing through the ionization threshold, the excess photon energies can be converted to photoelectron kinetic energy, with the increase in photoelectron kinetic energy being proportional to the laser intensity (see Fig 2.1 (b)). However, this increase will be discrete in nature, consisting of multiple integers of the single photon energy ($n\hbar\omega$). These processes are called *above-threshold ionization* (ATI) [2]. When the laser intensity is increased further ($I > 10^{13} \text{ W/cm}^2$), the field amplitude increases to the point where it is comparable to the Coulomb potential of an atom. In this case, an electron can tunnel ionized through a distorted potential barrier and thus set free itself in the continuum state (see Fig 2.1 (c)). With increasing laser intensity, the electric field's distortion of the potential can become so strong that the electron perceives no potential barrier and is thus free to leave the parent atom (see Fig 2.1 (d)), a process known as *over-the-barrier ionization* (OTBI). The Keldysh parameter (γ) can be used to distinguish between the previously mentioned processes and determine which mechanism will prevail [3]. The Keldysh parameter is given by:

$$\gamma = \sqrt{\frac{E_I}{2U_p}} \quad (2.4)$$

where E_I is an ionization energy and U_p is ponderomotive energy. When the electron is assumed to be weakly bound, then in the presence of the external laser field ($E = E_0 \cos \omega t$), these bound electrons can oscillate at the frequency ω of this field. The corresponding kinetic energy of this quivering motion is called "ponderomotive energy" (U_p) and is given by

$$U_p = \frac{q^2 E_0^2}{4m\omega^2} \quad (2.5)$$

where q is the electron charge and E_0 the laser field amplitude. U_p is proportional to the laser intensity and to the square of the laser wavelength ($\lambda = 2\pi c/\omega$) [4].

If the ponderomotive energy is much larger than the ionization energy ($U_p \gg E_I$), the Keldysh parameter becomes $\gamma \ll 1$ and tunnel ionization is the dominant process. Inversely, when the ponderomotive energy is much smaller than the ionization energy ($U_p \ll E_I$), the Keldysh parameter becomes $\gamma \gg 1$, meaning that MPI and ATI will be the dominant process.



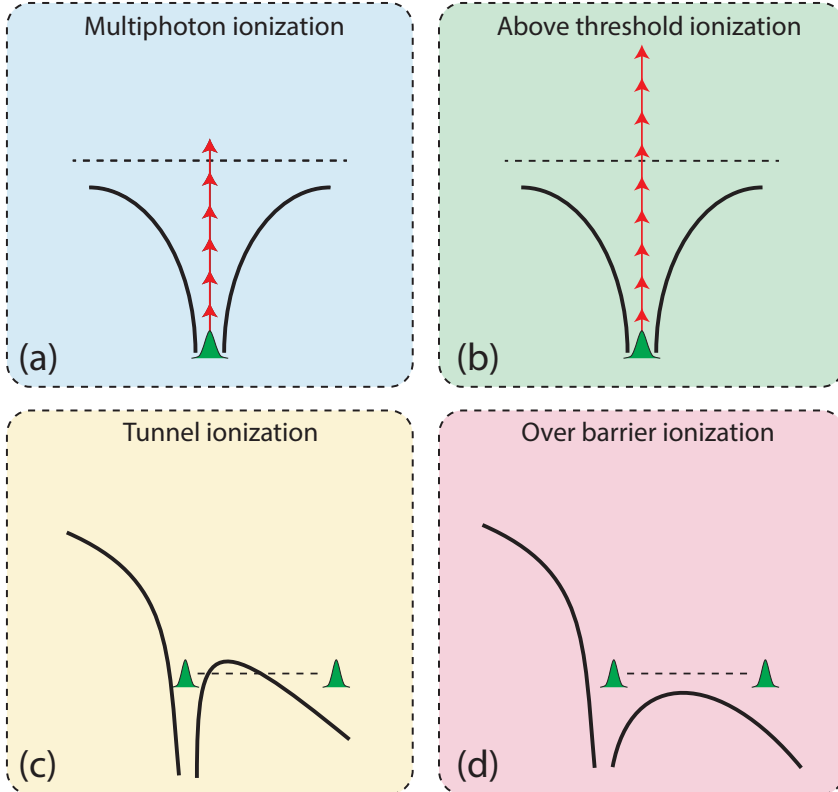
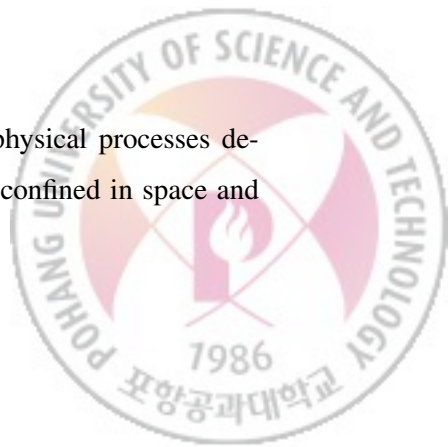


Figure 2.1: Ionization dynamics. The laser field has no discernible effect on the Coulomb potential in the perturbative regime ($\gamma > 1$), and (a) MPI or (b) ATI result in photoionization via multiple photon absorption (red arrows). In the strong field regime ($\gamma < 1$), the Coulomb potential is distorted significantly by the laser field, allowing (c) tunnel ionization or (d) OTBI to occur.

2.2 Ultrashort laser pulses

To achieve the high intensities required to observe the physical processes described in this thesis, the laser pulse energy must be strongly confined in space and



time. Confinement in space is easily accomplished using focusing optics such as a lens or spherical mirror. Whereas confinement in time is a challenging task that has taken decades to accomplish. The advancement of laser technology over the last few decades enabled the generation of intense and ultrashort laser pulses with the duration of few-fs [5], making it much easier to achieve laser intensities of $\sim 10^{14}$ - 10^{15} W/cm². For example, focusing a few-femtosecond ultrashort laser pulse with the pulse energy of a few hundreds of microjoules into a beam waist on the order of 50 μm , leads to intensities in the range of $\sim 10^{15}$ W/cm². This laser field is then on the order of $\sim 10^{10}$ V/m and becomes comparable to the Coulomb field. Before proceeding to the experimental realization of ultrashort laser pulses, we will briefly review the mathematical description of the laser field and relevant aspects.

A short pulse can be obtained mathematically by superimposing hundreds of continuous sinusoidal waves over a wide frequency range, which is defined as the bandwidth. Each of these waves has a distinct phase, which will be discussed in greater detail below. Any optical light field can be described using a time-dependent envelope or amplitude function, as well as a phase factor containing the carrier frequency and temporal phase [6].

$$E(t) = A(t)e^{i(\omega t + \phi(t))} \quad (2.6)$$

where $A(t)$ is the carrier envelope function, ω is the angular frequency of the carrier and $\phi(t)$ is the averaged phase evolution. Only the temporal aspects of the electric field are discussed in this section, whereas the spatial components of the electric field are ignored. When all of the wavelengths are in phase with each other, it results in constructive interference in a short period of time. In this way, a mathematical laser pulse can be obtained at its shortest duration and $\phi(t) = \phi_0$, where ϕ_0 is known as the carrier-envelope phase (CEP). This is the phase offset between the envelope and the carrier wave. As discussed previously, laser intensity is a critical quantity in determining physical processes when light interacts with matter, and it is proportional to the square of the amplitude of the electric field's envelope, $I(t) \propto |E(t)|^2$. From

an experimentalist point of view, another useful way to visualize the electric field is in terms of its angular frequency or in the spectral domain, where its spectral amplitude ($S(\omega) \propto |E(\omega)|^2$) can be directly measured using a spectrometer. A Fourier transform (FT) is a mathematical operation that enables the conversion of electric fields between time and frequency domains [7].

$$E(\omega) = \text{FT}(E(t)) = \frac{1}{\sqrt{2\pi}} \int_{-\infty}^{\infty} E(t) e^{i\omega t} dt \quad (2.7)$$

$$E(t) = \text{FT}^{-1}(E(\omega)) = \frac{1}{\sqrt{2\pi}} \int_{-\infty}^{\infty} E(\omega) e^{-i\omega t} d\omega \quad (2.8)$$

In the time domain, the pulse duration (or width) τ is defined as the full width at half maximum (FWHM) of the intensity $I(t)$ and similarly in the frequency domain, the spectral width (also known as the bandwidth) $\Delta\omega$ is defined as the FWHM of the spectral intensity $S(\omega)$. For a Gaussian pulse, the following relationship exists between bandwidth and pulse duration:

$$\Delta\omega = \frac{4 \ln(2)}{\tau} \quad (2.9)$$

If we write the bandwidth in terms of the photon energy, $\Delta E = \hbar\Delta\omega$, it results in *time-bandwidth product* (TBP).

$$\tau\Delta E = 4 \ln(2)\hbar \quad (2.10)$$

For transform-limited Gaussian pulses, a useful TBP formulation that converts between time and energy:

$$\tau[\text{as}] \cdot \Delta E[\text{eV}] = 1825 \quad (2.11)$$

This implies that the broader the supporting bandwidth, the shorter the pulse's possible duration. As an example, to achieve a 1-fs pulse duration, the spectral bandwidth should be larger than 1.8 eV. If we consider the entire visible light spectrum (400-800 nm), which has a 1.55 eV bandwidth, it cannot support sub-fs pulses on its own and

must be extended into a different spectral range. In this way, the TBP exemplifies the quantum mechanics uncertainty principle.

$$\Delta t \Delta E \geq \hbar/2 \quad (2.12)$$

Dispersion

The TBP describes the theoretically shortest pulse duration for a given bandwidth without taking into account the dispersion effect. However, dispersion cannot be avoided in reality, and the effect of dispersion must be considered in order to determine the effective pulse duration. In this case, Equation 2.9 changes to

$$\Delta\omega = \frac{4 \ln(2)}{\tau} \sqrt{1 + \left(\frac{a}{b}\right)^2} \quad (2.13)$$

where the pulse width parameter a is defined as

$$a = 2 \ln 2 \frac{1}{\tau^2} \quad (2.14)$$

and b is the chirp parameter [8].

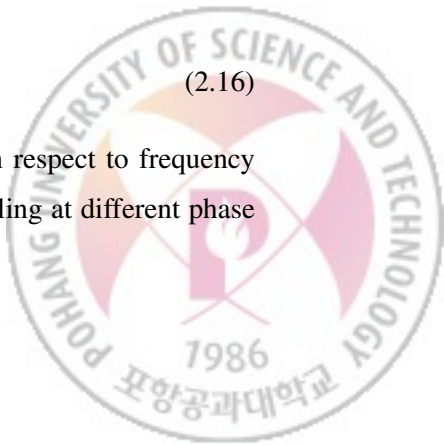
When light travels through a dispersive medium, a cumulative phase shift between the different frequencies occurs. The fact that the refractive index varies with the frequency of light and therefore each frequency travels at different phase velocities is known as dispersion. Then the phase velocity is defined as:

$$v_p(\omega) = \frac{c}{n(\omega)} \quad (2.15)$$

where v_p is the phase velocity of light, c is the speed of light in vacuum and $n(\omega)$ is the refractive index of light for a given frequency. The spectral phase of the electric field, $\phi(\omega)$, in the frequency domain is defined as [6]:

$$E(\omega) = \sqrt{S(\omega)} e^{-i\phi(\omega)} \quad (2.16)$$

The group velocity is the derivative of the spectral phase with respect to frequency and describes how the superposition of many frequencies traveling at different phase



velocities results in the speed at which the pulse envelope travels. The group velocity is thus defined as:

$$v_g(\omega) = \frac{c}{n(\omega) + \omega \frac{dn}{d\omega}} \quad (2.17)$$

The effect of the dispersion on a pulse can be understood by looking at the components of the Taylor expansion of the spectral phase (equation 2.16) about the central carrier frequency ω_0 :

$$\phi(\omega) = \phi_0 + \phi_1(\omega - \omega_0) + \frac{\phi_2}{2}(\omega - \omega_0)^2 + \frac{\phi_3}{6}(\omega - \omega_0)^3 + \dots \quad (2.18)$$

The first term ϕ_0 relates to the *carrier-envelope phase* (CEP). It is particularly relevant to few-cycle laser pulses, where the field envelope has a duration comparable to the optical period ($T = 2\pi/\omega_0$). It indicates the phase difference between the envelope's maximum and the carrier's maximum. CEP relevant issues in the experiment will be discussed in great detail in Chapter III. The second term (ϕ_1) in the Taylor expansion of the spectral phase is also referred to as *group delay* (GD). This term refers to the addition of a pure phase factor that is linear in frequency and corresponds to a pulse translation in time. This has no effect on the pulse duration, but it should be considered when there is a need for temporal overlap between two pulses, such as in pump-probe experiments. The third term (ϕ_2) relates to the *group delay dispersion* (GDD) and explains how the duration of the pulse changes due to the different frequencies being delayed relative to each other. A nonzero GDD results in a quadratic phase as a function of frequency; this is referred to as a linear chirp (i.e., linear change of the instantaneous frequency over the pulse duration in the time domain) and leads to a time-stretched pulse. In the visible and near-infrared wavelength ranges, most optical materials have a positive GDD [9], so the pulse accumulates more dispersion and becomes longer as it propagates through the medium. To achieve the shortest possible pulse, a negative GDD must be introduced to cancel out the positive GDD, resulting in a *fourier transform limited* (FTL) pulse. This can be accomplished through the use of chirped mirrors [10], which are dielectric multilayer mirrors specifically designed to slow down longer wavelengths more than shorter wavelengths by travelling a longer

optical path; this results in a negative GDD. All of the higher order terms in the Taylor expansion are crucial in the generation of ultrashort pulses and must be carefully optimized.



III. Few-cycle pulse generation

The main laser system is based on a commercial high energy, high repetition rate laser amplifier system (Femtopower HE/HR CEP, Femtolaser GmbH). The laser system is divided into two major components: a seed femtosecond laser oscillator and a multipass amplifier. The femtosecond oscillator serves as the primary workhorse in the field of experimental ultrafast physics and chemistry, as well as in a variety of other fields. In our laboratory, we use a femtosecond oscillator to deliver a sub-7 fs NIR pulse to the amplifier at a repetition rate of 75 MHz. Prior to seeding the multipass amplifier, the CEP of the oscillator output is stabilized via a feed-forward scheme (CEP4, Femtolaser GmbH) [11].

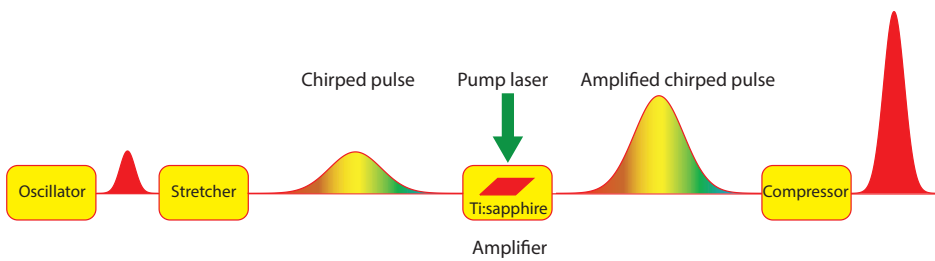


Figure 3.1: The chirped pulse amplification (CPA) method is illustrated schematically. The output of the ultrashort but low energy seed oscillator is time stretched and amplified with a multipass amplifier. The resulting high energy, relatively long pulse is recompressed using a grating compressor. It produces a high-energy, short pulse in the NIR spectral domain.

For safe amplification, the CEP stabilized seed pulse is stretched in time via bulk

glass material in the amplifier section. The beam is then injected into the laser cavity of a multi-pass amplifier. For amplification, a Ti:sapphire crystal is situated in a small vacuum chamber that is cryogenically cooled (down to 90 K) and pumped by a high-energy 532 nm green laser (DM50, Photonics industries). Finally, following the grating compressor, a multi-pass amplifier (10-passes) delivers 3 mJ (3 kHz, 25 fs) pulse energy in the output. Fig 3.1 illustrates a simplified schematic diagram of the laser system. The following sections will go over each component in detail.

3.1 Femtosecond oscillator

The femtosecond oscillator is the starting point for all experiments in a laser laboratory. Using the well-known *Kerr-lens mode-locking* (KLM) mechanism [12, 13], the femtosecond oscillator generates pulse trains with equal spacing. To generate femtosecond pulse trains using the KLM mechanism, a 3.1 W diode-pumped solid-state (DPSS) laser (Lighthouse photonics, 532 nm Sprout-D 5W NET [14]) is focused through a lens into a thin highly doped Ti:sapphire gain medium cut at the Brewster's angle to avoid reflection losses. The GDD of the laser pulses is controlled by a set of chirped mirrors and wedged fused silica plates inside the oscillator cavity. Possible back reflections from the outside of the oscillator are prevented by the wedge shaped output coupler, which transmits 15% of the intracavity energy. The laser pulses are compressed after transmission through the output coupler by two reflections on each of two chirped mirrors. Following that, the oscillator output is sent to the CEP4 module and focused into a periodically poled lithium niobate (PPLN) crystal as part of the fast loop of the CEP stabilization described in greater detail in Section 3.3.1. Another set of chirped mirrors compensates for the chirp introduced by the transmission through the PPLN crystal, and the subsequent amplifier system is seeded with CEP stabilized laser pulses with a sub-7 fs pulse duration (FWHM), a repetition rate of 75 MHz, and an average output power of 250 mW. The resulting oscillator output spectrum is depicted in Fig 3.3.

3.2 Multi-pass amplifier

Donna Strickland and Gérard Mourou [15] invented the *chirped pulse amplification* (CPA) method, which is now widely used in high energy laser systems. A CPA system begins by stretching the output pulses of an oscillator in time via some material dispersion. By doing so, the lengthened pulses can be safely amplified before being recompressed. Following that, a cryogenically cooled Ti:sapphire crystal is used as a gain medium, where the stretched femtosecond laser pulses from the oscillator and a frequency-doubled Q-switched Nd:YAG (55 W) pump laser are focused and spatially and temporally overlapped as shown in Fig 3.2. The stretched pulse is amplified by passing 10-times through the Ti:sapphire crystal. After the fourth pass, a Pockels cell unit reduces the repetition rate from 75 MHz to 3 kHz. The pulse is then shaped with a Dazzler unit (Dazzler, Fastlite) to compensate for dispersion and gain narrowing during amplification. A telescope recollimates the beam after the eighth pass to reduce the intensity at the crystal. After the tenth pass, the beam is compressed with a transmission type grating, which produces a 3 mJ, 28 fs output pulse at a repetition rate of 3 kHz. To achieve sub-5 fs pulse duration, the output spectrum of the amplifier is further broadened and the details will be discussed in Section 3.4.



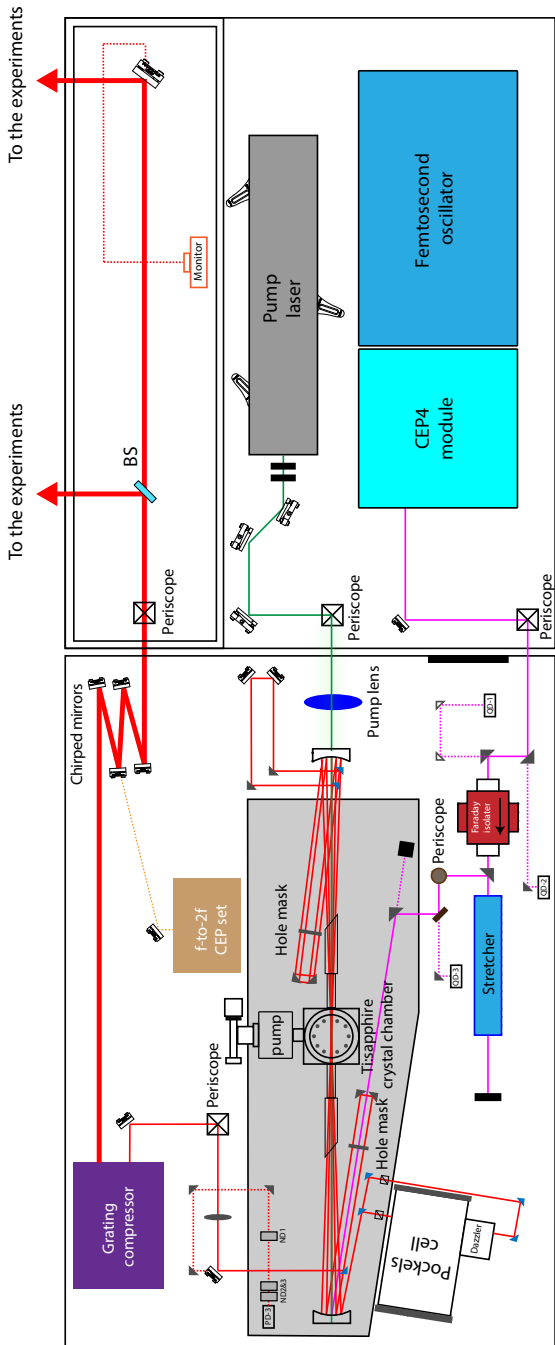


Figure 3.2: The 3 mJ, 3 kHz multipass laser amplifier system.

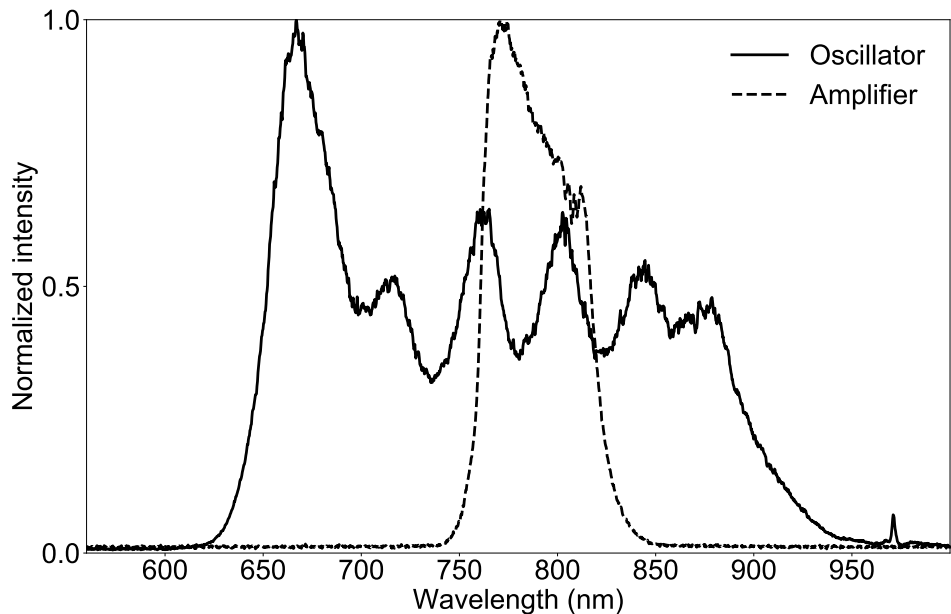


Figure 3.3: The output spectrum of the femtosecond oscillator is shown alongside the output spectrum of the amplifier with the central wavelength of 790 nm. The oscillator spectrum's bandwidth supports pulses with a duration of less than 7 fs, whereas the amplified output spectrum supports only pulses with a duration of 28 fs.

3.3 Carrier-envelope-phase stabilization

The underlying physical process for the generation of attosecond light pulses is *high-order harmonic generation* (HHG). According to a semiclassical model, in order to generate an attosecond pulse through HHG, the driving laser intensity should be on the order of $\sim 10^{13}\text{-}10^{14}$ W/cm², and with this sufficient field strength one of the valence electrons will tunnel ionize and then be driven back to the parent ion, resulting in a burst of attosecond XUV light. To optimize this HHG process, the interaction between the atom and the few-cycle laser must be limited to the driving laser's cycle

duration. When the pulse duration is reduced to a value comparable to 2-3 optical cycles, change in the peak electric field due to the CEP becomes significant. As a result, the CEP of the driving laser pulse becomes critical for generating isolated attosecond light pulses, and it is necessary to ensure the pulse's CEP is stable. In this section, we will discuss about the CEP measurement and stabilization methods for the oscillator and amplifier.

3.3.1 Oscillator CEP

The CEP of the oscillator pulses varies from pulse to pulse due to the difference between the group and phase velocity in the cavity, which results in a CEP slip on each cavity round-trip as shown in Fig. 3.4. Additionally, pulse energy instabilities, which result in nonlinear refractive index fluctuations, as well as center frequency instabilities, result in CEP fluctuations.

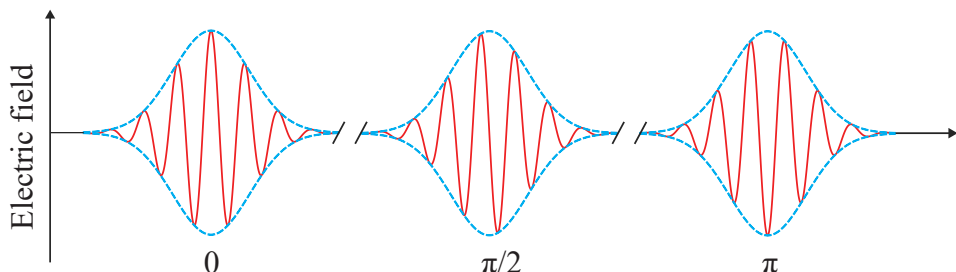


Figure 3.4: Pulse trains emerging from the femtosecond oscillator with different CEP. Left to right; $0, \pi/2, \pi, 3\pi/2$ respectively. The FWHM of each pulse is 4 fs.

In addition, numerous sources of noise and vibration are likely to exist in a typical laser laboratory, such as running air conditioners, vacuum pumps, and chillers. Some of the common noise sources in the laboratory are mechanical vibrations, air pressure change, and temperature drift. Active stabilization of the CEP is divided into two parts: First, the fast loop stabilizes the CEP of the oscillator output pulses, which

is typically generated by the oscillator itself. As the name implies, this stabilization is fast and runs at MHz frequencies because it has to compensate for the fast changes in the CEP caused by pump laser intensity fluctuations and acoustic noise in the laboratory etc. as opposed to the slow loop which is usually caused by mechanical and temperature drift. First, the oscillator output is sent to the CEP4 unit, which detects and stabilizes CEP fluctuations. In the CEP4 unit, the oscillator output pulses are focused on a PPLN crystal, which is tuned to frequency-shift the short-wavelength part of the oscillator spectrum to match the low-wavelength part via difference-frequency generation (DFG). Afterwards, CEP jitter is measured with a photodiode by detecting the beating signal between the long-wavelength part of the fundamental spectrum and the SFG (Fig 3.5) spectrum from the PPLN crystal (f-to-2f interferometer) [16].

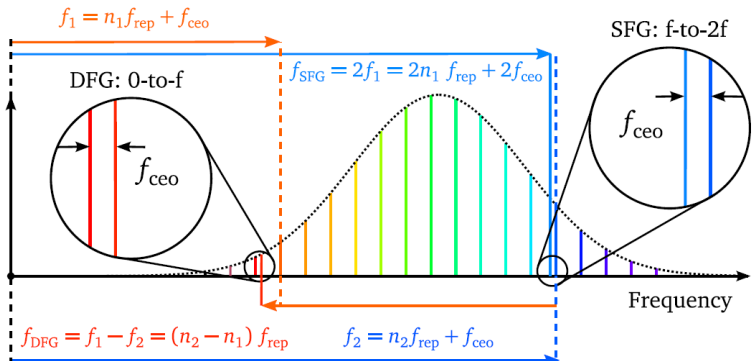


Figure 3.5: The self-referencing technique is depicted schematically. Adapted from Ref. [16]

Meanwhile the main oscillator beam is routed through an acousto-optic frequency shifter (AOFS), which is part of the CEP stabilization's fast loop. The CEP beating signal from the photodiode is amplified and applied to the AOFS, thereby removing the carrier-envelope offset frequency from the beam which is diffracted from the AOFS in the first order, thus locking the CEP of the output beam to zero. Slow CEP drift is stabilized by adjusting the temperature of the Ti:sapphire crystal and the dispersion

compensation wedge inside the oscillator cavity. To control the temperature of the Ti:sapphire crystal, a transistor is attached to the crystal mount, and one of the fused silica glass wedges is mounted on a motorized stage, both of which are controlled by an external PID controller unit that is a part of the CEP4 unit. Consequently, the multipass amplifier is seeded with the CEP stabilized laser pulses, which have a 6 fs pulse duration (FWHM) and 130 mW average output power.

3.3.2 Amplifier CEP

The CEP stabilized laser pulses accumulate a significant amount of CEP jitter as they pass through the multipass amplifier, which varies on a Hz scale and is primarily caused by thermal instabilities during amplification. This slow CEP drift can be compensated for by a second CEP stabilization loop operating at 100 Hz. The oscillator fast loop and the amplifier slow loop are completely decoupled because the oscillator fast loop stabilizes CEP changes via the AOFS in the CEP4 unit, whereas the amplifier slow loop controls tiny changes in the CPA amplifier's prism stretcher. To name a few CEP-noise sources in the amplifier;

- Pumps laser intensity noise
- Pump laser timing jitter
- Thermal load on the amplifier crystal, and cryogenic cooling
- Repetition rate change

Unlike the oscillator CEP detection and correction, the amplifier section was designed to address two major shortcomings of the previous implementations: The laser amplifier's relatively narrow output spectrum precludes direct f-to-2f measurement and necessitates spectrum broadening in a filament via white light generation. This filament is typically realized in a sapphire plate and is extremely sensitive to intensity fluctuations; this dependency translates intensity fluctuations into artificial phase noise

in the detection. For this purpose, a small portion of the amplifier output beam is sent into a custom f-to-2f interferometer (Fig. 3.6), which generates spectral interference fringes.

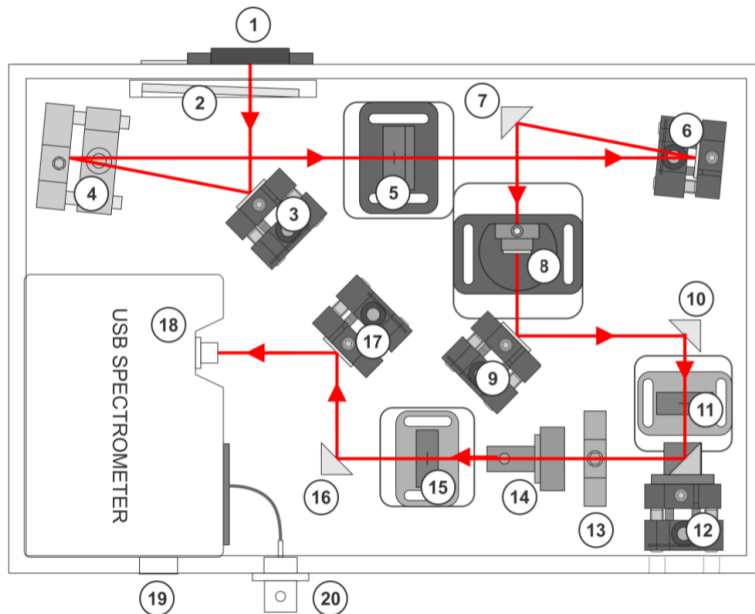
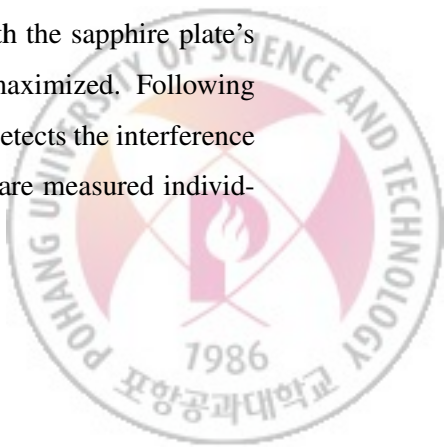


Figure 3.6: The schematic setup of the f-to-2f interferometer. Adapted from Femtoworld HE/HR laser user manual (Femtolasers GmbH).

In short, the incoming beam is focused onto a sapphire plate (5) by a mirror (4) after passing through an aperture (1) and a variable ND filter (2). Following the sapphire plate, a mirror (6) focuses the beam onto a beta barium borate (BBO) crystal (8), which frequency-doubles wavelength components around 1064 nm, resulting in spectral interference fringes around 532 nm. The polarizing beam splitter (14) is used to match the intensities of the frequency-doubled spectrum with the sapphire plate's octave spanning spectrum, allowing the fringe contrast to be maximized. Following that, a lens (15) focuses the beam into the spectrometer, which detects the interference fringes for individual laser pulses. To ensure that laser pulses are measured individ-



ually, the USB spectrometer must be triggered by a TTL signal clocked by repetition rate of femtosecond oscillator. For the coupling to the spectrometer, a steering Mirror (12) is employed. The resulting fringes are then measured using a USB spectrometer (Flame-T, Ocean optics) located inside the interferometer housing and a software is used to calculate the CEP of the laser pulses.

The CEP is measured for each laser pulse, and the control loop can generate feedback for each measured laser pulse. This is accomplished by adjusting the dispersion within the amplifier system. It should be noted that the number of measured laser pulses is limited by the speed of the USB spectrometer (~ 0.3 ms) and varies depending on the laser repetition rate. The overall speed of the control loop is thus determined by the spectrometer speed, as well as the actuator that compensates for the CEP.

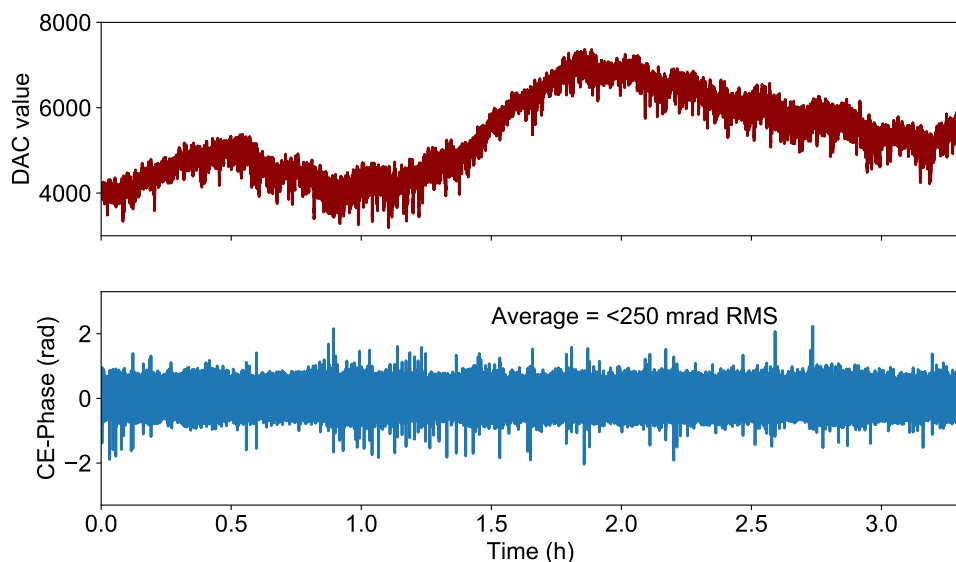


Figure 3.7: Amplifier CEP measurement and stabilization. The average amplifier CEP drift is less than 250 mrad RMS over 3 hours of measurement.



3.4 Supercontinuum generation

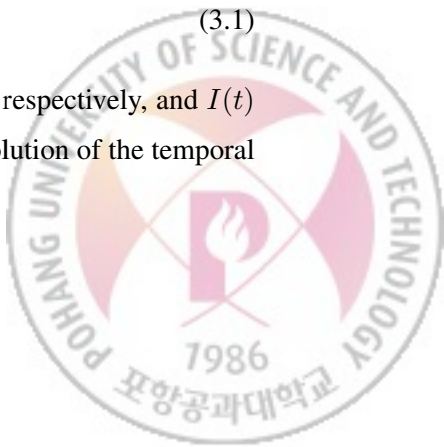
To achieve an even shorter pulse duration, *a hollow-core fiber* (HCF) setup with a *chirped mirror* (CM) compressor was implemented after the multi-pass amplifier system [17]. The HCF compression method was chosen due to its high amount of spectral broadening and compatibility with high energy input pulses (up to few millijoules). Due to these advantages, HCF compression has become a popular method for generating few-cycle pulses for attoscience. The amplified infrared pulses from the amplifier output are focused into a noble gas-filled (typically neon) HCF of about 100 cm length, where the high peak intensities induce a variety of nonlinear processes in the gaseous medium. As the pulse propagates through the fiber, the nonlinear response of the atomic gas to the intense laser pulse results in spectral broadening, a phenomenon referred to as *self-phase modulation* (SPM) and *self-steepening* (SS). However, due to the chamber's input and output windows, as well as the effect of self-phase modulation of the pulse as it propagates through the medium, the pulse can gain a significant amount of positive dispersion. This additional dispersion must be compensated in the pulse compression stage following spectral broadening, which can be accomplished with multilayer chirped mirrors. In this manner, the 28 fs pulses from the amplifier output can be compressed down to sub-5 fs, which is a sufficiently short pulse duration for the generation of few-cycle deep UV and attosecond XUV pulses.

Self-phase modulation

The primary effect that results in spectral broadening is SPM. The temporal variation in laser intensity results in a temporal variation in the refractive index:

$$n = n_0 + n_2 I(r, t) \quad (3.1)$$

where n_0 and n_2 are the linear and nonlinear refractive indices respectively, and $I(t)$ is the laser intensity. The simplest model accounting for the evolution of the temporal



phase links the instantaneous frequencies to the pulse intensity as [18]:

$$\omega(t) = -\frac{\partial \phi}{\partial t} \approx \omega_0 \left(1 - \frac{n_2}{c} z \frac{\partial I(r, t)}{\partial t} \right) \quad (3.2)$$

As a result of this temporal change in refractive index, new frequencies appear in the laser spectrum depending on the slope of the pulse $\partial I / \partial t$, the propagation distance z in the Kerr medium and its nonlinear index coefficient n_2 . In a purely Kerr medium, the front part of the pulse generates redder frequencies, the back part bluer frequencies.

Self-steepening

SS of laser pulses occurs when the velocity of the pulse's peak intensity is less than the velocity of the pulse's trailing edge, due to the intensity-dependent change in refractive index $\Delta n = n_2 I(r, t)$. From the refractive index Δn , it is apparent that the pulse group velocity decreases with increasing laser intensity. Considering a Gaussian pulse, the peak is slowed in relation to the pulse group velocity, while the trailing part catches up with the peak, resulting in the formation of a steep edge in the trailing part of the pulse. This effect results in a faster self-focusing of the pulse's trailing portion (in comparison to the leading portion) and an increase in the bluer frequency generated by the steep trailing portion. Combining SPM and SS in a broader context explains why frequency generation is shifted toward higher frequencies, or in other words, why the central wavelength is shifted toward the blue range of the spectrum. This can be understood by considering the SPM's influence on the two subpulses. The SPM generates red and blue frequency components on either side of the main pulse. As a result, the front and back sub-pulses only have red or blue frequencies. The back pulse propagates into the central part due to the self-steepening effect, increasing its intensity. Consequently, the complete pulse consists of a high-intensity portion dominated by blue frequencies and a low-intensity portion dominated by red frequency. Naturally, the SPM is more efficient for the extremely intense part, and therefore, blue frequency generation predominates. In between SPM and SS, SPM is more favorable for pulse compression [19].

In Fig. 3.8, a pulse propagation simulation is shown for different propagation distances. The simulation parameters were chosen to match the experiment.



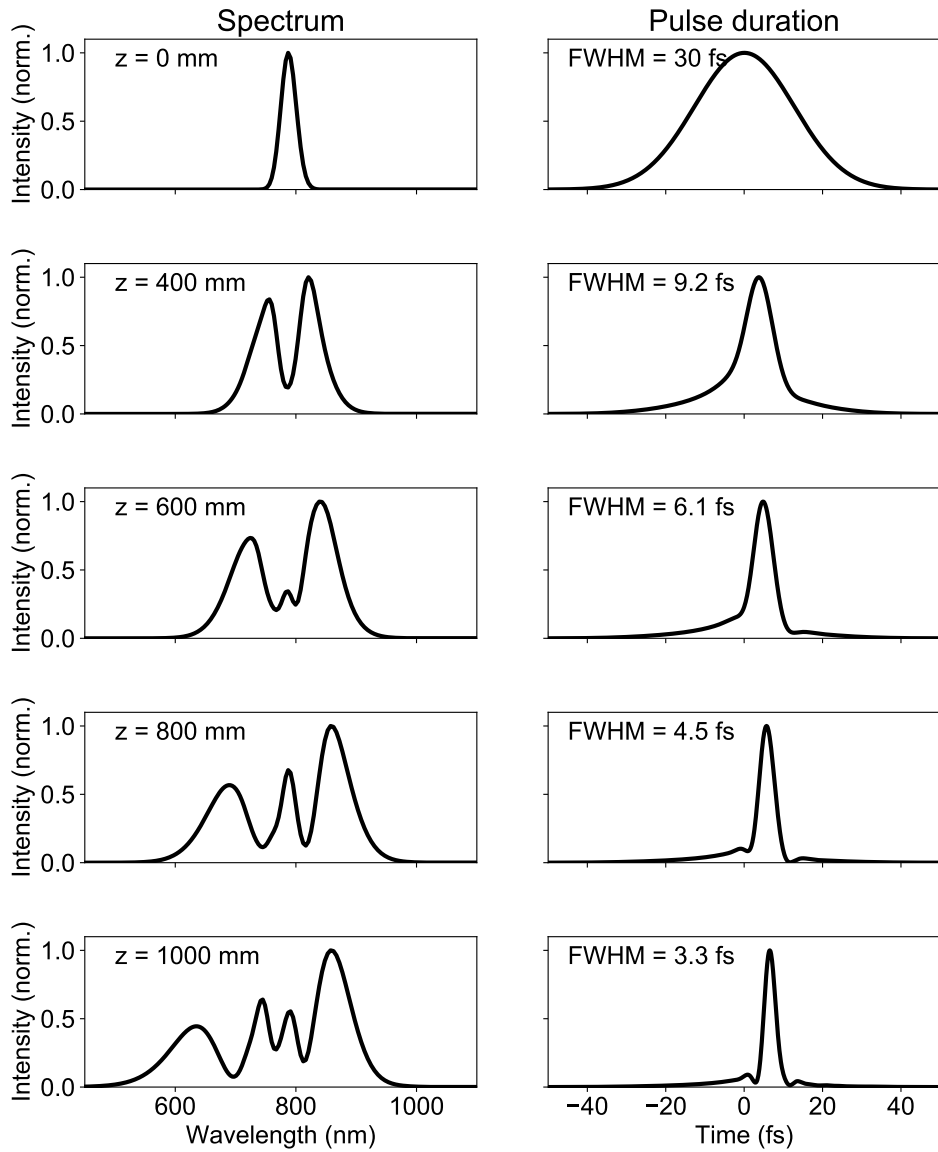


Figure 3.8: Pulse propagation simulations at various propagation distances. The left panel, shows the spectra, while the right panel depicts FTL pulses generated by the spectra. SPM and SS were both taken into account in the simulation.

3.4.1 Experimental setup

The experimental realization of the nonlinear phenomena discussed previously is accomplished using the experimental setup depicted in Fig. 3.9. The output of the CPA laser is split 50:50 and the beam is directed to the supercontinuum chamber via low GDD dielectric mirrors (20B20UF.25, Newport) and focused using a combination of two lenses with an effective focal length of about 1.5 m. In the supercontinuum chamber, a 100 cm long, 400 μm inner diameter HCF was mounted on a custom-made V-groove mount and filled with Ne gas at a pressure of 3 bar to produce a nonlinear SPM effect. A beam position locking system (TM Messtechnik) was implemented to ensure stable pointing at the hollow core fiber's entrance. A weak leakage (dashed lines in Fig 3.9) from the closest dielectric mirror in the supercontinuum chamber was picked up and sent to the position sensitive detectors (PSD-A and PSD-B). Detectors A and B continuously measure the laser position and angle deviations from a reference focus position and feedback with the measured error signal to the PID control unit of the stabilization system. An active feedback loop then controls the motorized piezo actuators (MoPiA) to compensate for the error and thus lock the beam position on the target location within 5 μm accuracy. At the focal point, the measured beam diameter ($1/e^2$) was approximately 240 μm , or approximately 60% of the fiber inner diameter, ensuring optimum coupling to get the highest throughput.



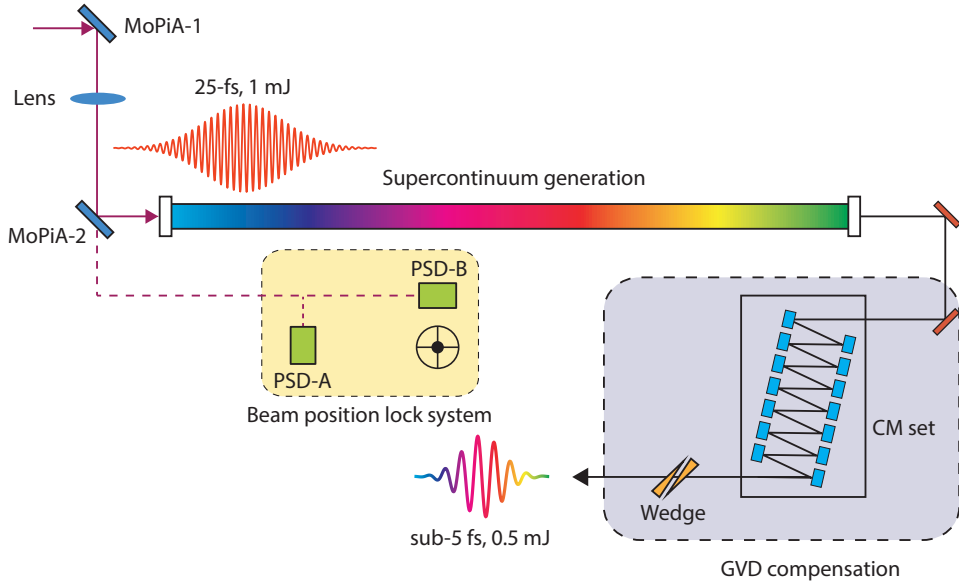


Figure 3.9: Supercontinuum generation setup. Inside the chamber, a 100 cm long, 400 μm inner diameter HCF is installed and filled with 3 bar neon gas. Before the entrance, a beam position locking system is implemented, and after the HCF setup, a pulse compression setup is shown.

To obtain sufficient spectral broadening, the appropriate gas pressure must be obtained. In this regard, we should adjust the gas pressure to maintain a spectrum with a sub-5 fs Fourier transform limit (FTL) at the output of the fiber, i.e., a constant broadening factor

$$F = \frac{\Delta\omega}{\Delta\omega_0} \quad (3.3)$$

where $\Delta\omega_0$ and $\Delta\omega$ are the initial and final pulse bandwidths, respectively. Numerous undesirable processes such as plasma formation, dispersion, and beam fluctuations can occur at a certain pressure level. In our case, we found that filling with 3 bar of neon gas was optimal for obtaining the desired spectral broadening following HCF setup. Due to the relatively high ionization potentials of noble gases, particularly neon and

argon, hollow-core fiber setups are typically operated with them. Nonetheless, plasma formation due to multiphoton ionization is possible in these gases and must be avoided, as it results in the destruction of the fiber material, particularly at the fiber's entrance. To avoid such occurrences, a glass tube (Fig 3.10) has been installed around the laser focus to monitor the laser-fiber coupling. Additionally, such plasma formation has the potential to distort the laser mode, reducing the output power and deteriorating the quality of the CEP stabilization. Section 3.3 discussed the technique for measuring and stabilizing CEP jitter in detail.

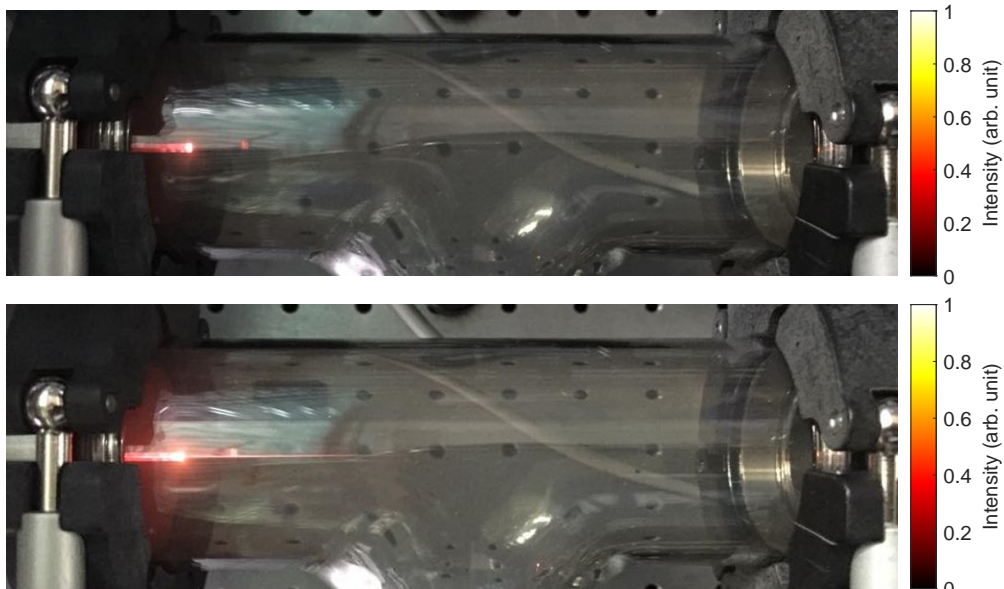


Figure 3.10: A glass tube was installed near the laser-fiber coupling. By looking through the glass tube, the laser can be safely coupled to the fiber. Plasma formation in front of the fiber tip is also shown, which must be avoided at all times.

After proper spectral broadening in the HCF setup, the inherent nonlinear phase accumulation induced by the SPM, other dispersive elements such as the supercontinuum generation chamber input and output windows (each for 1 mm thick fused silica

(FS)) and the HHG chamber entrance window (1 mm FS) can introduce additional dispersion and must be compensated for in advance. Considering all of this, output pulse after supercontinuum generation is compressed using 14 reflections on double-angled chirped mirrors (PC1332, UltraFast Innovations GmbH), which provide -40 fs^2 dispersion per bounce in the 450-1000 nm spectral range. Additionally, a pair of wedged glasses (50 mm long, with the apex angle of 4° , FS) is used for fine adjustment of GDD. Figure 3.11 show a typical spectrum after the supercontinuum generation setup, which supports sub-5 fs pulse duration.

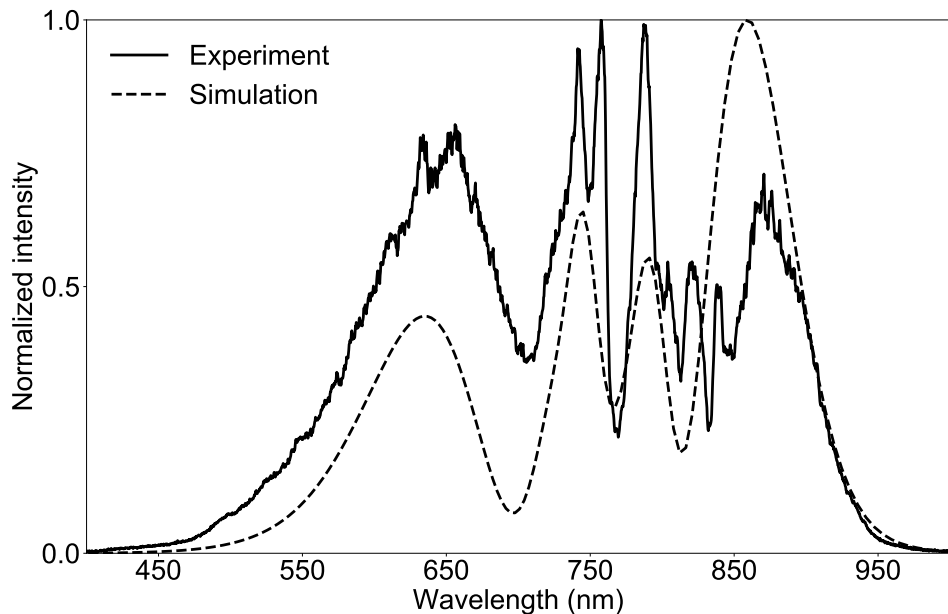


Figure 3.11: Experimental and simulated supercontinuum generation output spectra. The spectrum supports sub-4 fs pulse duration.



Third-order dispersion compensation

Propagation through a nonlinear medium introduces a positive dispersion on the output pulse, which is successfully compensated using chirped mirrors, as previously stated. These chirped mirrors, however, are intended to compensate for GDD but not for higher order terms. When aiming for pulse compression to the few-cycle range, higher order terms, specifically third-order dispersion (TOD), play a critical role in obtaining high-contrast few-cycle laser pulses. As a result, TOD compensation is also required. We used 2 mm of ammonium dihydrogen phosphate (ADP) as a material to compensate for residual TOD in our experiment. The experimental layout is shown below.

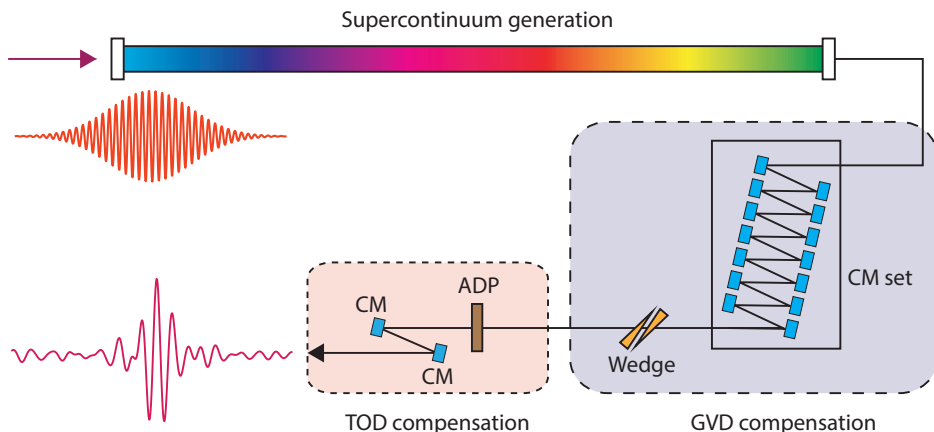


Figure 3.12: Few-cycle pulse compression scheme.

Following GDD compensation, a compressed sub-5 fs pulse is sent through a 2 mm thick ADP crystal, compensating for the residual TOD. The extra GDD introduced by the ADP material is compressed once more with another set of chirper mirrors, yielding a 3.4 fs pulse which corresponds to 1.2 optical cycles at 800 nm (see Section 3.4.3).

3.4.2 CEP after pulse compression

As previously stated, we must maintain an acceptable level of CEP stability throughout the experiment. While we stabilize the CEP in the amplifier section, the quality of the CEP lock can degrade following the supercontinuum generation due to plasma formation in front of the fiber tip (see Fig. 3.10). To ensure CEP stability following the HCF setup, we constructed our own CEP detection setup using an f-to-2f interferometer which is simpler than the amplifier CEP detection due to the broad bandwidth of the pulses at this stage. This CEP detection setup was implemented after the supercontinuum generation chamber since the output spectrum of the HCF is octave spanning, and no additional spectral broadening is required. A schematic drawing of the setup is shown in Figure 3.13. In summary, the spectrally broadened HCF output is directed to the setup and focused on a thin BBO crystal via an off-axis parabolic mirror. Following the *second harmonic generation* (SHG) with the BBO, the residual fundamental NIR laser is blocked with a bandpass filter and the generated SHG polarization is rotated with a half-wave plate to have the same polarization as the fundamental NIR. A Glan-Thompson polarizer is used after the filter to control the polarization. Since SHG signal has a partial spectral overlap with the fundamental NIR, the fringe pattern can be measured with a high-resolution spectrometer. Experimentally, f_{offset} is observed as a spectral interference pattern where the fundamental and frequency-doubled light overlap. The period and phase of this interference pattern can be analyzed using a simple Fourier transform of this part of the spectrum and by monitoring its evolution, a feedback signal is generated using a custom made control software.



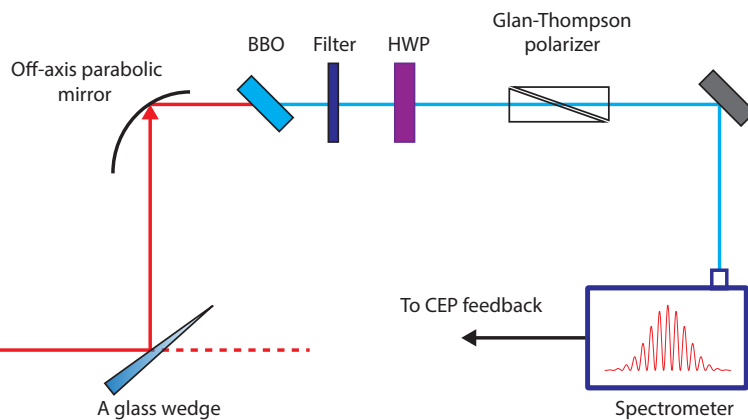


Figure 3.13: F-to-2f interferometer configuration. The wedge's reflection is picked up and routed into the setup for measuring CEP jitter. HWP: half-wave plate

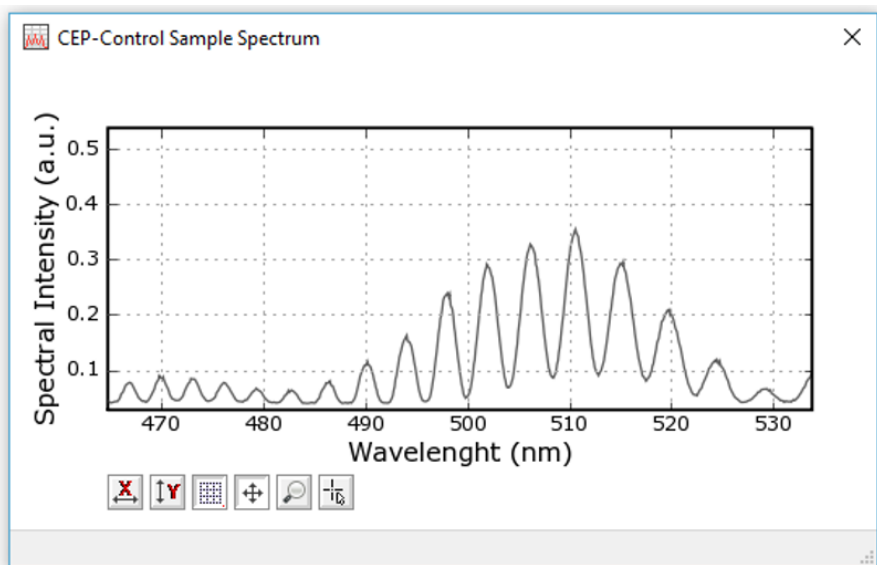


Figure 3.14: Spectral interference fringes are used to extract CEP information.

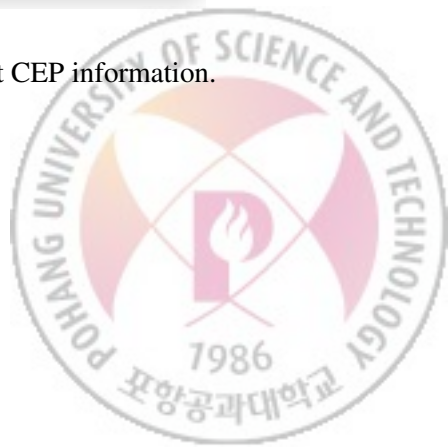


Fig. 3.14 illustrates the observed fringe pattern. Within the laser amplifier, the feedback signal is converted to a displacement of one of the stretcher prisms. By displacing the prism perpendicular to the beam with a piezo translation stage, the beam direction is maintained almost unchanged, but the amount of material dispersion accumulated by the pulses is adjusted. A proportional–integral–derivative (PID) controller algorithm compensates for CEP changes by adjusting the prism position. The phase stability achieved was less than 250 mrad, which can be attributed primarily to the avoidance of plasma formation in front of the hollow core fiber entrance. Two examples of fiber entrances with varying input pulse energies are shown in Fig. 3.10.

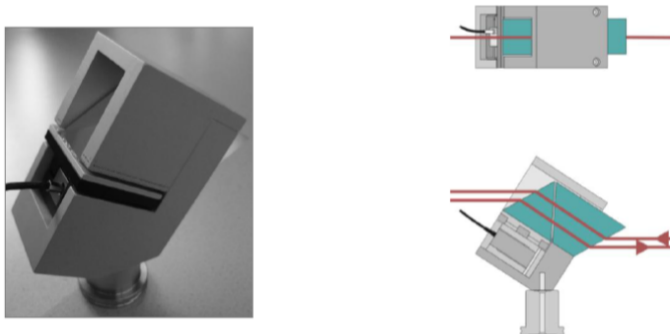


Figure 3.15: The piezo stretcher actuator is used to compensate for the amplifier system's CEP drift. It is made up of two glass prisms, one of which is fixed and the other of which is attached to a piezo actuator and can be moved relative to the other prism. This enables changing the amount of glass material (dispersion) without changing the laser beam's pointing or beam parameters.

If the phase noise emerging in the HFC and detected with the f-to-2f technique is uncorrelated with the phase noise of the input pulses, the standard deviations of the two noise contributions add geometrically:

$$\sigma_{\text{tot}} = \sqrt{\sigma_{\text{amp}}^2 + \sigma_{\text{HCF}}^2} \quad (3.4)$$

3.4.3 Pulse characterization

It is just as important to measure the pulse duration as it is to generate the pulse. As short-pulse generation technology improves, so do measurement techniques. Just a few examples include *frequency-resolved optical gating* (FROG) [20], *spectral phase interferometry for direct electric-field reconstruction* (SPIDER) [21], *dispersion scan* (d-scan) [22], and others. Here, we used the d-scan method, since it is simple to implement and well-suited for our ultrabroadband few-cycle pulses. The layout of the d-scan setup is depicted in Fig. 3.16.

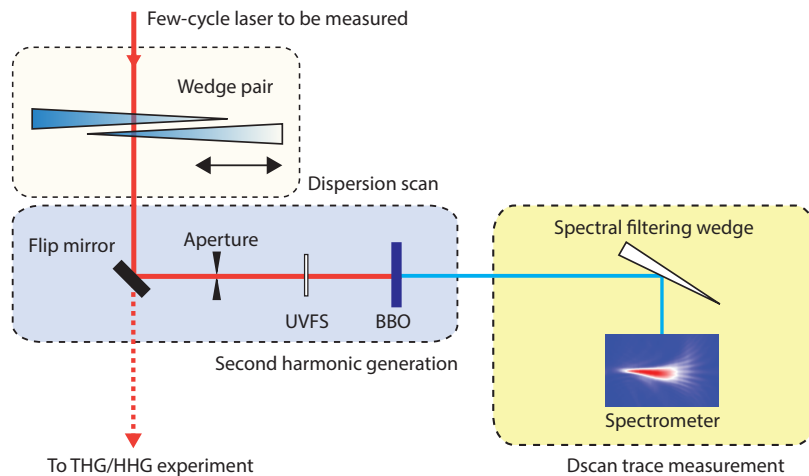


Figure 3.16: Dispersion scan setup. Ultrashort pulses are sent to an ultrathin ($5 \mu\text{m}$) BBO crystal and the generated SHG signal is measured with a spectrometer while the dispersion is scanned. The dispersion scan was performed using a glass wedge in the beam path.

The method of dispersion scanning is based on SHG. This method determines the dispersion by measuring the two-dimensional trace of the second harmonic as a function of wedge insertion. One can extract the spectral phase information of the input pulse from the measured 2D trace using an algorithm (e.g., differential evolution) [23],

whereas the pulse spectrum is easily measurable using a spectrometer. One can easily obtain the pulse duration information from the spectral intensity and spectral phase. To measure the dispersion dependent SHG trace, after the supercontinuum generation and compression, the beam was sent to the d-scan setup. After the pick-up mirror, an aperture and variable neutral-density (VND) filter are used to reduce the power down to 10 mW and subsequently the beam is focused by a 50 cm focal length spherical mirror onto the BBO. In order to simulate the vacuum chamber's input windows and an inherent TOD in the supercontinuum, UV-grade fused silica plate or an ADP crystal was placed before the BBO.



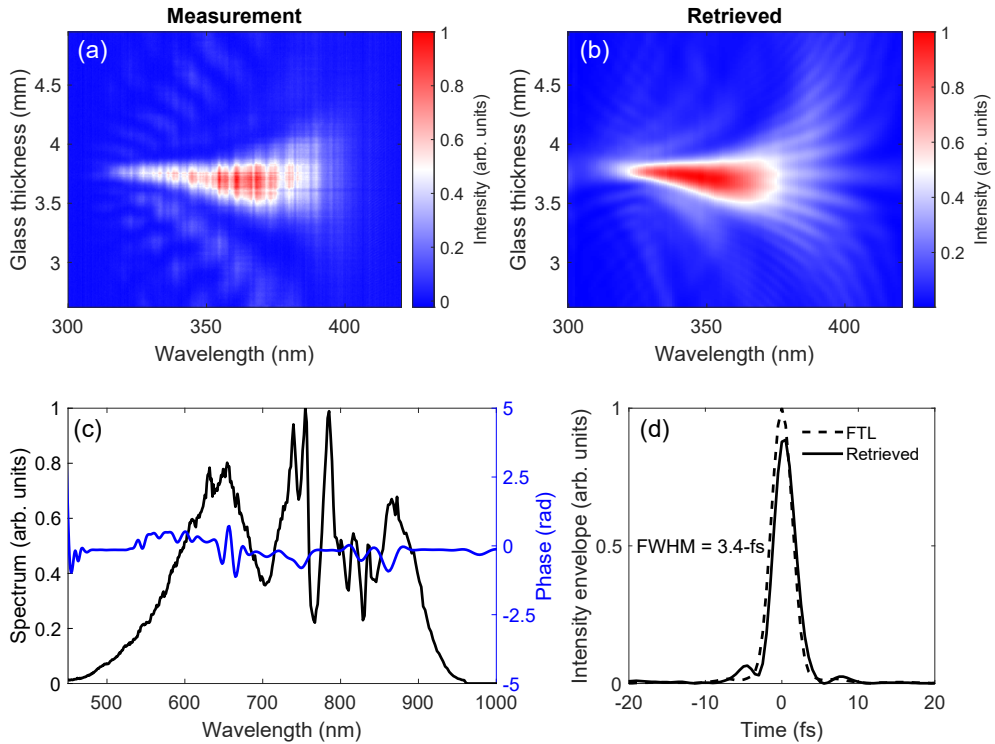


Figure 3.17: D-scan measurement of a few-cycle waveform generated by a hollow-core fiber statically filled with Ne at 3.0 bar. (a) Measured trace (b) Retrieved trace. (c) Corresponding spectrum (black) and the reconstructed spectral phase (blue). The spectrum spans from 450 to 950 nm and supports a Fourier transform-limited pulse duration of 3.3 fs. (d) Reconstructed intensity envelope (solid curve) exhibiting a pulse duration of 3.4 fs. The reconstructed envelope is nearly identical to the Fourier transform-limited envelope (dashed curve).



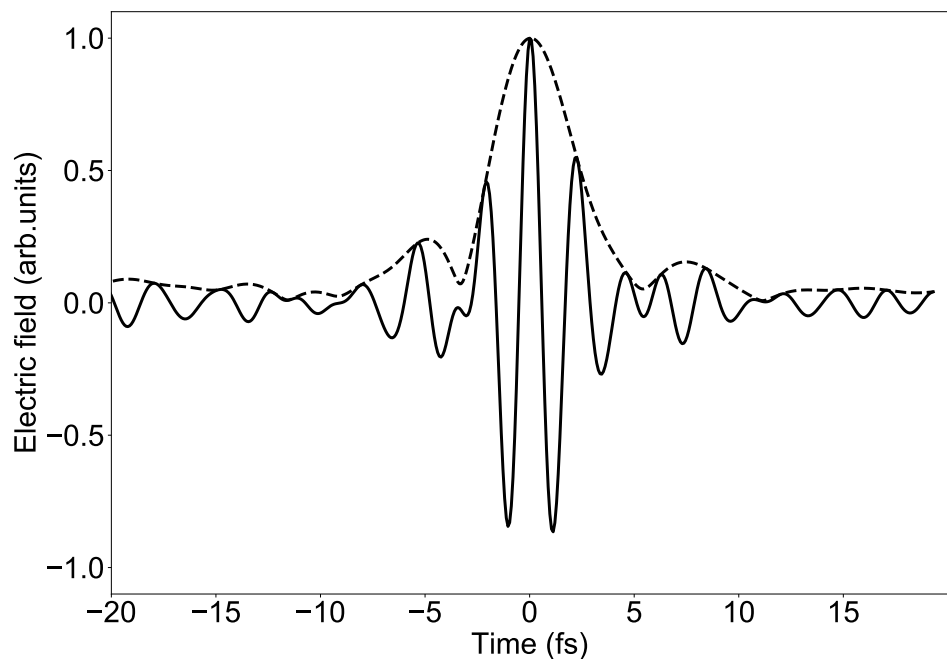


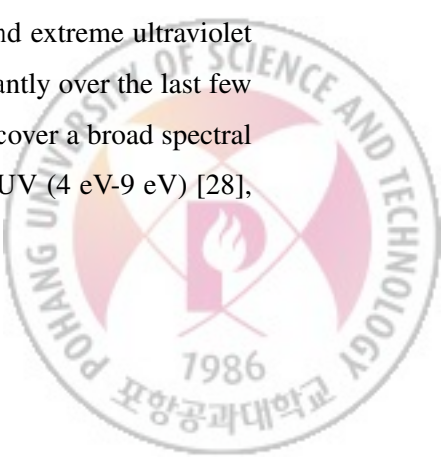
Figure 3.18: Reconstructed electric field of a few-cycle waveform (solid curve) with a period of only 3.4 fs (\sim 1.2 optical cycles) and its field envelope (dashed curve).



IV. Development of an ultrashort DUV/XUV beamline

4.1 Motivation

The control of material processes at the level of electron motion in real time has become one of the significant challenges in fundamental science [24]. The triggering and complete measurement of the valence orbitals of neutral electronic systems, the most relevant chemical function has hitherto remained inaccessible. For the control of chemical dynamics in a new paradigm, therefore, we need to understand the dynamics beyond the Born Oppenheimer approximation where the electronic states are not stationary and influential. We need to explore how nonstationary electronic states are coupled to nuclear motion and subsequently understand how the manipulation of the electronic motion can be used to trigger a selective motion of the nuclei thereby implementing a chemical reaction pathway. Ultrafast charge migration and conical intersection dynamics are a few examples among many chemical dynamics [25]. Ultrafast migration of a charge driven by electron correlation is manifested when ultrashort ultraviolet (UV) laser pulses create electronic wave packets, triggering pure electron dynamics in an ionized system. Most of the past efforts have been focused on the control of nuclear dynamics [26]. Even though electronic coherence and its coupling to nuclear degrees of freedom may profoundly affect the outcome of these processes, electron dynamics has received less attention. Proper investigation of electron dynamics in materials demands ultrafast sources in the visible, UV, and extreme ultraviolet (XUV) spectral region. Laser technology has advanced significantly over the last few decades, and now multiples of table-top ultrashort sources that cover a broad spectral range including: visible (1.5 eV-4 eV) [27], deep and vacuum-UV (4 eV-9 eV) [28],



extreme-UV (10 eV-100 eV) [29] and the X-ray region (100 eV-1000 eV) [30, 31] are available in the laboratories. To conduct dynamical studies of atomic and molecular systems, the well-known pump-probe technique is used, in which pump pulses perturb the system via ionization or excitation, while time-delayed probe pulses record the system's changes. This way, one can observe the system's dynamical evolution on their natural time scale. Attosecond XUV pulses are combined with NIR laser pulses in this example. However, when using NIR laser pulses, attosecond pulses in the XUV regime preclude the study of neutral species due to their excitation of core-level electrons and multiphoton photon process in the probe step. For this purpose, a few-cycle deep-UV (DUV) and XUV beamline has been constructed for studying ultrafast electron dynamics in molecules.

4.2 Design of the beamline

Attosecond chemical physics (ACP) beamline consist of three chambers: source, delay and target or interaction chamber, respectively, and schematically represented in Fig. 4.1. The beamline is driven by CEP-stabilized sub-4 fs visible/NIR pulses (see Fig 3.17) with 0.25 mJ energy at 3 kHz repetition rate and the details of ultrashort pulse generation method are discussed extensively in Chapter III. Few-cycle driving visible/NIR laser pulses were focused into a quasistatic gas cell supplied with noble gases using an $f = 500$ mm focal length spherical mirror, which was located in the source chamber (Fig. 4.1, first yellow panel). To control the gas pressure build-up during the *third-order harmonic generation* (THG) and *high-order harmonic generation* (HHG), a dual-chamber design was implemented and two introversive conical-shaped conduction barriers (or gas barriers) were installed in the inner chamber (see Fig. 4.2). With this design, we minimized the gas flow to other chambers and maintained a residual gas pressure well below 10^{-5} mbar during the experiment, which was necessarily needed to operate the microchannel plate (MCP) in the target chamber even when the THG was operating at a high gas pressure (up to 2 bar). The source chamber con-

ceptual design is shown in Fig. 4.2. An inner small vacuum chamber is backed up by a 1200 liter/min scroll pump (ISP1000E, Anest Iwata), which was directly nested inside the main vacuum chamber. Any residual gas pressure build-up in the main source chamber was pumped by 500 liter/min turbo-molecular pump (TMP) which works as a differential pump with the help of additional gas flow conduction barriers.

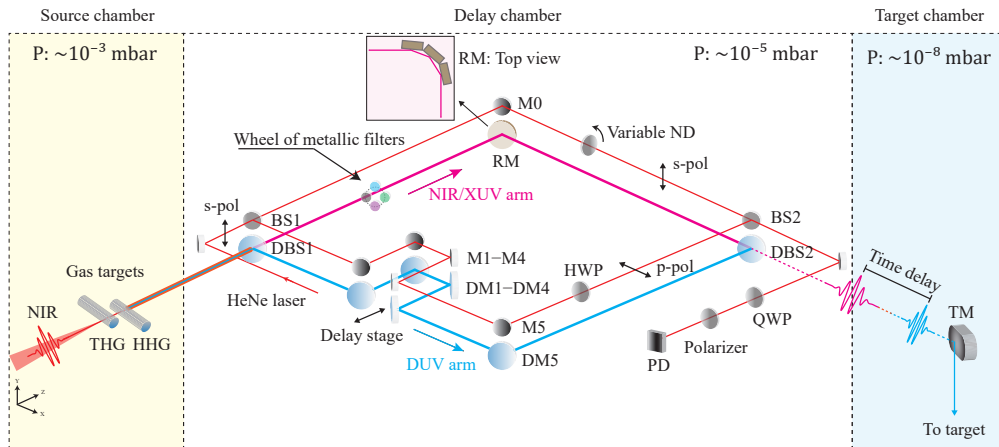


Figure 4.1: Layout of the experimental setup. A scheme for collinear generation is illustrated, as well as a method for active stabilization. The upper-layer contains a reference in-loop (IL) interferometer for active phase stabilization: the lower-layer contains the main interferometer for the pump-probe experiment using a DUV and XUV beam. THG: Third-order harmonic generation, HHG: High-order harmonic generation, DBS: dichroic beam splitter, BS: He-Ne beamsplitter, M: silver mirror, RM: triple rhodium mirror (75° angle of incidence per segment), DM: dichroic mirror, TM: Toroidal mirror, HWP: Half-wave plate, QWP: Quarter wave plate, PD: Photodiode

In Fig. 4.2, a detailed view of the gas cell is shown, indicating the entrance and exit holes for the laser beam. The drilled holes on the gas cell have small diameters of $200\ \mu\text{m}$ for the in- and outgoing beams, respectively. Additional two introversive conical gas barriers were installed to keep the gas flow into the other chambers as

low as possible. This geometry furthermore reduces the XUV propagation distance in the comparatively high-pressure environment thus decreasing absorption of the XUV photons.

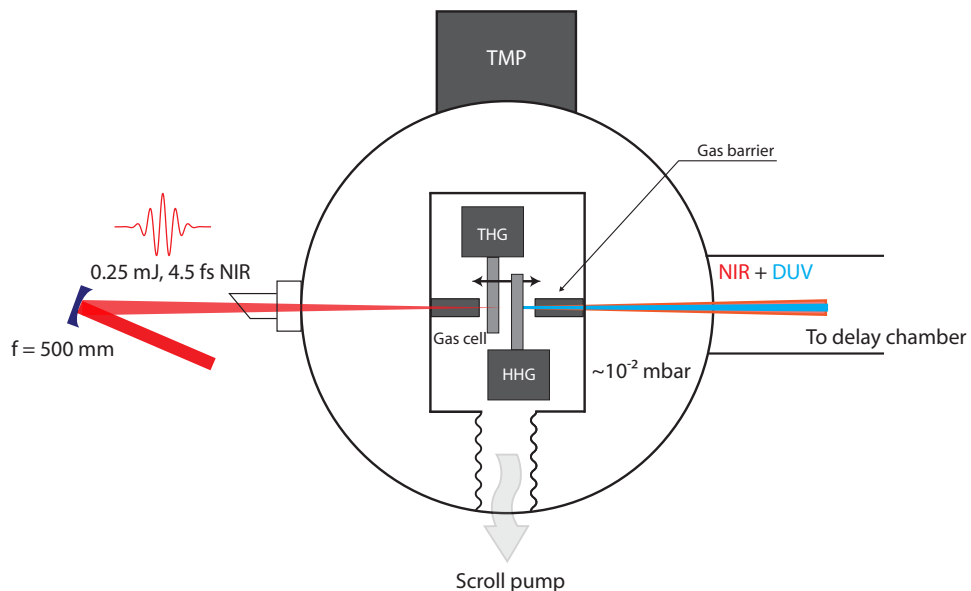


Figure 4.2: Schematic illustration of the source chamber. The gas cell for THG and HHG is housed in a small chamber, nested inside a larger main chamber. TMP: turbo molecular pump

The gas ballast in the target chamber was removed with a 300 liter/sec TMP, in combination with a side channel-pump, providing pressure values of 10^{-8} mbar in the target chamber and 10^{-5} mbar in the delay chamber. The hole size was sufficiently large enough to let the driving laser pass through it without clipping. With this configuration, we were able to maintain a 10^{-2} mbar vacuum level inside the main chamber while applying up to 2 bar gas pressure in the THG cell.

The gas cell is a 3-mm inner-diameter ceramic tube and has a mechanically predrilled (with CO₂ laser) 200 μm diameter hole for laser propagation. One end of the tube is sealed with an epoxy. The ceramic tube was chosen because it is resistant to damage caused by the focused strong NIR laser pulses.

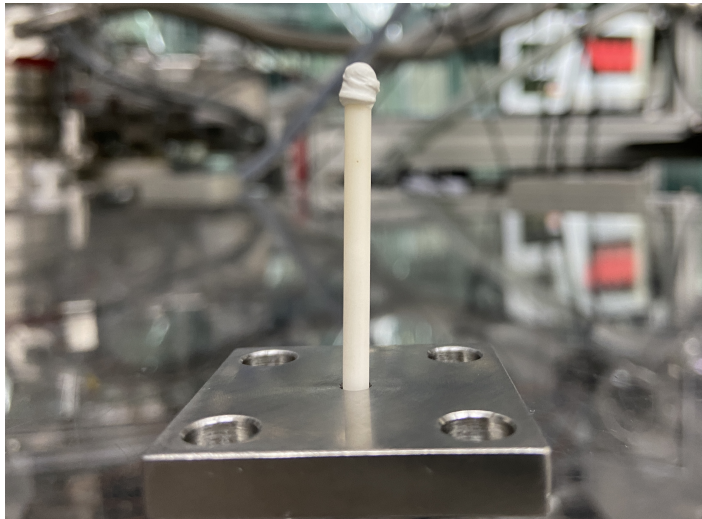


Figure 4.3: Ceramic gas cell for the THG and HHG experiment.

The measured focal spot size at the focus was 100 μm with a Rayleigh range of 9.2 mm. The input laser pulse energy in front of the Brewster window entrance was 0.25 mJ and the estimated peak intensity at the focus was on the order of $\sim 1.2 \times 10^{15} \text{ W/cm}^2$. Depending on which type of experiment and the samples of molecules under investigation, we generated either THG or HHG or both of them simultaneously by varying the applied gas pressure inside the gas cell. In the case of simultaneous THG and HHG, we utilized a collinear generation scheme [32] where two static gas cells were placed at the focus of driving laser (see Fig 4.2). Each gas cell could be positioned independently by using a motorized 3-axis stage from outside of the vacuum chamber for fine tuning the harmonic yields.

After the source chamber, the generated DUV, XUV and residual fundamental NIR pulses co-propagate into the delay chamber where a double-layer Mach-Zehnder

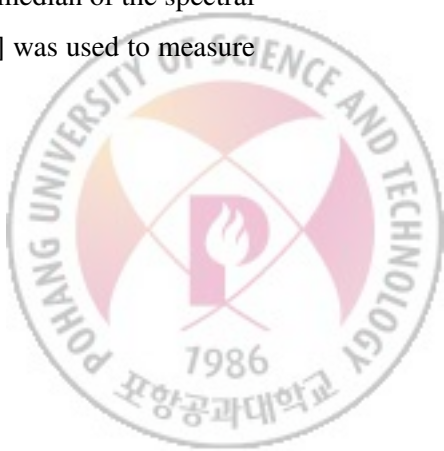
interferometer system provides a variable, actively phase-stabilized pump-probe delay. Inherently different divergences of the fundamental NIR, DUV and XUV pulses allow us to separate them spatially using a perforated dichroic beam separator (DBS1 in Fig. 4.1, (Layertec GmbH)) with a hole of 1.0 mm diameter, through which the XUV and residual NIR pulses can pass, whereas whereas >90% of the DUV beam is reflected off. Thin metallic filters such as Al and Zr (a wheel of metallic filters in Fig. 4.1) allow the XUV pulses to transmit, while blocking the remaining small portion of the DUV and fundamental NIR pulses. The residual NIR in the DUV arm is effectively suppressed by utilizing the reflectivity properties of the UV separators and dielectric mirrors ($R > 99\%$ at 270 nm, $R < 10\%$ at 405–850 nm) with a total of nine reflections from the DUV optics, resulting in NIR suppression of more than 99.99%. The thin metal filters in the XUV arm (150–300 nm thickness) suppress the NIR and DUV transmission by at least nine orders of magnitude, allowing for essentially perfect separation of the DUV and XUV beams for pump-probe experiments. The DUV and XUV pulses are then combined again at the second perforated dichroic beamsplitter (DBS2 in Fig. 4.1), which has a 1.5 mm diameter hole. For the high-resolution time-resolved experiments, we established the Mach-Zehnder type double-layer interferometer (DLI) setup where the upper-layer interferometer serves as a reference beamline for phase stabilization and delay scan using an intensity-stabilized He-Ne laser whereas the lower-layer interferometer serves for the actual pump-probe experiments using the generated ultrashort DUV and XUV pulses. The details of the phase stabilization method will be described in Section 4.5.2. The combined beams are then focused by a nickel-coated toroidal mirror into an interaction chamber where the interaction region is located between the repeller and extractor plates of a velocity map imaging (VMI) spectrometer. In the interaction chamber, the sample under study can be injected either through a supersonic gas jet from the top of the interaction chamber or through an effusive gas jet which is integrated into the repeller plate of the VMI spectrometer. More discussions about the VMI setup can be found in Section 4.6

4.3 Third-order harmonic generation

When biologically relevant molecules are exposed to UV light, they become electronically excited or ionized, initiating a complex chain of events [33, 34]. To investigate these intricate interactions and obtain a comprehensive picture of the dynamical behavior of electronically excited states in biologically relevant molecules, reliable ultrashort UV sources operating in the DUV range are required. DUV and VUV generation has been accomplished via a variety of techniques, including four-wave mixing [35], filamentation [36], quasi phase-matched THG in a gas via ultrasound, optical parametric amplification [37] and dispersive wave emission in a hollow-core waveguide [38]. Numerous studies have been conducted recently on frequency upconversion in gases using focused few-cycle NIR pulses to generate DUV pulses in a noble gas-filled cell [39, 40]. However, producing intense, few-cycle DUV pulses remains a technical challenge that requires improvements. Previously, THG works were primarily focused on achieving a shorter pulse duration, and the details of the THG process were not discussed extensively. In this regard, the THG process lacks information on the details of the THG optimization process. In this section, we will discuss the effective THG in argon gas by optimizing various parameters such as gas pressure, gas type and cell position.

4.3.1 Experiments

For the THG optimization experiments, we disconnected the delay chamber and installed another Brewster window for the exit as shown in Fig 4.4. In this experiment, a 5-fs, 0.23-mJ NIR laser with a mean photon energy of 1.7 eV was used (see Fig 4.5 (a) Fundamental). The mean photon energy was defined by the median of the spectral intensity distribution. The dispersion scan (d-scan) method [22] was used to measure the pulse duration.



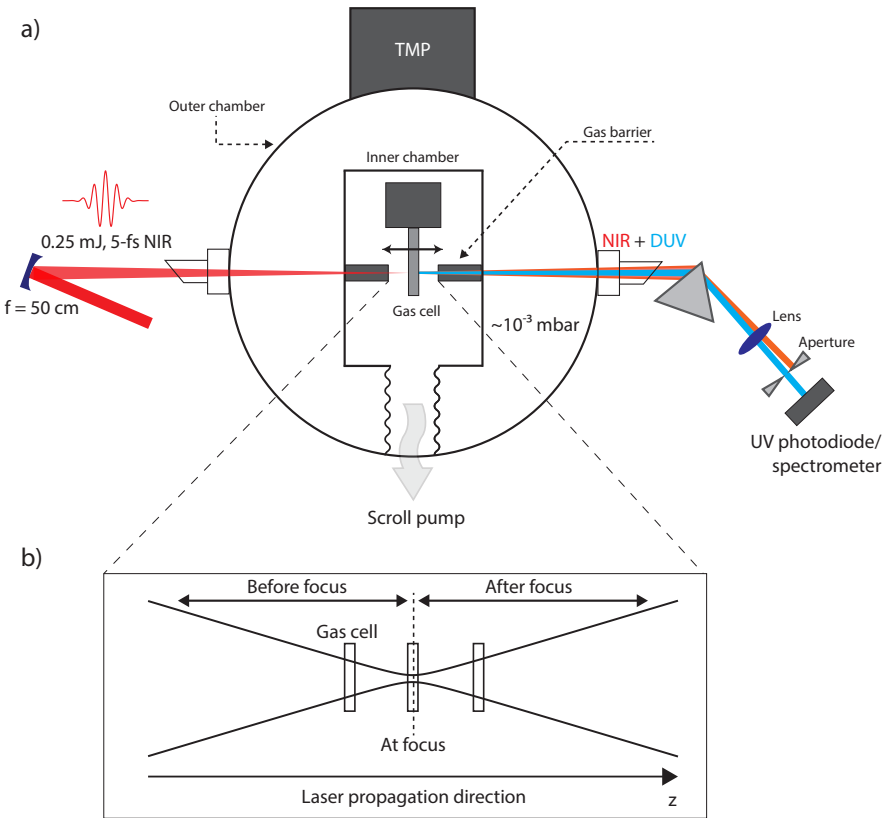


Figure 4.4: (a) Schematic experimental setup. A gas cell for THG is housed in a small chamber, nested inside a larger main chamber. (b) Geometry of the laser beam near the focus. z_0 represents the gas cell position. A negative z_0 value means the gas cell is positioned before the laser focus and vice versa. The laser focus is at $z_0 = 0$ mm

A $f = 500$ mm spherical mirror was used to focus the few-cycle laser into a quasi-static gas cell (3-mm-thick inner diameter, 300 μm hole diameter), as shown schematically in Fig 4.4. The beam diameter at the focus was measured to be $\sim 100 \mu\text{m}$ diameter (full width at $1/e^2$ maximum). The estimated peak intensity at the focus was on the order of $\sim 1.2 \times 10^{15} \text{ W/cm}^2$. The gas cell was placed on a motorized XYZ stage so that the central location of the gas cell with respect to the laser focus could be controlled in vacuum. Using an UV-grade fused silica prism and an aperture, the generated

third-order harmonics were separated from the fundamental NIR laser and collected by a lens to an absolutely calibrated UV photodiode for energy measurements, or to a UV-NIR (200-1100 nm, HR4000) spectrometer for spectral measurements. The laser focus position inside the source chamber ($z_0 = 0$ mm) was determined by measuring the mean photon energy of transmitted NIR spectra as a function of the cell position when 0.2 bar Ar gas was supplied in the cell (Fig. 4.4 (a)) while a pair of wedges was used to optimally compress the pulse duration by using the dispersion scan result.

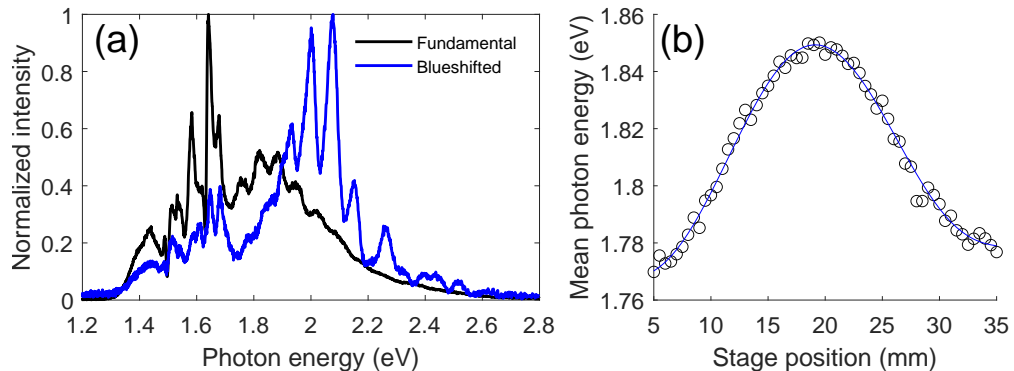


Figure 4.5: (a) Spectra of NIR laser before and after transmission through the gas cell, measured when the gas cell was positioned at the tightest focus position. The gas cell was supplied with argon gas. The transmitted NIR spectrum is showing a spectral blueshift (higher photon energy). (b) Mean photon energies of the transmitted NIR laser as a function of the cell position. The amount of blueshift was used to determine the best focus position $z_0 = 0$ mm, which is 18.25 mm stage position.

The gas cell position in the laser propagation direction was changed by the motorized linear stage on which the entire gas cell unit was mounted. The author developed a Labview program to collect data and automate the cell position dependency experiment. The spectral blueshift experimental result is shown in Fig 4.5 (b). From the experiment, the absolute focus position ($z_0 = 0$ mm) was judged as 18.25 mm stage position (Fig. 4.5 (b)), at which the largest amount of spectral blueshift was observed.

Then, the generated DUV energies were measured by changing the cell position (z_0). As indicated in Fig 4.4 (b), the gas cell at $z_0 = 0$ mm means that the gas cell is positioned at the laser focus and the negative z_0 value indicates the gas cell location being in front of the laser focus.

Fig 4.6 shows the measured DUV energies [(a) and (b)] and spectra [(c) and (d)] as functions of the gas cell position, for 2-bar Ne [(a) and (c)] and 0.8-bar Ar [(b) and (d)] gas targets. Fig 4.6 (e) and (f) show the measured DUV energies when the supplied gas pressures were changed at fixed cell locations. Reflection losses from the windows, prism, and lens, were considered in the data, as shown in Fig. 4.6 (a) and (b). In the case of Ne gas, the highest DUV energy was generated at the laser focus, as shown in Figs. 4.6 (a) and (c). In contrast, the results from Ar gas in Figs. 4.6 (b) and (d) show that the DUV yield (equivalent to DUV pulse energy) was the lowest at the laser focus while two maxima were located on either side of the laser focus. For a qualitative explanation of this cell position dependence, the THG yield was estimated numerically (Fig. 4.7 (c) and Fig. 4.7 (d)) based on a zeroth-order approximation, which is proportional to the product of neutral atomic density, the cube of the electric field strength, and the $\chi^{(3)}$ of the corresponding atom. The Ammosov-Delone-Krainov (ADK) [41] tunneling ionization rate was used to estimate the depletion of the neutral atoms. The experimental result is consistent with the numerical estimation shown in Fig. 4.7, in which the ionization of Ne atoms was not significant (Figs. 4.7 (a), density of neutral atoms) compared to the Ar case (Figs. 4.7 (b), density of neutral atoms). As estimated by the numerical calculation shown in Fig. 4.7 (b), a strong depletion of Ar atoms constitutes the low DUV yield at the focus.



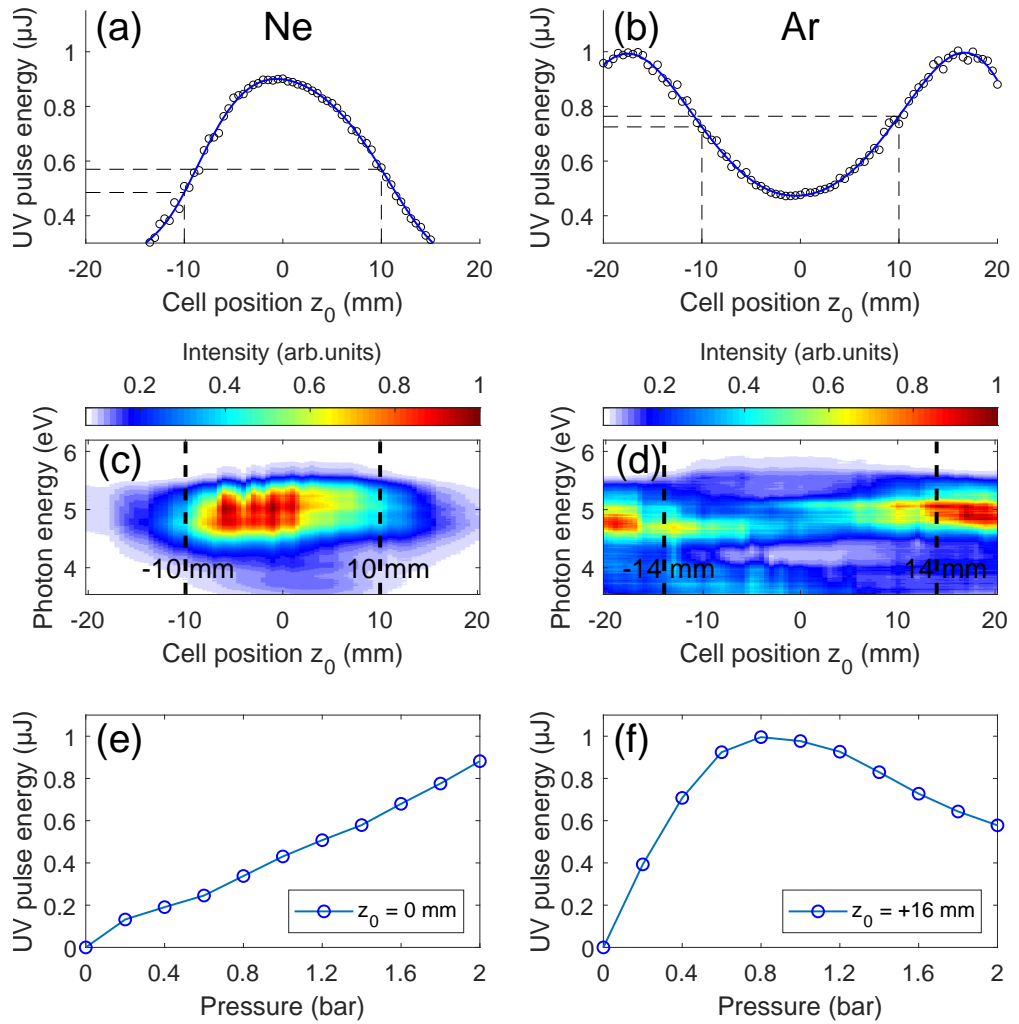


Figure 4.6: DUV pulse energies and spectra versus gas cell position relative to the laser focus: (a), (c) Ne gas and (b), (d) Ar gas. DUV pulse energies at the best gas cell position for different gas pressures: (e) Ne and (f) Ar.



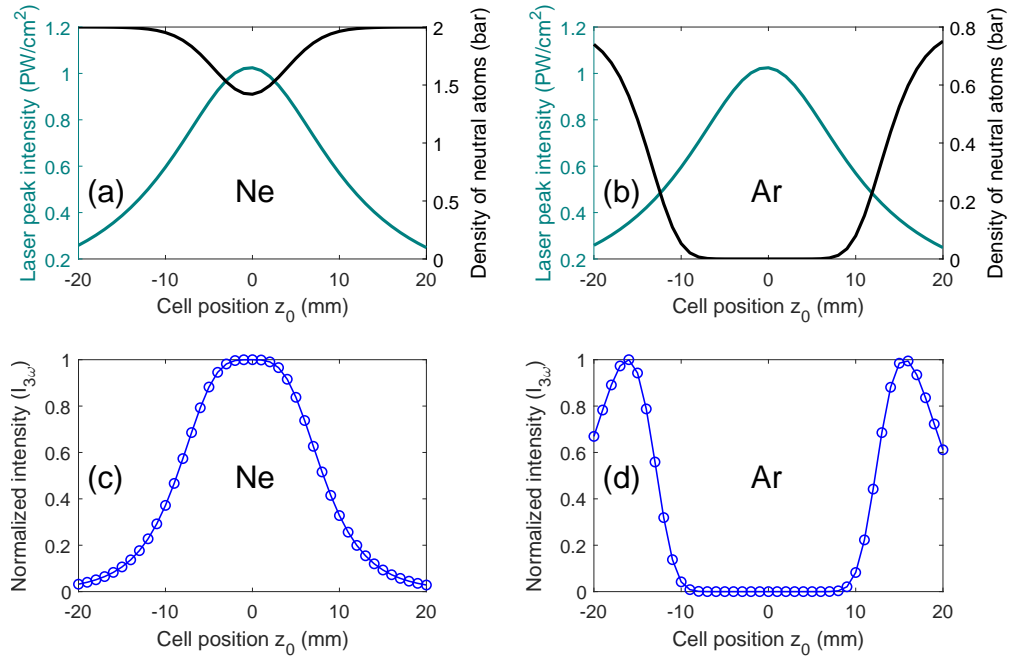


Figure 4.7: Neutral density and THG yield. (a) and (b) show the variation of neutral-atomic densities and laser intensity for different cell positions. (c) and (d) are estimated THG yields, indicating that the maximum deep-UV yield is expected when the cell is placed off the laser focus in the case of Ar. For Ne (a), 25% of the neutral atoms are expected to be ionized when the cell is positioned at the laser focus. For Ar (b), the neutral atoms are totally depleted.

Based on this result, we fixed the cell position at $z_0 = +16$ mm in the case of Ar gas, where a maximum of the DUV yield was observed. The gas pressure was then varied from 0 to 2 bar. The highest DUV yield was observed at 0.8 bar. When a much higher pressure was applied, the DUV yield was reduced due to the increased plasma density and, hence, the increased nonlinearity. For Ne, with the cell located at the focus position ($z_0 = 0$ mm), a gradual increase in DUV yield was observed by supplying higher gas pressures as shown in Fig. 4.6 (e), which is in agreement with other experimental results [39]. Since Ar was yielding the UV generation more efficiently,

we placed the gas cell at an optimum position ($z_0 = +16$ mm) and measured DUV energy for 30 min. The result is shown in Fig 4.8.

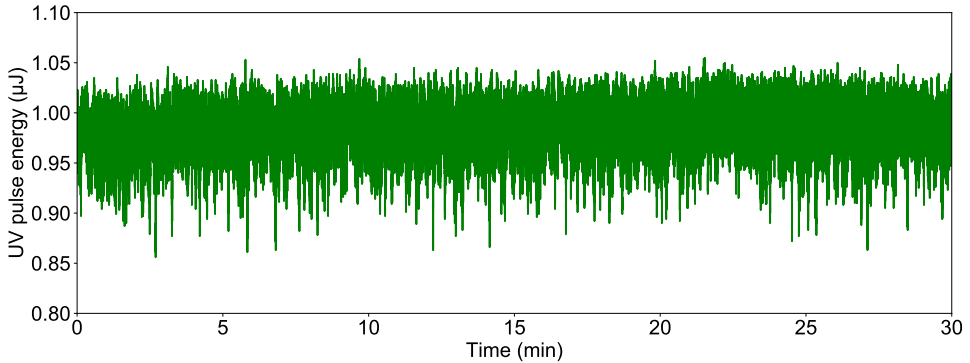


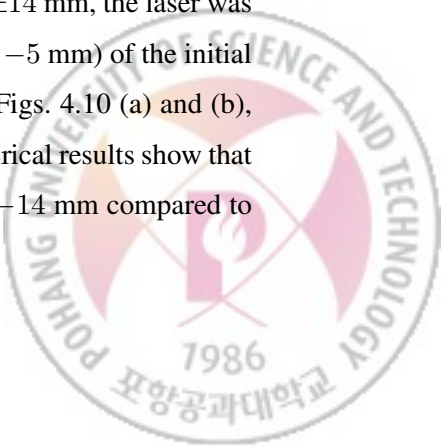
Figure 4.8: Power logging of the generated DUV is shown. During the 30-min measurement, pulse energy stability was less than 2% (RMS).

Ar has a larger third-order susceptibility ($\chi^{(3)} = 0.0441$ (a.u.)) and a lower ionization energy ($I_P = 15.7$ eV) than Ne ($\chi^{(3)} = 0.00312$ (a.u.), $I_P = 21.5$ eV). Therefore, the results from Ar show relatively high DUV yields even in low gas pressures (below 1 bar). As a compromise, the neutral Ar atoms are significantly depleted at the focus as shown in Fig. 4.7 (b). In general, an ionized atom has a lower susceptibility than the neutral atom, resulting in an inferior production of UV photons. Therefore, when Ar is used as a THG medium, it is not recommended to place the gas target at the laser focus. Hence, scanning the cell position is an essential task to find the optimal condition for THG.

The third-order polarizability P_3 , and the resultant THG can be understood as a perturbative phenomenon with a simple analytic formulation $\mathbf{P}_3 \propto \chi^{(3)} \mathbf{E}^3$, with $\chi^{(3)}$ and \mathbf{E} are the third-order susceptibility of a material and a driving field strength, respectively. The asymmetry in the DUV yield (dashed lines in Figs. 4.6 (a) and (b)) with respect to the gas cell location was noted, which cannot be reproduced with the zeroth-

order approximation shown in Figs. 4.7 (c) and (d). When the gas cell is placed in front of the laser focus, the DUV yield is slightly smaller than when the gas cell is placed behind the focus regardless of the gas type. Furthermore, the DUV spectra are significantly different depending on the cell position. Hence, cross-sections (or spectra) were taken at several gas cell positions (dashed lines in Figs. 4.6 (c) and (d)) to examine the variations in the generated DUV spectra more closely. A notable difference depending on the gas cell location was observed (Fig. 4.9 (a)). The DUV spectrum taken from the gas cell condition at $z_0 = +14$ mm exhibits a spectral blueshift compared to the spectrum from the condition at $z_0 = -14$ mm. The same tendency was observed from the Ne result (Fig. 4.9 (c)). To understand these experimental observations, the propagation of an ultrashort optical pulse in a gas medium was simulated by numerically solving the nonlinear envelope equation under the slowly evolving wave approximation [42]. In the simulation, nonlinear effects were included, such as nonlinear absorption, plasma dispersion and the third-order susceptibility of the medium. While a focused laser beam has a symmetric intensity distribution with respect to the laser focus, nonlinear laser-matter interaction mechanisms can be asymmetric between the gas cell positions, being placed before and after the laser focus. In the present THG results, the asymmetric blue-shifting tendency was reproduced by a simulation, as shown in Figs. 4.9 (b) and (d). The simulated spectral shape deviates from the experimental observations because of the reduced detection efficiency of the near vacuum-UV components (above 5.7 eV) compared to the DUV components.

Fig 4.10 provides more details of the simulation results for the Ar target, when the cell was located at $z_0 = \pm 14$ mm. Fig 4.10 (a)-(d) present the results for $z_0 = -14$ mm, i.e., when the gas cell was placed 14 mm before the laser focus. Figs. 4.10 (e)-(h) present the simulation results for $z_0 = +14$ mm. For both $z_0 = \pm 14$ mm, the laser was strong enough to ionize the atoms at the leading edge ($z - z_0 \approx -5$ mm) of the initial gas profile (dashed lines in Figs. 4.10 (a) and (e)) as shown in Figs. 4.10 (a) and (b), and Figs. 4.10 (e) and (f). In Fig. 4.9, the experimental and numerical results show that the blueshift is less significant when the cell is located at $z_0 = -14$ mm compared to



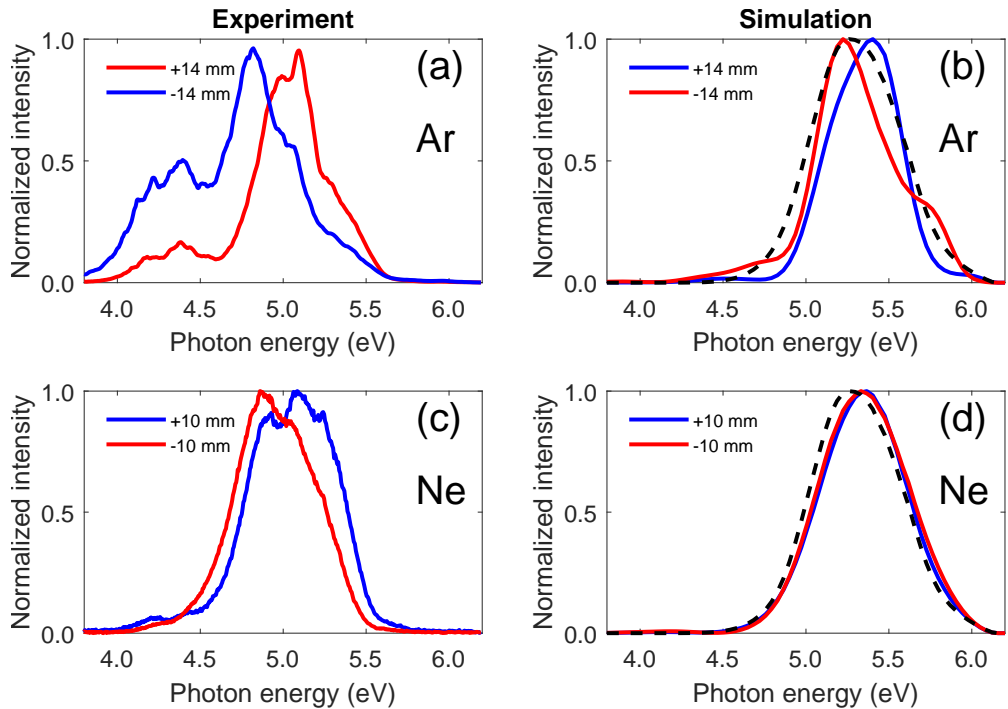


Figure 4.9: (a) and (c) experimental spectra taken at the dashed lines in Figs. 4.6 (c) and (d), respectively. (b) and (d) DUV spectra obtained from the simulation performed using the experimentally observed laser parameters. More details on the simulation results are given in Fig. 4.10. The dashed lines in (b) and (d) show an analytical solution of the third-harmonic spectrum obtained by Fourier transforming the cube of the fundamental laser $E(t)$ in the temporal domain.



when $z_0 = +14$ mm. This is because the laser beam interacts with the leading edge of the gas profile before the laser is tightly focused. The generated electron density is one order of magnitude smaller than in the case of $z_0 = +14$ mm, as shown in Figs. 4.10 (a) and (b). Figs. 4.10 (c) and (d) show the on-axis spectral intensities of the NIR (c) and DUV (d) lights for $z_0 = -14$. Although the laser beam becomes naturally stronger by the focusing geometry, the relatively low-density plasma causes the beam to diverge, resulting in the reduction of the on-axis NIR intensity over the first half of the propagation, the beam then becomes stronger again in the next half of the propagation. The mean photon energy of the NIR light is blueshifted and then returns to its initial spectral shape because low-frequency light diverges further in the plasma. On the other hand, when the gas cell is at $z_0 = +14$ mm, the atoms are irradiated with a diverging laser beam. The approximately 10 times higher 0.07 bar of the atoms can be ionized at the leading edge of the gas profile. The beam divergence is augmented by plasma-induced refraction at the leading edge of the target profile. The plasma formation is more localized (Fig. 4.10 (e), red curve) compared to when the gas cell is at $z_0 = -14$ mm (Fig. 4.10 (a)). The overall on-axis NIR intensity (see colorbar scale) is reduced by a factor of four, as shown in Fig. 4.10 (g). Owing to the significant ionization at $z - z_0 \approx -5$ mm and the localized plasma, the NIR fundamental spectrum becomes significantly blue-shifted at this point already as indicated by the dashed line in Fig. 4.10 (g). The frequency-shifted laser then propagates through the gas medium and generates DUV light through the third-order nonlinear process. Therefore, the blueshifted DUV yield increases gradually after $z - z_0 \approx -5$ mm (Fig. 4.10 (h)).



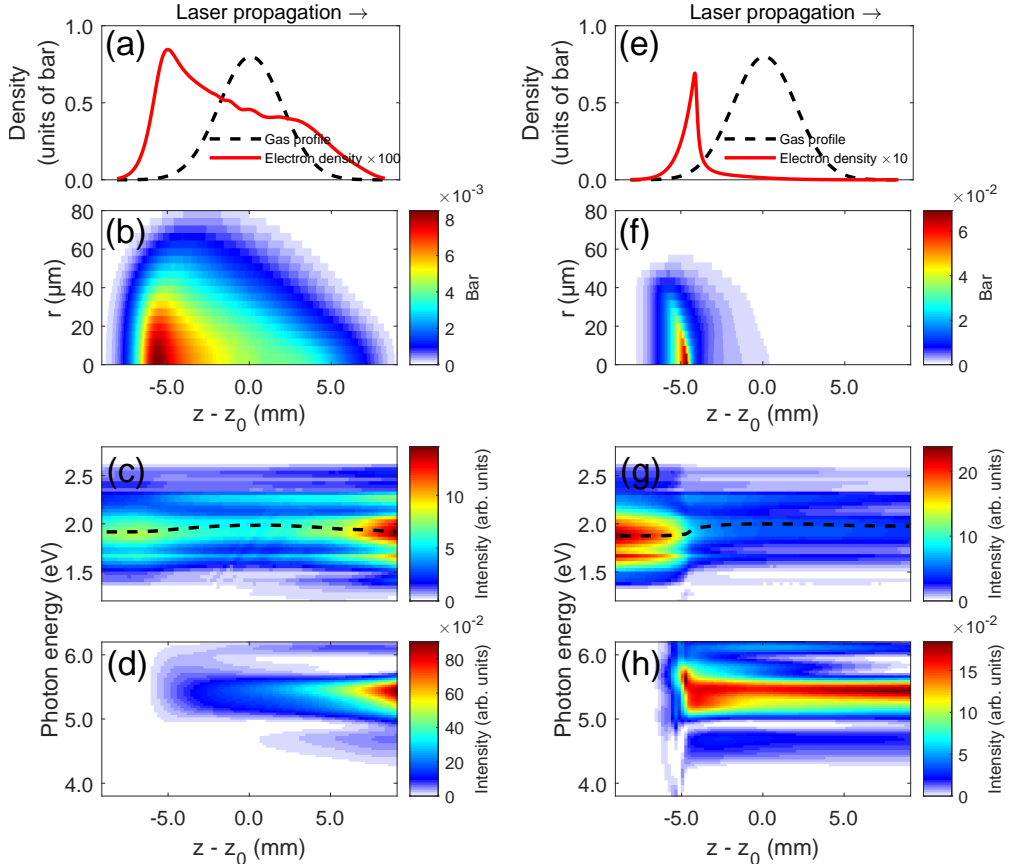


Figure 4.10: Simulated nonlinear DUV generation dynamics in Ar. The left column [(a), (b), (c), and (d)] and the right column [(e), (f), (g), and (h)] panels are the results for the two different cell positions: $z_0 = -14$ mm and $+14$ mm, respectively. (a) and (e) show the z -dependent on-axis ($r = 0$) electron densities after the laser has passed. (b) and (f) are the two-dimensional (r and z) electron density profiles. The spectra of propagating fundamental [(c) and (g)] and the third-order harmonic [(d) and (h)] were taken from the on-axis ($r = 0$). In (c) and (g), the mean photon energies of the fundamental laser are indicated by the dashed lines in order to visualize the blueshift.

In both cases of $z_0 = \pm 14$ mm, as can be seen in Fig 4.10 (d) and (h), the DUV yield increases gradually as the beam propagates through the medium. The presence

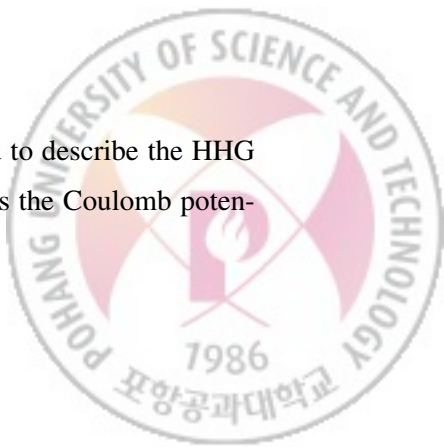
of plasma generated in the gas cell has a significant impact on the DUV efficiency due to the phase mismatch. As discussed above, the dashed lines in Figs. 4.6 (a) and (b) indicate a higher yield for $z_0 > 0$. When the cell is located before the laser focus ($z_0 < 0$), the plasma is distributed over the entire interaction region (Figs. 4.10 (a) and (b)), which makes the phase mismatching dominant. In the case of $z_0 > 0$, the plasma is localized at around $z - z_0 \approx -5$ mm with a relatively high electron density, as shown in Figs. 4.10 (e) and (f). Therefore, the plasma-induced phase mismatching occurs only at the localized position.

4.4 High-order harmonic generation

When the intense laser field interacts with atoms, binding electrons can be tunnel ionized and liberated. A fraction of these liberated electrons follow the oscillating electric field, and when the electric field changes direction and brings them close to the parent atom, electrons can recombine with it and release the gained energy as a photon. This process is called *high-order harmonic generation* (HHG). Emitted photon energies can vary and be tuned depending on the driving laser characteristics [31], but they are typically in the XUV regime when Ti:sapphire based NIR lasers are used. Typically, HHG is accomplished by focusing intense, ultrashort laser pulses into a gas target (atoms or molecules) [43]. HHG has been also recently produced from solid [44, 45] and liquid targets [46]. As stated in the introduction, the Keldysh parameter for gas-based HHG should be greater than 1 in order to tunnel ionize the binding electrons. However, a variety of other experimental parameters, including the laser wavelength, focusing geometry, and pulse duration, can all have an effect on the HHG process [47].

4.4.1 The simple man's model

The well-known Simple man's model (SMM) [48] is used to describe the HHG process, see Figure 4.11. At first, a strong electric field distorts the Coulomb poten-



tial, allowing electrons to tunnel ionize. In the second step, when the released electron wave-packet propagates in the oscillating electric field and reaches the continuum state, it can obtain energy from the driving laser field. In the third step, as the electric field changes direction, electron wavepackets are driven back and closer to the parent ion, where they recombine by emitting a photon. The resulting HHG spectrum exhibits a variety of distinct characteristics. Every half cycle of the electric field, the above-described three-step process occurs in the linearly polarized laser field, yielding an odd harmonics comb based on the driving laser's photon energy. For low-order harmonics, where the perturbative regime can be used to describe the harmonic generation process, the conversion efficiency rapidly decreases until it reaches a plateau region where it remains relatively constant over tens of orders. At the high energy end of the spectrum, a cut-off region exists where harmonic generation efficiency begins to decline and eventually vanishes. Figure 4.13 illustrates these major characteristics of HHG.

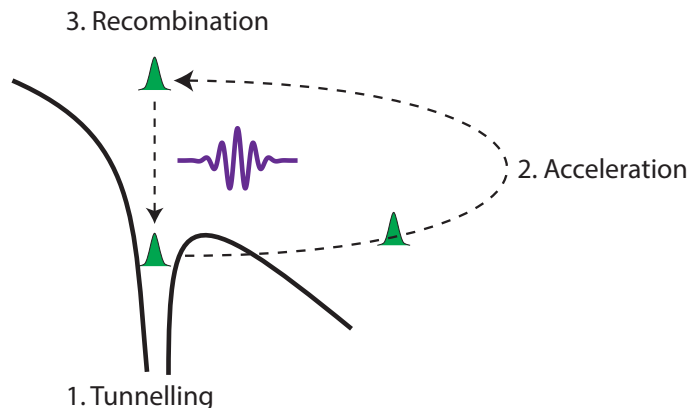


Figure 4.11: The three-step simple man's model, which includes tunnel ionization, free acceleration, and high-energy photon emission upon recombination.



4.4.2 Experiment

Similarly to the THG experiment, the HHG experiment used the same 5-fs, 0.2 mJ NIR laser with a mean photon energy of 1.7 eV. Details of the experimental setup can be found in Section 4.3.1. The only difference is in the position of the HHG cell in relation to the laser focus, the applied gas pressure, and the gas type. We used Ne gas as a medium for the HHG, and the gas cell filling pressure was in the range of 100 mbar or less. As we previously discussed, in terms of the underlying physical mechanism, low-order harmonic generation (e.g., THG) has typically been characterized by perturbation theory. In contrast, high-order harmonic generation (HHG) is a highly nonperturbative process in which the density of freed electrons influences the propagation of the driving NIR field, affecting its spatiotemporal properties as well as the coherent properties of the generated XUV via the phase-matching effect. For the HHG experiment, the cell location with respect to the laser focus was scanned and placed about 3 mm after the focus, where the highest XUV photon count was measured. The XUV-CCD camera (Andor iKon-M) installed in the delay chamber was used to characterize the generated HHG beam profile, whereas the number of XUV photons was determined using a XUV photodiode (AXUV-100G).

The generated XUV beam was routed to the interaction chamber via a rhodium coated turning mirror (Fig. 4.1, RM) and then focused onto the VMI spectrometer via a nickel coated toroidal mirror. A flat-field grating spectrometer was installed in the interaction chamber, as shown in Fig. 4.12, for spectral characterization.



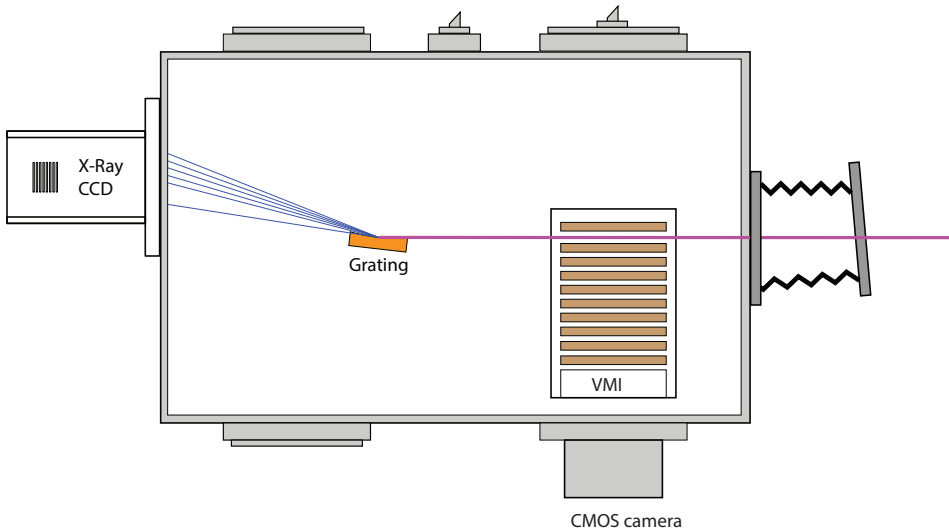


Figure 4.12: Schematic drawing of the interaction chamber. A VMI and a flat-field grating spectrometer are shown. The XUV beam is indicated by the violet color.

The resulting XUV spectrum is shown in Fig. 4.13 after energy calibration using Al absorption edge (dashed curve). Temporal characterization of the XUV pulses can be done via streaking in the future. Based on previous work with comparable driving pulses and XUV spectra, the XUV pulse duration is expected to be in the order of a few 100 as [49]. The photon flux of the XUV source is $\sim 2.5 \times 10^7$ photons/pulse at the target chamber, taking into account the losses from the metallic filters and rhodium mirrors.



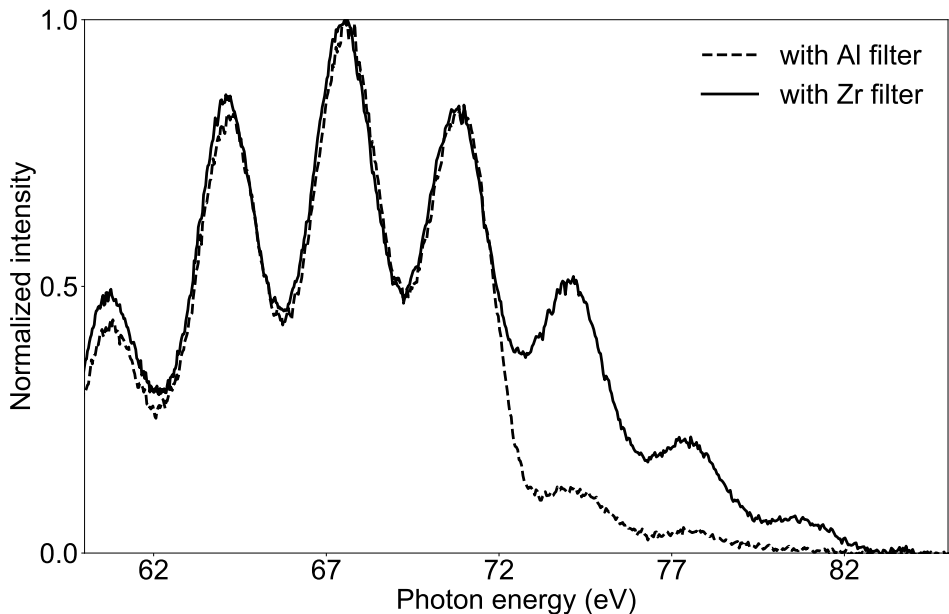


Figure 4.13: Generated HHG spectrum measured in the interaction chamber with two different filters. An Al filter is used to calibrate the HHG spectrum using its well known absorption edge.

We successfully generated DUV and XUV beams in the chemical physics beamline by focusing an intense few-cycle NIR laser into a gas cell filled with noble gases using the frequency upconversion method. The gas type, cell position, and gas pressure were the primary differences between the THG and HHG. In the case of THG, the gas cell was 16 mm ahead of the laser focus, whereas in the case of HHG, the gas cell was 3 mm after the focus to satisfy phase-matching conditions. The DUV was generated using a gas cell filled with 0.8 bar argon gas, which produced 1 μ J pulse energy in the 220-310 nm range. For XUV, a gas cell was filled with < 0.1 bar Ne gas, resulting in $\sim 2.5 \times 10^7$ photons per pulse. In terms of photon energy, the readily available light sources generated in the chemical physics beamline are shown in Fig. 4.14.

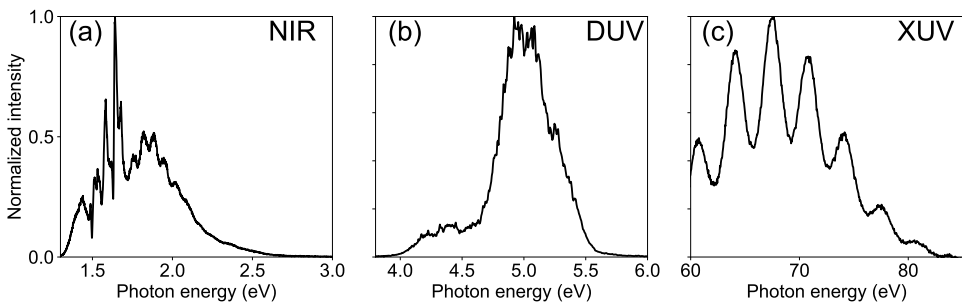


Figure 4.14: (a) Driving few-cycle NIR laser spectrum. (b) Energy spectrum of the generated DUV and (c) XUV light.

4.5 Delay-line setup for time-resolved experiments

The pump-probe technique is a highly effective spectroscopic technique for studying the evolution of dynamic systems. However, depending on the dynamic system's time scale of evolution, different time resolutions are required. For example, studying the rotational and vibrational dynamics of molecules requires a time resolution of a tens of femtoseconds to picoseconds. Whereas studying electron dynamics within atoms and molecules requires a much higher time resolution, typically on the order of a few femtoseconds or even attoseconds. When studying ultrafast electron dynamics in atoms and molecules with femtosecond time resolution, maintaining phase stability between the pump-probe beams becomes a difficult task due to mechanical drift, acoustic and vibrational noise in the laboratory. Timing jitter between pump-probe pulses should be controlled on the attosecond time scale for high-resolution time-resolved experiments. This section discusses active and passive phase stabilization techniques, as well as a novel continuous scan phase-locked double-layer interferometer used in this beamline to achieve pump-probe measurements with superior timing stability.

Vibration control

The most relevant sources of mechanical noise and drift in the laboratory that can cause interferometer instability and thus timing jitter between the pump-probe beams. Although not all noise can be avoided, the vast majority can be significantly reduced using a variety of techniques. Thermal drifts, for example, can be reduced by controlling the temperature variation in the room, whereas mechanical noise can be greatly reduced by using vibration damping and isolation methods.

Common noise sources in the laboratory		
Noise sources	Frequency range (Hz)	Time period (s)
Acoustic noise	100-10000	0.01-0.0001
Vacuum pumps	5-25	0.2-0.04
Air compressors/conditioner	4-20	0.25-0.05
Foot traffic	0.5-6	2-0.1
Temperature change	0.0001-0.005	10000-200

We begin with passive stabilization by isolating the delay line chamber's breadboard as well as the chamber itself from mechanical noise using various types of vibration isolators. First, vibrational coupling between the delay chamber and the supporting Al frame was damped by a sorbothane sheet (SB12C, Thorlabs) capable of dumping \sim 30 Hz and higher. Second, welded bellows further reduce the vibration transmission between the delay chamber and the optical table. Finally, another vibration isolator (VIB320, Newport) was installed beneath the delay chamber breadboard and optical table to effectively suppress vibration frequencies above 9 Hz. Figure 4.15 shows a vibration isolation technique schematically.



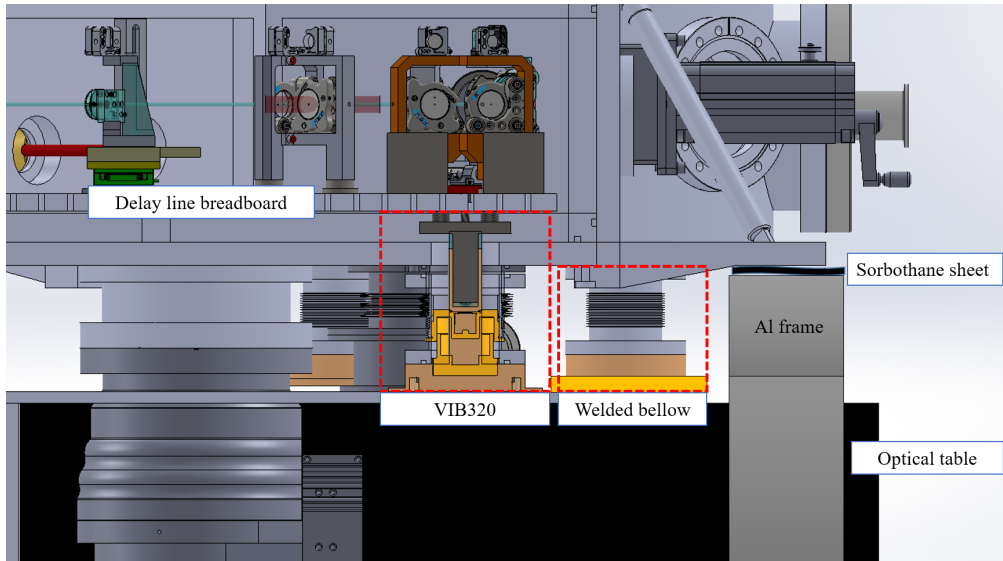


Figure 4.15: The vibration isolation technique is schematically depicted.

In Fig 4.16, the frequency domain result of a mechanical noise measurement is shown following the implementation of a passive stabilization technique using a standard fringe-based interferometer method. On the graph, noises at 60 Hz from the mains power line and 30 Hz from the scroll pump are visible, as well as other noise at low and high frequencies. Therefore, eliminating noise in the interferometric setup and achieving sub-femtosecond time jitter (or phase stability) is one of the main goals and we use a combination of active and passive stabilization methods to achieve excellent interferometric phase stabilization.



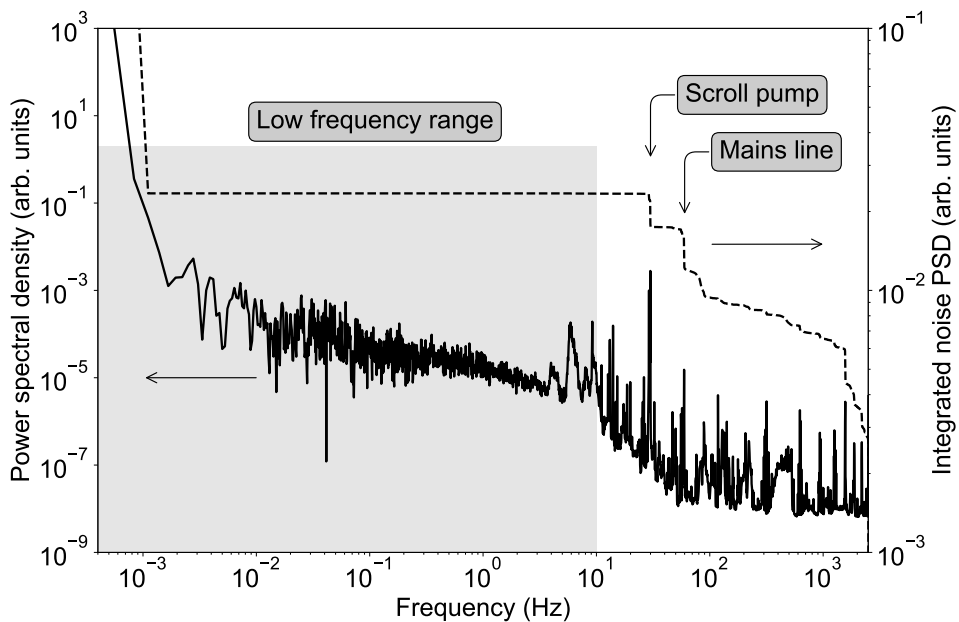
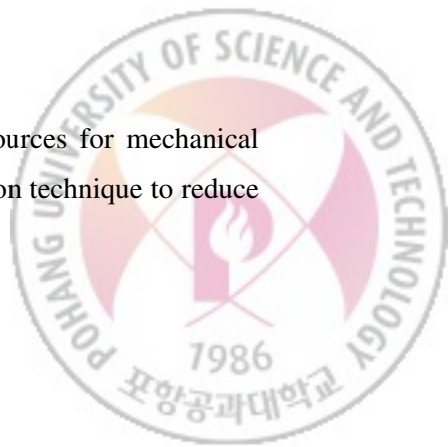


Figure 4.16: Noise sources in the laboratory. With the frequency domain analysis, noise sources can be identified using a conventional interferometer. The most significant noise contribution comes from prominent characteristic peaks at 60 Hz (mains line) and 30 Hz (scroll pump) as well as slow temperature-induced drift below 1 mHz.

The integrated PSD curve (dashed) demonstrates that low-frequency noise is negligible across a wide frequency range and only becomes significant on the long-term temperature drift scale (1mHz and below). Except for thermal drift, the majority of low-frequency drift is effectively suppressed using the previously stated passive stabilization technique.

4.5.1 Interferometer setup

After suppressing and passively stabilizing the major sources for mechanical noise and drift, we additionally implement an active stabilization technique to reduce



or remove noise which cannot be shielded passively. As previously stated, several methods for phase stabilization have been implemented and used in attosecond beamlines. Numerous active stabilization techniques have been developed and are currently being used in the case of XUV pulses combined with an NIR beam. The majority of them employ a collinear scheme [50, 51, 52] in which a reference continuous wave (CW) laser co-propagates with XUV and NIR laser beams to form an interferometric beam path. When few-cycle deep UV pulses are combined with XUV pulses in the beamline, however, such a collinear scheme with a CW laser is impossible due to spectrally incompatible dielectric and dichroic optics along the beam paths. Additionally, the relative phase between the two interferometer arms must be relocked at each delay point, as the intentional delay change disrupts the relative phase. This becomes a problem when data acquisition has to be automated, since it is frequently time-consuming. In our DUV/XUV beamline, we employ a double-layer interferometer system that enables continuous delay changes while maintaining the relative phase between the two arms. When a beamline operates in the deep ultraviolet spectral range, dielectric coated mirrors are typically used due to their high reflectivity in this spectral range. On the other hand, when performing UV pump XUV probe experiments with frequency tripled pulses, it is critical to consider how much fundamental light can be allowed to shine on the target without interfering with the experiment.

$$A \propto \frac{\sqrt{I}}{\omega} \quad (4.1)$$

$$A_{3\omega} = \frac{1}{3} A_\omega \quad (4.2)$$

where A , I and ω denote the amplitude of the vector potential, the intensity of the electric field and the frequency of the laser field, respectively. With this relationship in mind, we carefully selected a DUV dielectric mirror with a high reflectivity in the DUV and a very low reflectivity in the visible range ($R > 99\%$ at 270 nm, $R < 10\%$ at 405–850 nm).

Unfortunately, the disadvantage of these dielectric mirrors is that they preclude the use of collinear schemes for active phase stabilization due to their low reflectivity

in the visible range, since the narrow-band stable CW laser sources typically used as a phase reference operate at visible wavelengths (e.g. Helium-Neon lasers). The dielectric mirrors in the DUV arm (see Fig 4.1), in particular, have a $< 10\%$ reflectivity at > 350 nm and thus require a unique stabilization method. A disadvantage of the phase stabilization method based on simple interferometry is its ambiguity at extremes. In a "standard" interferometer, delay shift is converted into a sinusoidal amplitude modulation (i.e. interference). This interference is ambiguous; if the interference signal reaches an extremum and then reverses direction, we cannot determine whether the delay went backwards or forwards following that point. Between the two extremes, there is only a sub-half-wavelength range where the relationship between delay and amplitude is unambiguous. This allows us to stabilize a delay anywhere within that (small) range, but not beyond it, e.g. a few cycles away. As a result, each point of a delay scan requires relocking to the nearest half-cycle of the interference signal and does not contain information about the absolute path length. M. Hubbert *et al.* [53], overcame this obstacle by combining an interferometric stabilization method based on white light with a quadrature detection technique. This approach, on the other hand, introduces more complexity in the beamline. To overcome these technical difficulties, we implemented a double-layer interferometer (DLI) stabilization scheme, in which the upper layer acts as a reference interferometer by locking the relative phase using an intensity stabilized He-Ne laser. Another feature of the DLI is the incorporation of the accumulated Pancharatnam's phase method [54], which allows for continuous delay scanning over a long range while stabilizing the interferometer.



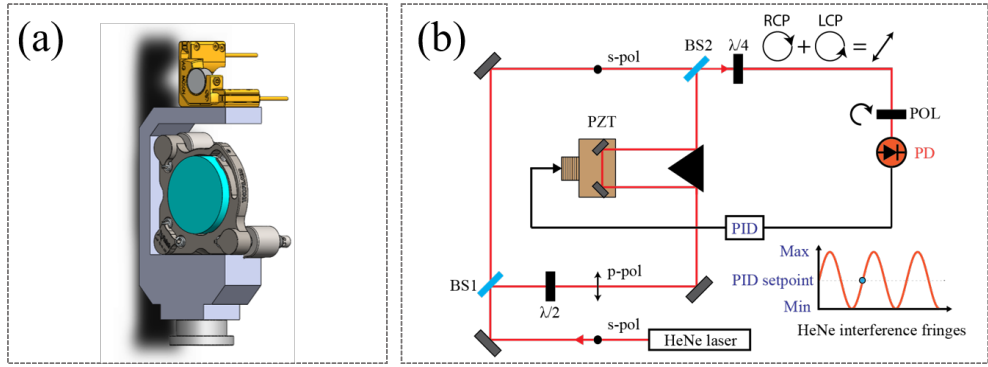


Figure 4.17: (a) Custom-designed coupled Al mirror mount for the double-layer interferometer setup. (b) Actively-stabilized continuous delay scan scheme based on Pancharatnam’s phase in the upper-layer (reference) interferometer. BS: beam-splitter, PZT: piezoelectric transducer stage, PD: photodiode, POL: polarizer, PID: proportional-integral-derivative controller, RCP: right-handed circular polarization, LCP: left-handed circular polarization.

4.5.2 Active phase stabilization

The uniqueness of the current ultrafast DUV/XUV beamline is the capability of continuous delay scanning with attosecond timing precision. For this purpose, as mentioned above, a double-layer interferometer (DLI) setup with an arm length of 1.2 m has been constructed, as shown in the mid-panel of Fig. 4.1, in which the upper layer serves as a reference in-loop (IL) interferometer to scan and stabilize the DUV/XUV delay line on the lower layer. To achieve a high degree of phase stabilization, the optical breadboard of the delay line chamber is supported by vibration isolators (VIB320, Newport), which greatly suppress the mechanical noise from various sources in the laboratory. To minimize the intensity drift of the upper-layer (IL) interferometer, which would cause a phase drift of the DUV/XUV delay, an intensity-stabilized He-Ne laser is used to provide a phase reference in the upper layer. As shown in Fig. 4.17 (a), custom-designed Al mirror mounts have been fabricated for the DLI setup to mechani-

cally link the lower- and upper-layer interferometers. Since most mechanical drifts and vibrations in both layers are correlated with this design, the phase locking in the upper-layer interferometer automatically ensures the phase locking in the lower layer. Half-inch standard silver mirrors are used in the upper layer for the He-Ne laser, whereas 1-inch dielectric mirrors and perforated dichroic beam separators are installed in the lower layer tailored for the DUV and XUV/IR pulses in the respective beam paths (see Fig. 4.1 (a)). For continuous scanning of the delay over a long range while actively stabilizing the phase in the DLI setup, we utilize the accumulated Pancharatnam's phase method [54] in the reference upper-layer interferometer. Fig. 4.17 (b) illustrates the active stabilization scheme in which an intensity-stabilized, linearly polarized (s-pol) He-Ne laser beam passes through the upper-layer interferometer. After the first beam-splitter (BS1), the polarization in one of the arms is rotated by 90 degrees with respect to the other arm using a half-wave plate (HWP). The cross-polarized beams are then recombined at the second beamsplitter (BS2) and pass through a quarter-wave plate (QWP), which converts these crossed linear polarizations into circular polarizations of opposite helicity. The superposition of the two orthogonal circular polarizations results again in a linearly polarized beam whose polarization angle now only depends on the relative optical phase between the two circular-polarization components. Effectively, this method converts a change in optical phase (or delay) into a change of the linear polarization angle, while in a simple interferometer an optical phase change results in an intensity change due to constructive or destructive interference. The advantage of this method is that the rotation of the polarization angle is directional and continuous with the optical delay, while the intensity variation due to interference in a normal interferometer changes direction after every half-cycle. By analyzing the polarization angle with a polarizer (POL) and detecting the resulting He-Ne laser intensity with a photodiode (PD), we can lock the optical delay by keeping the photodiode signal (and thus the polarization angle) at a certain value. This is achieved by using an analog proportional-integral-derivative (PID) controller (SRS SIM960) together with a piezo-electric transducer for the optical delay stage in a feedback loop with the set point set

to roughly the middle of the range between the minimum and maximum photodiode signal after the polarizer as a function of optical delay. Scanning the delay can now easily be achieved by slowly rotating the polarizer while maintaining the PID lock. Since the polarization change is continuous with the optical delay, the scan range is only limited by the reference laser's coherence length and the mechanical constraints of the optical delay stage. A full (2π) turn of the polarizer corresponds to an optical phase change of 4π , or two wavelengths of the reference laser.

To validate the performance of the DLI, for simplicity, the dielectric/dichroic mirrors in the lower layer have been replaced with Ag mirrors and the intensity-stabilized He-Ne laser is now split in two parts. One part is used in the upper layer with the PID feedback loop to stabilize and scan the interferometer, while the second part is used for the lower layer (out-of-loop, OOL) stability measurements. This second lower-layer (OOL) interferometer provides a direct performance assessment of the actively stabilized DLI, since it uses the same beam path as the DUV/XUV beams for pump-probe experiments. In addition, the He-Ne intensity is referenced by another photodiode to eliminate intensity-related drift. Figure 4.18 shows the phase stability of the DLI measured over ~ 2 h at a fixed optical delay. The signal from the upper- and lower-layer photodiodes was sampled at a 6 kHz rate (well above the relevant acoustic frequencies) and converted into optical delay units by using the He-Ne wavelength of 632.8 nm and the amplitude of both interference signals obtained from a short scan of the delay stage with the PID controller switched off.



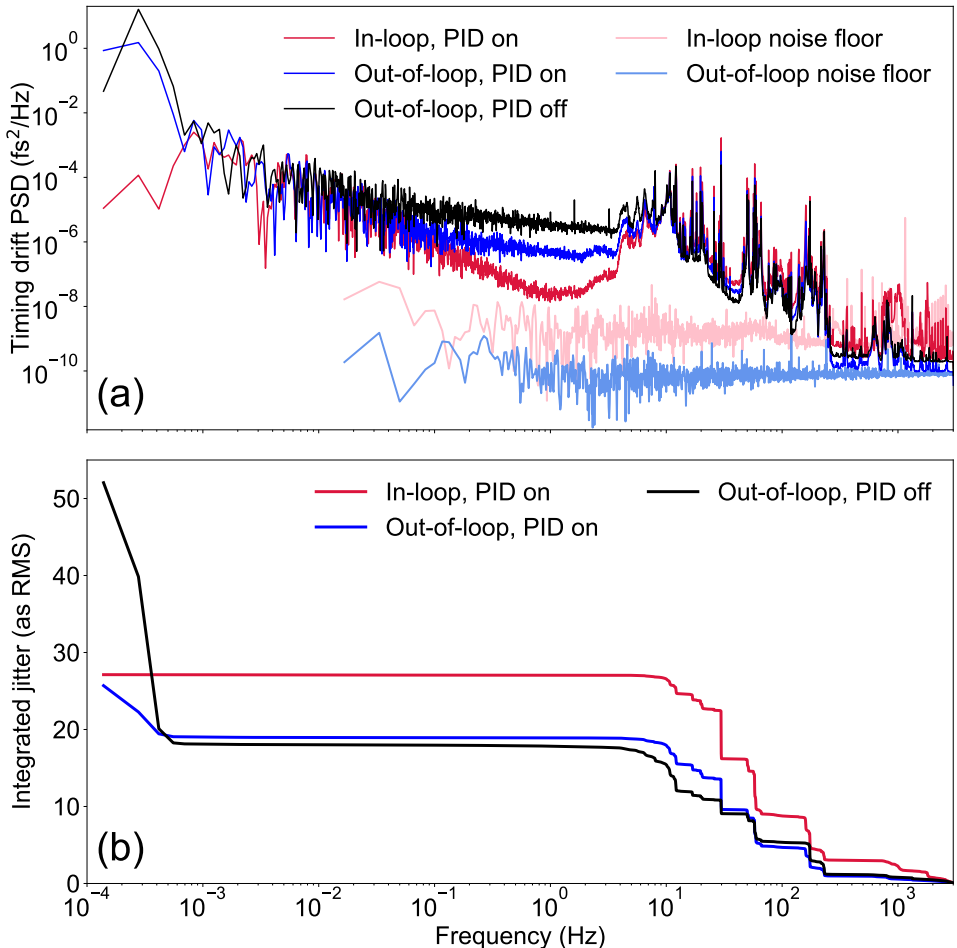


Figure 4.18: Frequency-domain analysis of the optical delay timing jitter and drift.
 (a) Power spectral density of the timing drift for the upper layer (red), lower layer (OOL) with PID control (blue), and lower layer (OOL) without PID control (green). The instrument noise floor for the respective interferometers is shown in lighter colors.
 (b) Integrated timing jitter calculated from the PSD shown in (a). Temperature-related long-term drift is notable below ~ 0.4 mHz.

The power spectral density (PSD) of the timing drift signal of the upper-layer (IL)- and lower-layer (OOL) interferometer as well as their corresponding integrated jitter (square-root of the integrated PSD, starting at high frequencies and integrated towards zero) are shown in Figure 4.18. In order to determine long-term stability, both the upper (IL) and lower layer (OOL) stability were measured for two hours at a fixed optical delay position with and without active PID control. The analog PID controller was not bandwidth limited within the depicted frequency range. In Fig. 4.18, upper layer (IL) measurements are shown in red, lower layer (OOL) in blue, and free-running (PID control disabled) in green. It is evident from Fig. 4.18 (a) that the active stabilization notably reduces the timing drift in the lower-layer (OOL) interferometer over the entire frequency range below ~ 15 Hz. On the other hand, the active PID control introduces some noise on its own at higher frequencies due to a mechanical resonance of the piezoelectric stage around 30 Hz as well as electronic noise, which increases the overall lower-layer (OOL) timing jitter by about 3 as above 30 Hz (Fig. 4.18 (b)). Note that the upper layer (IL) measurement had a lower signal-to-noise ratio compared to the lower-layer (OOL) signal due to a different amount of optical power on the respective photodiodes, effecting a higher noise floor and thus a higher apparent timing jitter in the upper layer (IL) measurement due to electronic noise. However, only the lower layer (OOL) measurement provides the relevant stability assessment and upper limit for timing drift in pump-probe experiments, since it uses the DUV/XUV beam path. It is also worth emphasizing that the free-running measurement (PID control disabled) exhibits excellent passive stability across the entire frequency range due to careful vibrational decoupling of the delay chamber from the environment, maintaining a sub-20 nm RMS timing jitter down to ~ 0.4 mHz (~ 40 min). This is why active PID control only slightly improves the drift and jitter within this frequency range. The PID controller feedback loop operates close to its sensitivity limit as evidenced by its low-frequency behavior (< 1 Hz) where the residual in-loop timing error exhibits a similar behavior as the natural (free-running) drift PSD (though it has only a negligible contribution to the integrated jitter). Temperature fluctuations in the laboratory

on longer time scales lead to a total peak-to-peak timing drift of about 310 as over the 2-h measurement time without active PID control (see inset in Fig 4.19 (b)). In contrast, the active stabilization reduces this long-term drift significantly to \sim 80 as peak-to-peak. This residual lower-layer (OOL) drift, despite of active PID control, is due to the differential mechanical drift of the two interferometer layers with temperature. A more rigid mount construction, e.g., a twin mirror mount from a single piece of metal, as well as better temperature control in the laboratory and in particular within the delay chamber, could readily improve this temperature-related drift. In addition, an electronic low-pass filter at the output of the PID controller can be used to ensure the excellent passive performance above \sim 15 Hz while reducing the timing drift at lower frequencies. This measurement demonstrates that the passive stability of our DLI is already sufficient to perform short-time (less than 40 minutes) measurements with sub-20 as RMS accuracy without using the PID controller. Active stabilization enables longer measurements over hours and potentially improves short-term stability by filtering out electronic high-frequency noise.

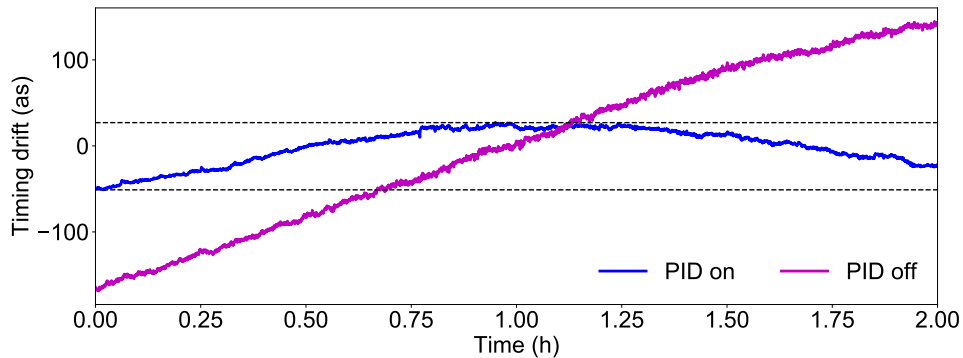


Figure 4.19: Time-domain measurement of the drift, which is significantly reduced by the active stabilization on longer time scales.

The main purpose of the DLI is to provide a phase-locked continuous delay scan

while maintaining attosecond timing precision. Figure 4.20 demonstrates a phase-locked continuous scan over the full optical delay range of 200 fs. The optical delay was scanned in \sim 80-as steps by rotating the polarizer while maintaining active stabilization. At each delay position, the lower-layer (OOL) interference signal was sampled at a \sim 83 kHz rate for 2 s. The averaged lower-layer (OOL) signal is shown in Fig. 4.20 (a) with the interference fringes normalized to the $[-1, 1]$ interval after fitting a sine function to the data in order to extract the average amplitude. The fit also yields a wavelength of 634.8 nm, which is within 0.3% of the actual 632.8 nm He-Ne wavelength. After normalizing the sampled lower-layer (OOL) signal, the signal spread at each delay step can be easily converted into optical delay jitter by applying the inverse sine function and calculating the standard deviation, which is depicted in Fig. 4.20 (b). Data points within 10% of the extrema have been removed, since the normalized signal may exceed the $[-1, 1]$ interval there due to noise and the inverse sine function would be undefined for these points, skewing the overall jitter statistics. We obtain an average timing jitter of 12.9 ± 0.8 as RMS over the entire delay range, which quantifies short-term timing jitter within a frequency range of 0.5 Hz (2 s) to the Nyquist frequency of \sim 41.5 kHz. Note that this result is better than the lower-layer (OOL) timing jitter shown in Fig. 4.18 because it was measured on a different day with a slightly different alignment of the DLI and different signal strength on the photodiodes. This suggests that electronic noise contributes significantly to the apparent timing jitter at high frequencies. Long-term drift as well as phase nonlinearity due to imperfect alignment of the polarization optics manifest as a deviation of the measured interference pattern from an ideal sine curve, which amounts to about 2.4% RMS in this measurement. Overall, this result not only shows the phase-locked delay scanning capability of our DLI but also provides sufficiently low timing jitter during the delay scan to perform highly accurate attosecond pump-probe experiments with ultrashort DUV and XUV pulses.



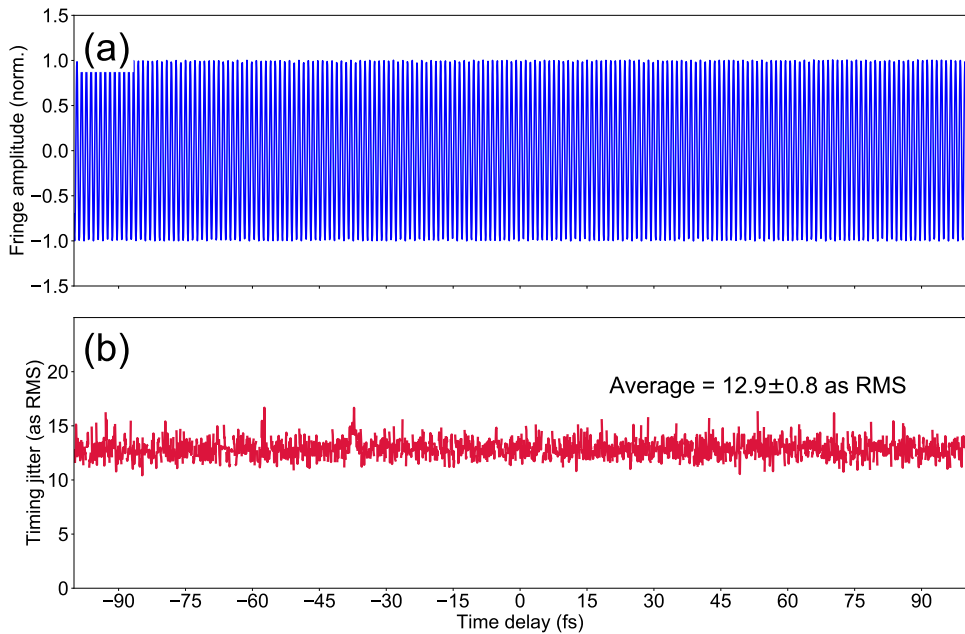
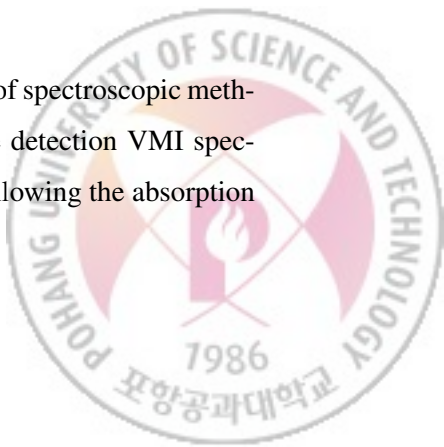


Figure 4.20: Phase-locked delay scan and stability of the double-layer interferometer over an optical delay range of 200 fs. (a) Normalized fringe amplitude in the lower-layer interferometer as a function of optical delay. (b) Timing jitter calculated from the fluctuations in the recorded interference signal within 2 s of measurement time for each delay step, yielding an average of 12.9 as RMS. Data points within 10% of the interference extrema have been removed due to unreliable conversion between amplitude and timing.

4.6 VMI spectrometer

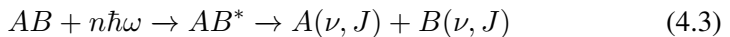
4.6.1 Introduction

To extract information from an atom or molecule, a variety of spectroscopic methods have been developed. One of them is the charged particle detection VMI spectrometer, which measures particle energy in space and time. Following the absorption

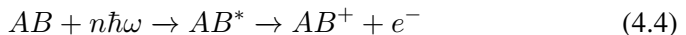


of a number of photons, molecules go through various photofragmentation processes, yielding various observables to be measured.

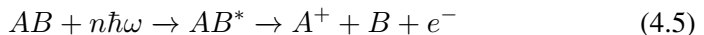
- Photodissociation



- Photoionization

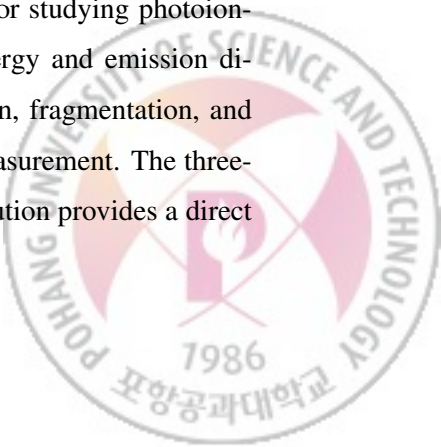


- Dissociative photoionization



where AB^* is photo-excited complex and ν and J are vibrational and rotational quantum numbers of the molecular fragments.

Chandler and Housten created a novel spectroscopic technique [55] in which the spatial distribution of photofragments (photoion (A^+ , AB^+) or photoelectron (e^-)) is projected onto a two-dimensional (2D) detector. This allows us to measure the arrival time of photofragments based on their mass-to-charge ratio. This technique was later improved by Eppink and Parker [56] by including an electrostatic lens. The electrostatic lens system is made up of a repeller, an extractor, and a ground electrode. The target atoms and molecules interact with the laser field at the position located between two electrostatic electrodes known as the repeller and extractor. When the appropriate voltages are applied to these electrodes, charged particles with the same initial velocity in the interaction region are pushed toward and focused onto the same point on the position-sensitive detector. As a result, measuring the spatial distributions of photoelectrons or photoions has become a popular technique for studying photoionization and photodetachment. This is because the kinetic energy and emission direction (spatial information) of products produced by ionization, fragmentation, and other processes are both recorded and accessible in a single measurement. The three-dimensional (3D) photoelectron or photoion momentum distribution provides a direct



way to obtain valuable information about the target structure and underlying molecular reaction. Depending on the polarity of the applied voltage to the electrodes, measured signal will be detected as photoelectron or photoion momentum distributions. In this manner, the imaging technique can be used to study laser-matter interaction.

4.6.2 VMI spectrometer design

We developed a multielectrode VMI spectrometer for detecting high-energy charged particles in the chemical physics beamline. The VMI spectrometer is made up of eleven electrodes in total. Figure 4.21 shows a schematic drawing of the VMI spectrometer. Between the repeller and the extractor electrodes, light-matter interaction occurs. Through the indicated holes in the μ -metal shielding, the laser and molecular beam enters the spectrometer. The repeller electrode is a metal disk with a 80 mm diameter and a small pinhole (50 μm diameter) orifice in the center through which a target gas flows into the interaction region. The next ten electrodes are ring-shaped, with an outer diameter of 80 mm and an inner diameter that increases in 2 mm increments, beginning with 40 mm for the extractor. These ten electrodes are stacked along the TOF axis, separated by polyether ether ketone spacers of 6 mm. SIMION simulation is used to optimize the voltage configuration at the electrodes as well as the position of the interaction region with respect to the repeller electrode in order to obtain high-resolution VMI images. Light-matter interaction at the interaction point generates charged particles, and the resulting Newton sphere (3D) expands and focuses on the detector plane (2D) using inhomogeneous electric fields created by the electrodes. A double stack, 80 mm diameter microchannel plate (MCP) assembly with a P46 ITO phosphor screen (Hamamatsu, F2226-24P) is used for charged particle imaging. When the signal strikes the front plate of the MCP, it is amplified across the MCP stack and falls onto the phosphor screen. The double stage MCP system allows the signal gain up to $\sim 10^7$ at a maximum operation voltage of ± 2400 V. The MCP rear plate is maintained on ground and the phosphor screen is operated at 3.5 kV. The

maximum voltages that can be applied to the electrodes are $V_{\text{rep}} = 15$ kV and $V_{\text{ext}} = \sim 12$ kV. Electrons with kinetic energies as high as 100 eV can be measured using this VMI spectrometer [57]. To shield the stray magnetic field from the environment, the entire VMI spectrometer is covered by a μ -metal shielding.

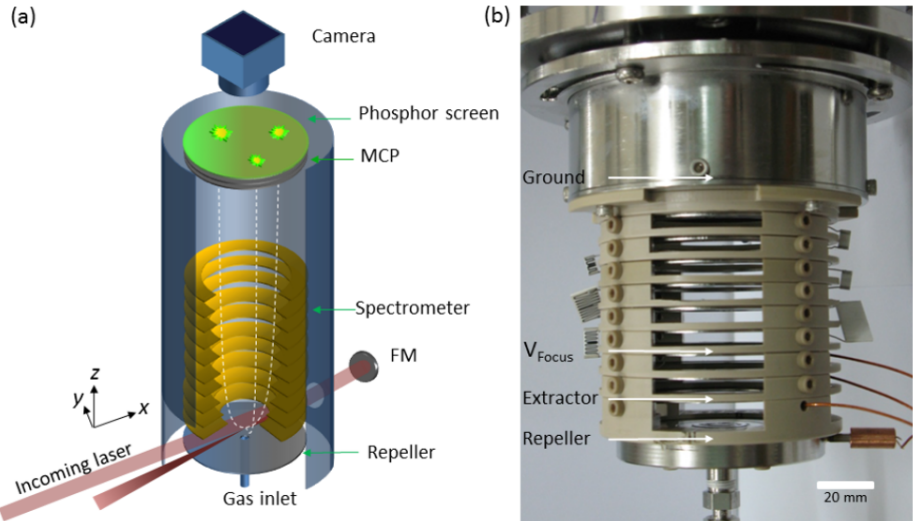


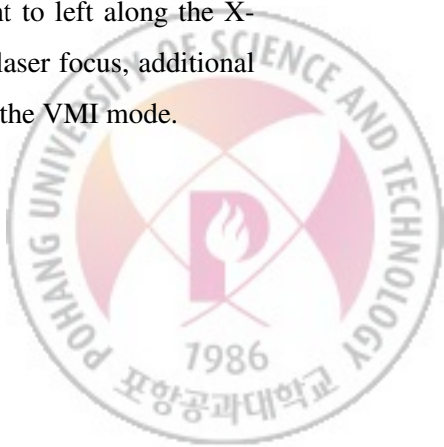
Figure 4.21: Conceptual and actual VMI setup is depicted. (a) Conceptual VMI design. (b) Actual VMI setup developed and used in the chemical physics beamline. Adapted from Ref. [57]

The visible image on the phosphor screen is captured by a charge couple device (CCD) camera placed outside the vacuum chamber through a glass window. To record the VMI images on the phosphor screen, a peltier-cooled CCD camera (PCO Sensicam qe) were mounted on the side of the experimental chamber and imaged using an objective lens through a view port on the lid. The P46 phosphor of the MCP was chosen for its short fluorescence lifetime of ~ 0.4 μ s which is much faster than for the ~ 330 μ s gap between laser pulses. Recording images at a rate of 3 kHz requires a greater data storage rate than the one-dimensional ion time-of-flight (i-TOF) spectra. For example

1024×1024 pixel images would mean that incoming light from the phosphor screen will be integrated on the CCD sensor and read out as 12-bit data and sent to the PC via PCI-Bus interface.

4.6.3 VMI spectrometer operation mode and alignment

Prior to conducting any experiments with the VMI spectrometer, the primary step is to align the instrument with respect to the laser focus. Otherwise, VMI images could become asymmetrical and meaningless. We use the *spatial imaging mode* for VMI alignment to ensure the focus of the NIR-DUV-XUV beam is centered on the VMI spectrometer's central axis. In this mode, we can determine the position of the NIR by inducing multiphoton ionization with the laser itself. Because photoelectrons produced by the multiphoton ionization are highly intensity-dependent, meaning that when the VMI is operated in this spatial mode, it magnifies the image of the laser focus along the laser propagation direction. To accomplish this, we introduced a noble gas into the interaction chamber via an effusive nozzle and intersected it with the focused NIR laser. The photoelectrons generated as a result of multiphoton ionization were captured using a CCD camera. The resulting test image is shown in Fig. 4.22 (a). To find the optimal position of the VMI in relation to the laser focus, i.e., the laser focus is at the center pixel of a test VMI image, the tilt stage of the VMI was adjusted and iterated several times until the laser focus is at the center pixel of the test VMI image. In Fig. 4.22 (a), the spatial imaging mode is shown. The laser focus position is magnified using the ATI electrons of Xe atoms and aligned with respect to the VMI's center pixel. Only the repeller voltage was applied and operated at 2 kV in this spatial imaging mode. Other electrodes were turned off. The laser polarization was along the Y-axis while the laser propagation direction was from right to left along the X-axis. After aligning the VMI spectrometer with respect to the laser focus, additional electrodes can be turned on and the spectrometer is switched to the VMI mode.



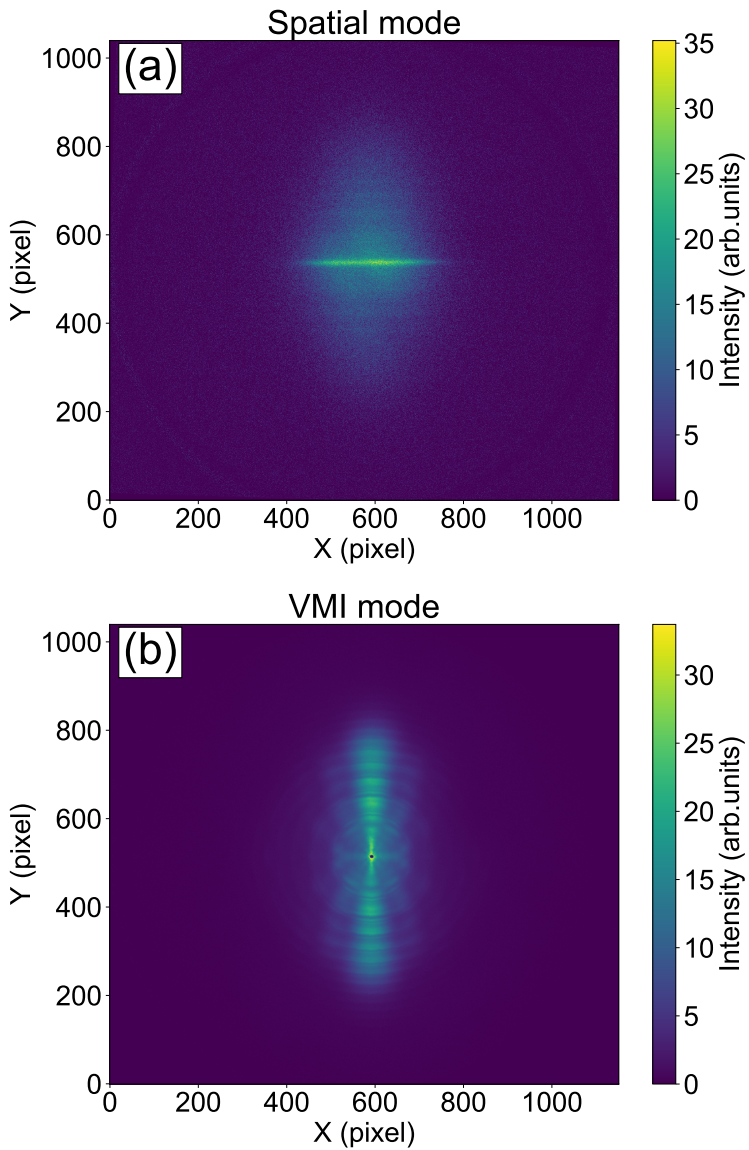


Figure 4.22: Imaging in spatial and VMI modes. ATI photoelectrons from xenon gas imaged in (a) spatial mode. (b) PEMD from molecular oxygen is recorded (raw data) in VMI mode when photoionized with a few-cycle NIR laser field. ATI peaks along the laser polarization axis such as those in (b) are useful for VMI energy calibration.

In Fig. 4.22 (b) shows an example of the PEMD from molecular oxygen upon few-cycle laser irradiation using the VMI mode. This mode enables the full 3D information of the momentum distribution to be extracted by using the inverse Abel transform.

4.6.4 VMI-TOF operation mode and calibration

The VMI spectrometer can operate not only in VMI mode but also in TOF mode, which records the arrival time of charged particles at the detector based on their *mass-to-charge ratio* (m/q). Instead of recording an image, the amplified electric currents produced by charged particles can be measured in this mode. In order to accomplish this, a 30 cm long doubly-shielded $50\ \Omega$ coaxial cable with SMA type connectors are used to connect the phosphor output terminal on the back of the MCP mounting flange to a 14 bit, 2 GSamples/s analogue-to-digital converter (ADQ14DC-2X, SP Devices) through a high-speed, variable-gain current amplifier (DHPCA-100, Femto Messtechnik GmbH). This ADC model has a PCI express interface and a data transfer rate of up to 3200 MB per second onto the host PC. Assuming a record length of 10 μ s for each TOF trace and a memory overhead per sample of 2 Bytes, the data generated per shot is 64 kB, resulting in 192 MB generated per second at 3 kHz, which is significantly less than the maximum transfer rate. Due to the TOF signal's low signal-to-noise ratio (SNR), the ADQ14 digitizer is configured in multi-record mode, which allows multiple TOF traces to be recorded at the trigger rate and averaged to reduce statistical noise in the trace (see Fig. 4.23). The ADQ14 digitizer has a resolution of 14 bits. However, the laser intensity noise and noise from the current amplifier can reduce the actual number of bits, i.e., the dynamic range of the digitizer. As a result, the effective number of bits (ENOB), which is the true bit depth after accounting for the noise floor of the analogue-to-digital converter, is used to evaluate the dynamic range of the data acquisition system. The ADQ14 has an ENOB of 9.5.

The RMS noise voltage V_{RMS} is determined by the following formula:

$$V_{\text{RMS}} = \frac{V_{\text{pp}}}{2^{\text{ENOB}}} \quad (4.6)$$

where V_{pp} is the peak-to-peak input voltage amplitude. With ADQ14 safety in mind, we limited the ADC input voltage range to about 500 mV (1 V full range) after the current amplification, implying a noise floor of ~ 0.7 mV. The actual TOF signals are measured in tens of mV ($\sim 10\text{-}50$ mV, depending on amplification gain, laser intensity, etc.) hence the averaged pulse amplitude after considering the aforementioned factors yields a SNR of $\sim 14\text{-}17$, which is more than sufficient.

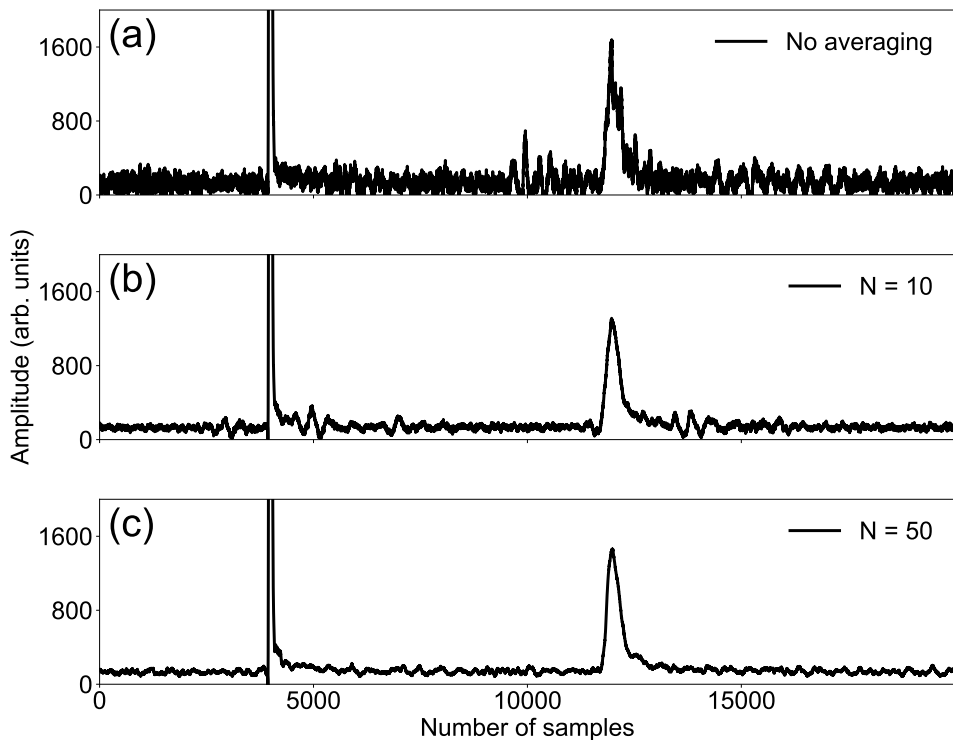


Figure 4.23: Examples of waveform averaging with different numbers of averaging using multi-record feature in the ADQ14 digitizer. (a) No averaging applied, raw data. (b) 10-waveforms averaged. (c) 50-waveforms averaged.

VMI-TOF spectrometer calibration

The VMI-TOF spectrometer must also be calibrated in order to be element-specific (m/q). Similarly to the VMI experiment, a gas sample was injected via an effusive gas jet embedded in the VMI spectrometer's repeller electrode. The generated electrons and ions are accelerated to the MCP detector by an inhomogeneous DC electric field. Electrode voltages were set to either negative or positive polarity depending on the signal of interest. Because we were not interested in the momentum position in the TOF mode, only the repeller was used in the experiment. Therefore, the ions are classified according to their mass-to-charge ratio (m/q). We calibrated the VMI-TOF using two different noble gases, krypton ($m/q = 84$) and xenon ($m/q = 132$). Due to their relatively high and distinct mass-to-charge ratio, they produce a distinct and easily identifiable TOF signal. As a result, we were able to calculate the calibration coefficient by measuring the corresponding arrival time (TOF). The TOF equation following the Wiley-McLaren design is given by:

$$t = k \cdot \sqrt{\frac{1}{V_R} \cdot \frac{m}{q}} \quad (4.7)$$

Here: V_R -is the repeller voltage, k -denotes the calibration coefficient that must be determined for a given repeller voltage. In our case, calibration coefficient was found to be $k = 0.7850 [\mu\text{s}/(\text{amu}/\text{kV})^{0.5}]$.



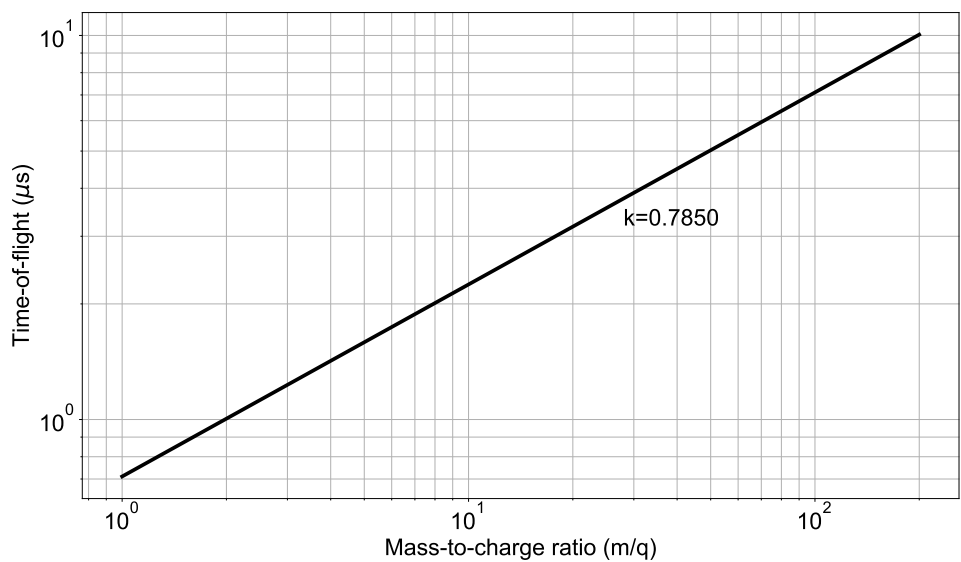


Figure 4.24: TOF and mass-to-charge ratio relation calculated from the experimental result. The calibration coefficient (k) was found to be 0.7850.

After the VMI-TOF spectrometer was calibrated, the mass spectrum of molecular nitrogen ion signals ($\text{N}^{2+}, \text{N}^+, \text{N}_2^+$) were measured along with other residual gas ion signals in the interaction chamber as shown in Fig. 4.25. Mostly, $m/q = 14$ and 28 are most dominant signals in the mass spectrum and validate our spectrometer calibration.



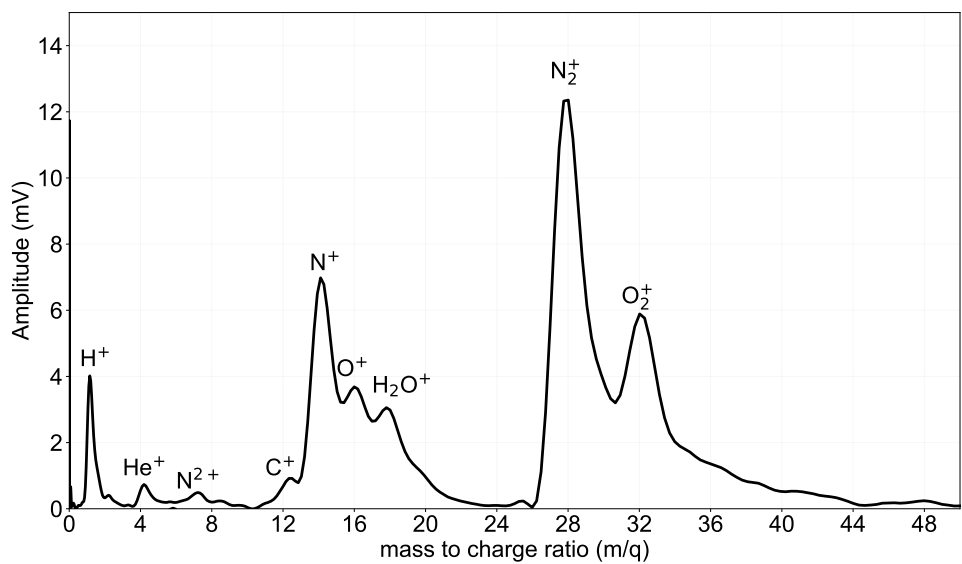


Figure 4.25: Mass spectrum of molecular nitrogen (N_2). Molecular ion signals N_2^+ , N^+ , N_2^+ are identified along with other residual gas ion signals in the interaction chamber.



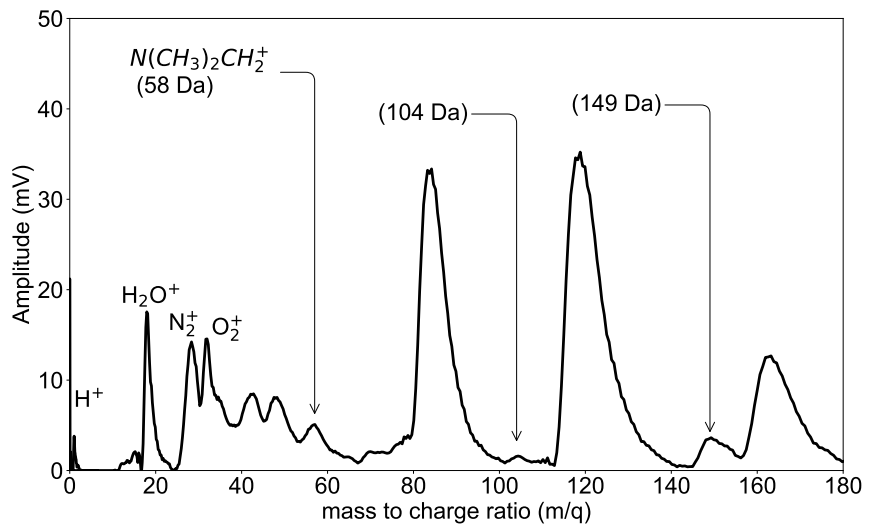


Figure 4.26: Measured mass spectrum from the PENNA molecule when irradiated with a few-cycle NIR laser.

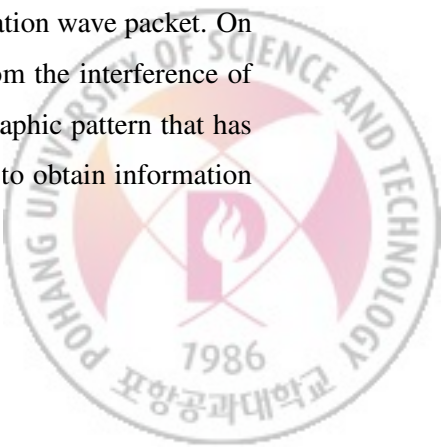


V. The beamline applications for photoelectron holography experiments

5.1 Motivation

When an atom is exposed to a strong laser field, a fraction of electrons can be liberated through the tunnel ionization and propagate in the driving laser field. A portion of these electrons can return and recombine with the parent ion. This allows for the generation of high-order harmonics. On the other hand, some tunnelling electrons fly away on their own (direct electron wavepacket), while others can return and scatter off the parent ion (rescattering electron wavepacket). In the latter case, scattered electrons can accumulate an additional phase on their path to the detector, interfering with some direct electrons when their final momentum is the same. This way, two electron wavepackets can create an interference pattern at the detector similarly with the conventional optical interferometer, which is referred to as *photoelectron holography* (PH).

PH has gained considerable attention in the last decade due to its ability to encode the structure of an atom with sub-angstrom resolution and on a subcycle time scale. Depending on the origin and scattering behavior of the photoelectrons, different interference patterns can be distinguished in PH. For the first time, a spider-like PH pattern was identified [58], and this type of PH pattern has since been extensively studied both theoretically and experimentally [59]. This structure is formed by the interference of the forward scattering electron wave packet and the direct ionization wave packet. On the other hand, a fishbone-like structure [60], which results from the interference of direct and backscattered trajectories, is a less prominent holographic pattern that has been observed experimentally using NIR laser pulses and used to obtain information



on nuclear dynamics [61]. In the past, the majority of photoelectron holography experiments have been performed with multicycle lasers. In a multicycle laser field, electron wave packets are repeatedly emitted from their parent ion with every half optical cycle, resulting in intracycle and intercycle interferences [62] and causing one type of interference pattern to obstruct or entangle another type of interference pattern in the photoelectron momentum distributions. Thus, a few-cycle laser pulse is preferable for investigating the scattering process because it eliminates intercycle interference and leaves only intracycle interference patterns dominant in the *photoelectron momentum distribution* (PEMD). Numerous theoretical studies have been conducted in recent years on the few-cycle laser driven PH feature [63]. Recently, it was theoretically shown that CEP control of a few-cycle laser significantly alters the interference patterns in a PEMD and that CEP-stabilized few-cycle laser pulses can be used to distinguish between different types of intracycle interference [64, 65]. When the driving few-cycle laser has a sine electric field, a fishbone-like structure is produced, whereas the cosine electric field produces a spider-like structure in the PEMD, implying that these interference patterns closely related to the rescattering mechanism. Controlling the rescattering electron trajectories with the CEP has primarily been discussed theoretically [66], but has not yet been demonstrated experimentally.

5.2 PH experiments with a multicycle laser

Intra- and intercycle interferences are possible in the multicycle laser field. As a result, the PEMD driven by multicycle lasers exhibits multiple types of interference patterns that interfere with one another. Figure 5.1 (a) shows the measured PEMD of N₂ using 30-fs a NIR laser field. Molecular nitrogen was randomly oriented in this experiment. PEMD was symmetric in both the up and down directions, as demonstrated by the experimental results. As previously stated, electron wave packets emitted from every half-optical cycles obstruct with each other, therefore resulting in the symmetric PEMD.

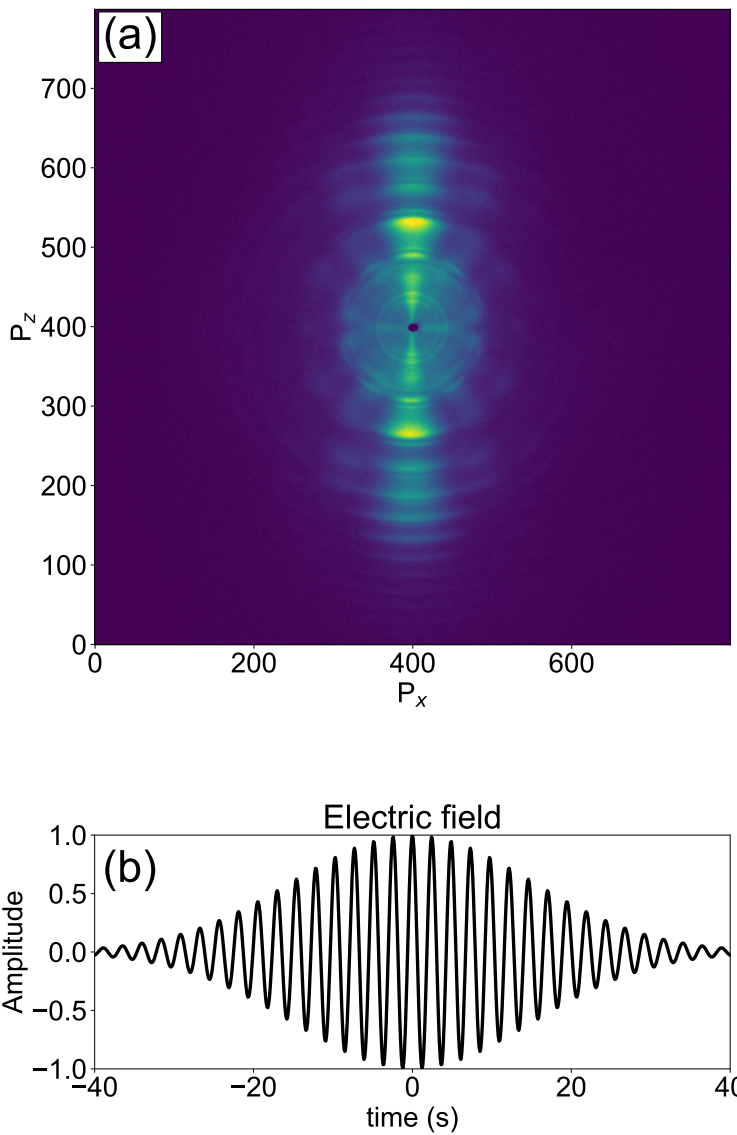


Figure 5.1: N₂ PEMD with a multicycle laser pulse. (a) Measured PEMD with a 30-fs NIR laser field. (b) Simulated driving laser electric field

To ensure the molecular orientation effect with respect to the laser polarization, we simulated the PEMD of parallel aligned and alignment averaged molecules in a linearly polarized laser field with an intensity of $1.5 \times 10^{14} \text{ W/cm}^2$ and a wavelength of 800 nm using the TDSE method. The laser parameters are identical to those used in the experiment. Figure 5.2 (a) and (b) illustrate the simulated PEMD in the presence of a multicycle laser field when the molecular nitrogen is alignment averaged and parallel aligned respectively. According to the simulation result, molecular orientation is not significant for the PEMD. Alignment averaged TDSE simulations well reproduce the experimental PEMD result (see Fig. 5.1), and as expected, multiple types of interference patterns obstruct each other.

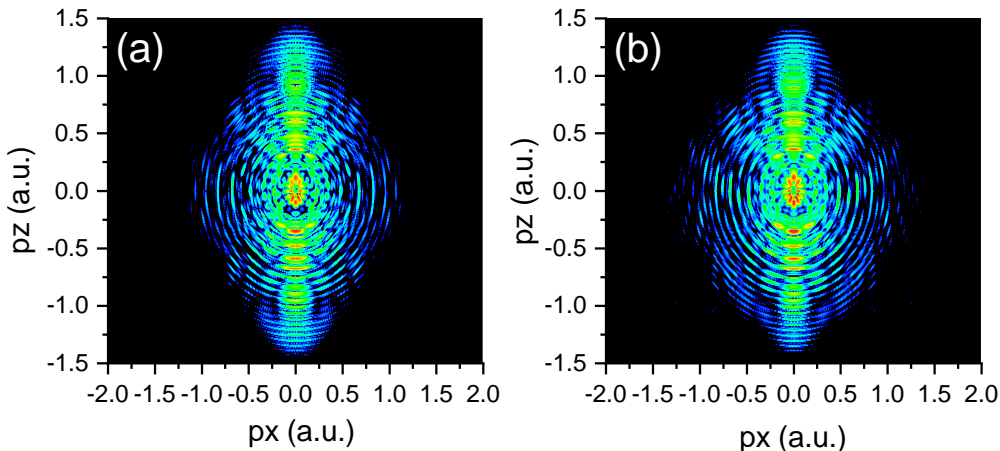
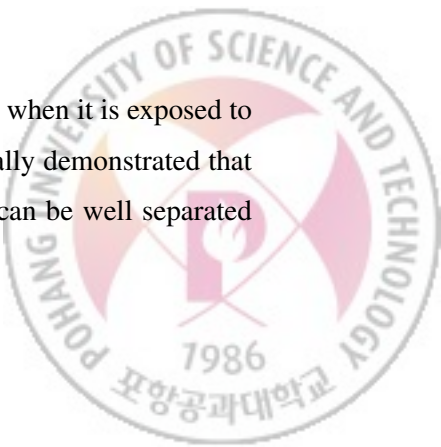


Figure 5.2: TDSE simulation of N_2 PEMD with a multicycle laser pulse. (a) Parallel aligned. (b) Alignment averaged.

5.3 PH experiments with a few-cycle laser

In this experiment, we studied PH from molecular nitrogen when it is exposed to 1.2-cycle NIR laser pulses with different CEPs and experimentally demonstrated that well-known spider-like and fishbone-like interference patterns can be well separated



by using a CEP-stabilized 1.2-cycle NIR laser field. Figs. 5.3-5.5 show experimentally the measured PEMDs when the few-cycle driving NIR laser CEP is changed.



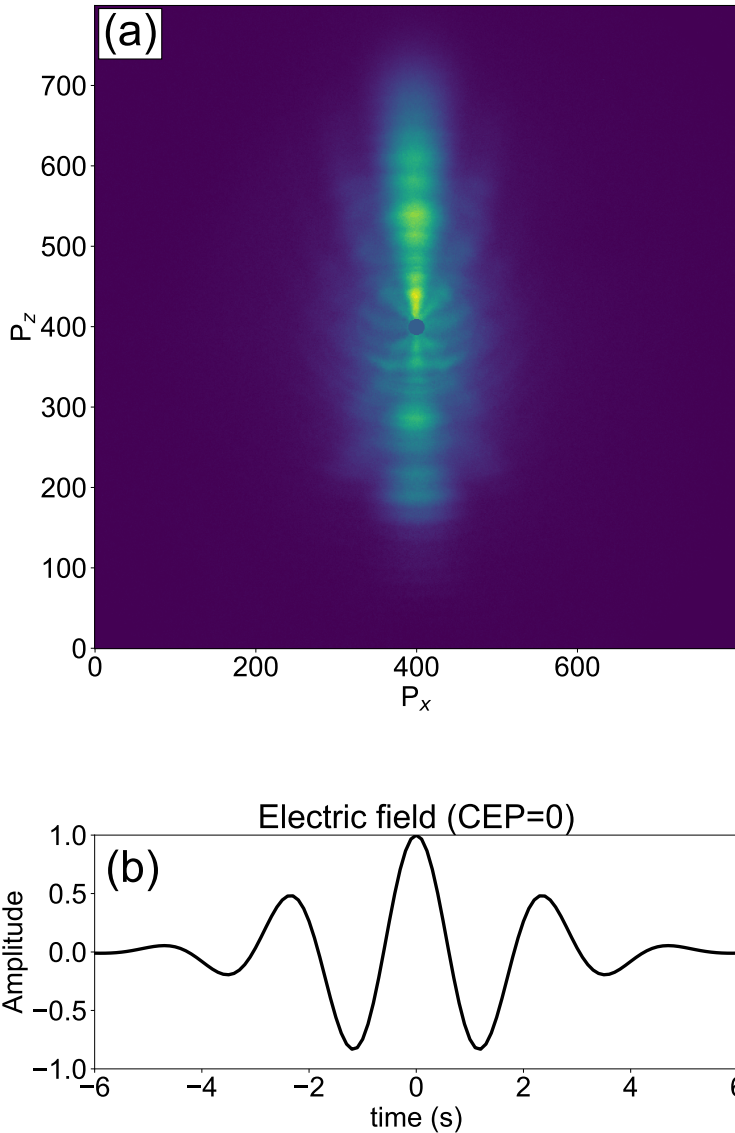


Figure 5.3: N₂ PEMD with a few-cycle laser pulse. (a) Measured PEMD with a 3.4-fs NIR laser field. (b) Simulated driving laser electric field, CEP = 0

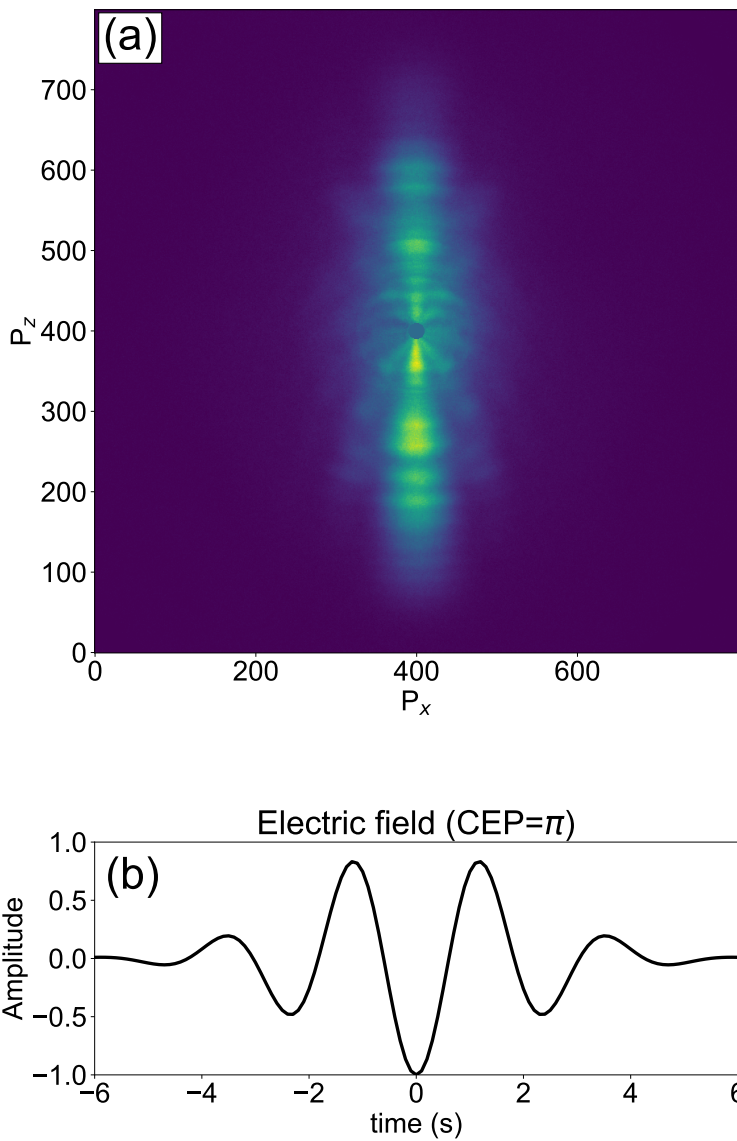


Figure 5.4: N_2 PEMD with a few-cycle laser pulse. (a) Measured PEMD with a 3.4-fs NIR laser field. (b) Simulated driving laser electric field, $CEP = \pi$

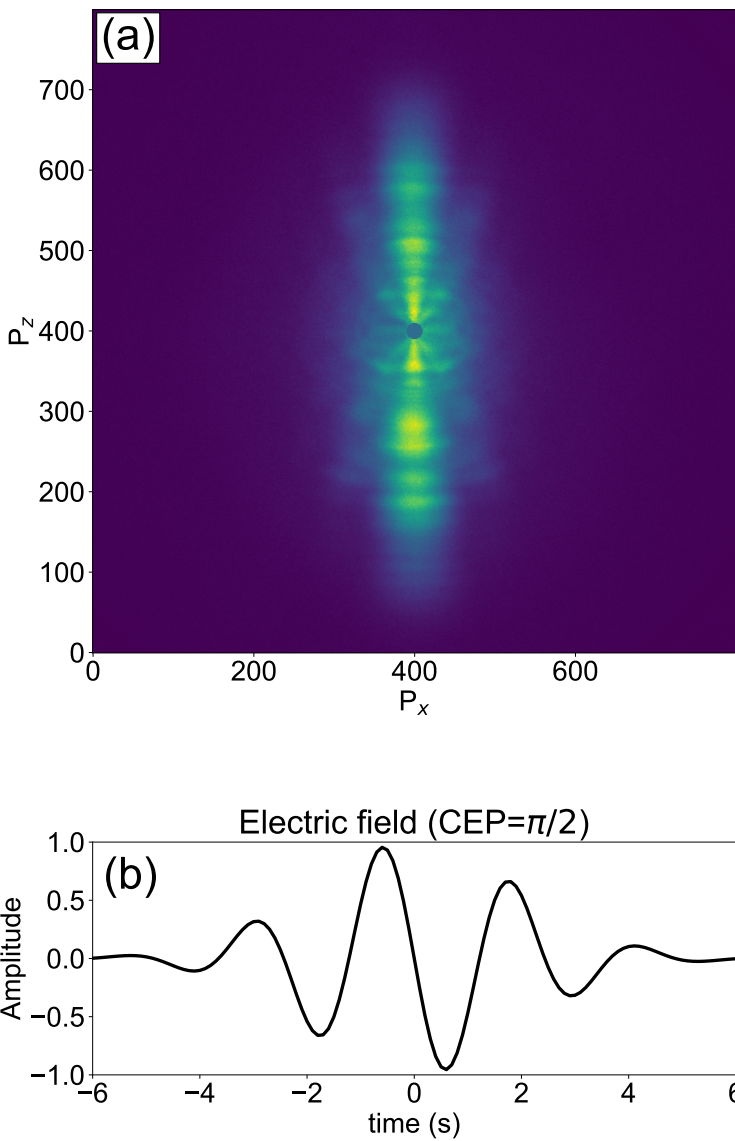


Figure 5.5: N₂ PEMD with a few-cycle laser pulse. (a) Measured PEMD with a 3.4-fs NIR laser field. (b) Simulated driving laser electric field, CEP = $\pi/2$

Our experimental results show that the interference pattern in the PEMD is highly correlated with the shape of the electric field, which is obviously controlled by the CEP of the ultrashort pulse. For a cosine-shaped electric field, an asymmetric PEMD pattern has been observed for the first time. A spider-like PEMD structure appears in the upward direction, whereas a fishbone-like (or boomerang type) PEMD structure appears in the downward direction (see Fig. 5.3). However, for a sine-shaped electric field, a spider-like pattern appears in both upward and downward directions, symmetrically (see Fig. 5.5). Then we demonstrate that by controlling the CEP, the spider-like structure can be altered as shown in Fig. 5.4. The TDSE simulation reproduces the experimental observations accurately and captures the major features as illustrated in Fig 5.6.

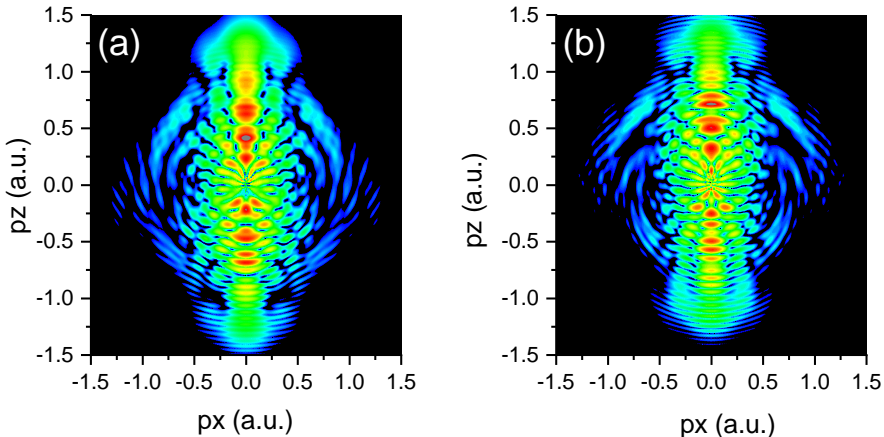


Figure 5.6: TDSE simulation of N_2 PEMD with a few-cycle laser pulse. (a) $CEP = 0$. (b) $CEP = \pi/2$.

To ascertain the reason for the PEMD's symmetry breaking when a few-cycle laser is used, we carried out an SFA simulations by considering contributions from various electron orbits. Intracycle interference occurs when the direct and indirect orbits interfere at the detector. Typically, the amplitudes of the two orbits coincide in a

linearly polarized laser field, allowing for clear intracycle interference to be observed in the PEMD spectrum. When only direct orbits are taken into account in the SFA simulation, the result indicates a symmetric PEMD (Fig. 5.7, 5.8 (b)). When rescattering orbits are taken into account, the result indicates an asymmetric PEMD (Fig. 5.7, 5.8 (a)). As a result, we conclude that when a few-cycle laser is used, forward-rescattering orbits are critical for the formation of asymmetric PEMD. Whereas the contribution of backward-rescattering orbits is negligible. When a sine-shaped electric field is applied, forward-rescattering electron orbits contribute symmetrically to the PEMD, resulting in a symmetric PEMD distribution as illustrated in Fig. 5.5. Fig 5.9 depicts the temporal variation of a few-cycle laser field and the associated electron trajectories which contribute to a PEMD structure.

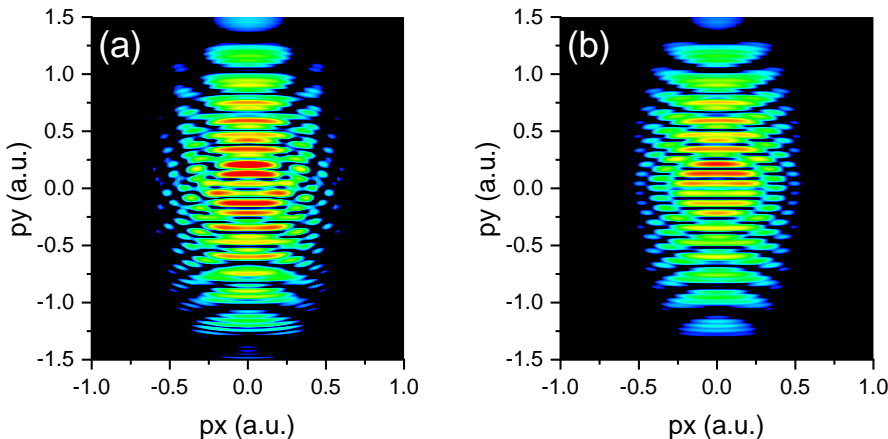


Figure 5.7: SFA simulation of N_2 PEMD with a few-cycle laser pulse CEP = 0. (a) Direct and rescattering orbits. (b) Direct orbits only.



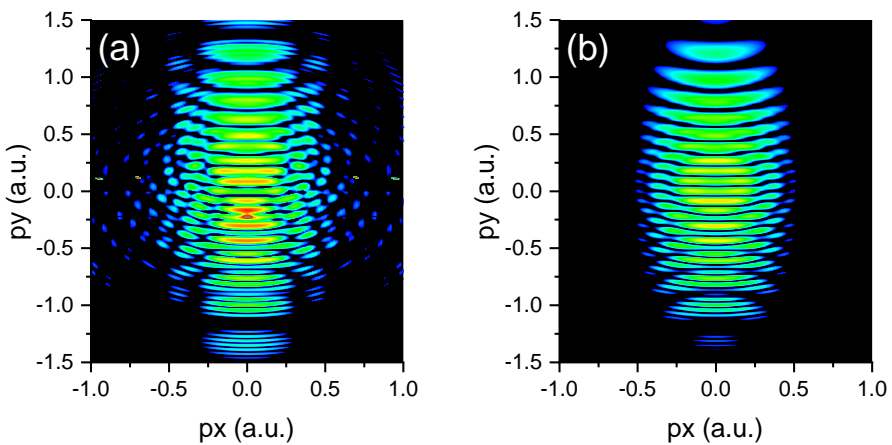


Figure 5.8: SFA simulation of N_2 PEMD with a few-cycle laser pulse $\text{CEP} = \pi/2$. (a) Direct and rescattering orbits. (b) Direct orbits only.



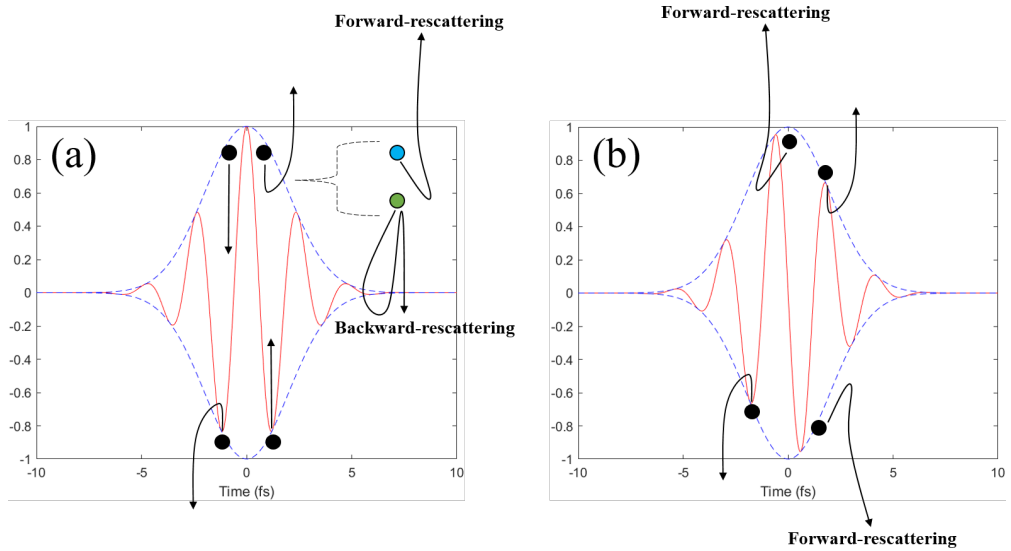


Figure 5.9: Relevant electron trajectories are shown when the (a) $\text{CEP} = 0$, (b) $\text{CEP} = \pi/2$. Forward-rescattering electron trajectories resulting in a asymmetric PEMD. Contributions from back-rescattering electron trajectories are negligible.

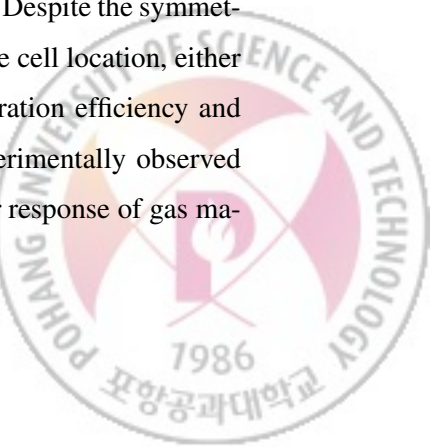
Experimental observation is well reproduced and explained by theoretical simulations (TDSE and SFA). Our theoretical simulations reveal that the forward scattering of electron trajectories plays a key role and affects the interference structures in the PEMD.

In our experiment, the contribution from intercycle interference was greatly suppressed by using a CEP-stabilized few-cycle laser, resulting in well separated spider- and fishbone-like interference patterns in the PEMD. To the best of our knowledge, this is the first demonstration of spider and fishbone structure separation using a few-cycle NIR laser.

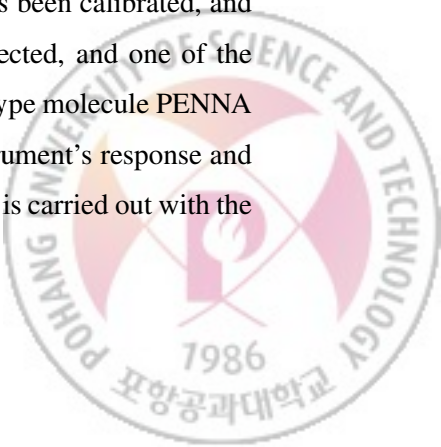


VI. Conclusions and outlook

The author worked on developing a state-of-the-art attosecond chemical physics beamline at POSTECH with the mind of studying the dynamics of ultrafast chemical reactions, particularly in biologically relevant molecules, as motivated by the experimental work of L. Lehr [67] and theoretical work of S. Lünenmann et al [68]. As a prerequisite, in Chapter III, the author discussed the generation of CEP-stabilized ultrashort laser sources in the visible/NIR spectral range and compressing them down to 1.2-cycles by compensating for higher order dispersion terms, thereby achieving close to Fourier-transform-limited pulses. The resulting few-cycle laser was measured with a novel dispersion scan method. Afterward, the development of the beamline utilizing the generated few-cycle NIR laser source is discussed in detail in Chapter IV. Beginning with the design of the beamline in Chapter IV, the efficient deep UV generation method was thoroughly investigated. We found that UV production via third-order processes is critically dependent on the gas cell's position relative to the laser focus and on a number of previously unexplored highly nonlinear effects. We also experimentally demonstrated that we could achieve 1 μJ -class DUV pulses in the 3.6-5.7 eV range (at a -20 dB intensity level), which supports a transform-limited sub-2.5-fs pulse, using Ar gas at sub-atmospheric pressure (0.8 bar). Obtaining μJ -class DUV pulse energy at sub-atmospheric pressure which is \sim 10-times lower pressure than previous works, is also a significant achievement in terms of engineering. Additionally, depending on the cell position, generated DUV spectra exhibited spectral blueshift and found to be associated with electron density buildup during THG. Despite the symmetric intensity distribution of the laser beam near the laser focus, the cell location, either before or after the laser focus, had an effect on the DUV generation efficiency and blueshift. A numerical simulation was used to explain the experimentally observed blueshift tendency. By striking a balance between the third-order response of gas ma-



terials and highly nonlinear processes, careful simultaneous optimizations of the gas type, gas pressure, laser intensity, and cell location can result in highly efficient UV generation. Additionally, by following the motivation of this thesis, efficiently generated intense few-cycle DUV pulses were combined with ultrashort NIR and XUV pulses for time-resolved experiments. To investigate ultrafast dynamics with high time resolution, the timing jitter between the pump and probe pulses should be kept to an attosecond time scale. To accomplish this, we implemented a double-layer interferometry (DLI) system in our DUV/XUV beamline that is capable of continuous delay change or scan while maintaining the relative phase between the two arms of the interferometer. A collinear scheme is used to generate few-cycle DUV and XUV pulses in a gas and the resulting DUV and XUV pulses are being separated spectrally and spatially by a perforated dichroic beam separator, forming a pump-probe experimental configuration. Before the active stabilization, additional efforts were made to suppress vibrational noise from the environment by using a number of vibration isolation methods. In addition, for the continuous scan capability, we implemented Pancharatnam's phase stabilization method in the DLI, as a result we demonstrated that the timing jitter between the pump and probe pulses can be stabilized to 12.9 ± 0.8 as RMS in short-term jitter and ~ 80 as long-term peak-to-peak drift over 2 h. Thus, the exceptional attosecond time resolution during the continuous delay scans over a period of 200 fs is allowing us to perform high time resolution experiments to investigate the ultrafast electron dynamics in chemical reactions. The design and operation of a velocity map imaging spectrometer capable of operating in two modes, VMI and TOF, is discussed at the end of Chapter IV. VMI-TOF mode is particularly useful for determining the dynamics of molecular photo-dissociation as a function of the time delay between pump and probe pulses. In this regard, the VMI-TOF spectrometer has been calibrated, and a number of TOF traces from various samples have been collected, and one of the marker ion mass-to-charge ratio has been detected from a prototype molecule PENNA under different experimental conditions, demonstrating the instrument's response and readiness. In Chapter V, a photoelectron holography experiment is carried out with the



help of a VMI spectrometer. Photoelectron holography has previously been well studied using short and mid-IR multi-cycle lasers, and more recently with NIR lasers. In our case, we investigated the photoelectron momentum distribution of randomly oriented molecular nitrogen when it interacted with CEP-stabilized 1.2-cycles NIR laser pulses, and the previously well-known spider and fishbone like PEMD are well separated, which is typically entangled when using multicycle laser. Within the scope of this thesis, an attosecond chemical physics beamline has been built, ultrashort light sources have been generated and characterized, and the required high time resolution for studying ultrafast chemical reaction dynamics has been demonstrated. Produced ultrashort laser sources are used in the photoelectron holography experiment, and the effect and significance of a few-cycle laser electric field waveform are revealed by separating well-known PEMD features as a result of subcycle control of the electron trajectory.



요약문

저자는 특히 생물학적으로 관련된 분자에서 초고속 화학 반응의 역학을 연구하는 마음으로 POSTECH에서 최첨단 아토초 화학 물리학 범라인을 개발했습니다. 생물학적으로 관련된 분자를 연구하려면 대부분의 생체 분자가 UV 영역에서 흡수 대역폭을 갖기 때문에 깊은 UV 영역에서의 초단파 레이저가 필요합니다. 따라서 효율적인 deep UV 생성 방법을 철저히 조사하였습니다. 우리는 3차 오더의 계산을 통한 UV 생산이 레이저 초점에 대한 가스 셀의 위치와 이전에 탐색되지 않은 많은 고도의 비선형 효과에 크게 의존한다는 것을 발견했습니다. 우리는 또한 실험적으로 3.6-5.7 eV 범위(-20dB 강도 레벨에서)에서 1μJ급 DUV 펄스를 달성할 수 있음을 입증했습니다. 대기압(0.8bar). 이전 작업보다 10배 낮은 압력보다 낮은 대기압에서 μJ급 DUV 펄스 에너지를 얻는 것도 엔지니어링 측면에서 중요한 성과입니다. 또한, 셀 위치에 따라 생성된 DUV 스펙트럼은 스펙트럼 청색 편이를 나타내며 THG 동안 전자 밀도 축적과 관련이 있는 것으로 밝혀졌습니다. 레이저 초점 근처의 레이저 빔의 대칭적인 강도 분포에도 불구하고 레이저 초점 전후의 셀 위치는 DUV 생성 효율과 청색 편이에 영향을 미쳤습니다. 수치 시뮬레이션은 실험적으로 관찰된 청색 편이 경향을 설명하는 데 사용되었습니다. 가스 재료의 3차 오더의 반응과 고도로 비선형적인 프로세스 사이의 균형을 유지함으로써 가스 유형, 가스 압력, 레이저 강도 및 셀 위치의 신중한 동시 최적화를 통해 매우 효율적인 UV 생성을 얻을 수 있습니다. 또한, 이 논문의 동기를 따라 효율적으로 생성된 강렬한 몇 사이클 DUV 펄스를 초단 NIR 및 XUV 펄스와 결합하여 시간 분해 실험을

수행했습니다. 높은 시간 분해능으로 초고속 역학을 조사하려면 펌프와 프로브 펄스 사이의 타이밍 지터를 아토초 시간 규모로 유지해야 합니다. 이를 달성하기 위해 DUV/XUV 빔라인에 DLI (Double Layer Interferometry) 시스템을 구현했습니다. 이 시스템은 간섭계의 두 암 사이의 상대 위상을 유지하면서 지속적인 자연 변경 또는 스캔이 가능합니다. 공선 방식은 가스에서 몇 사이클 DUV 및 XUV 펄스를 생성하는 데 사용되며 결과 DUV 및 XUV 펄스는 천공된 이색성 빔 분리기에 의해 스펙트럼 및 공간적으로 분리되어 펌프 프로브 실험 구성을 형성합니다. 능동 안정화 이전에 여러 방진 방법을 사용하여 환경으로부터의 진동 소음을 억제하기 위한 추가적인 노력이 있었습니다. 또한 연속 스캔 기능을 위해 DLI에서 Pancharatnam의 위상 안정화 방법을 구현하여 펌프와 프로브 펄스 사이의 타이밍 지터가 단기 지터 및 에서 RMS로 12.9 ± 0.8 로 안정화될 수 있음을 입증했고 2시간동안의 측정으로 최대 80 as 피크-피크 드리프트를 관찰하였습니다. 따라서 200fs의 극도로 짧은 반응시간동안에 아주 뛰어난 아토초 시간 분해능을 가진 실험 셋업은 화학 반응에서 초고속 전자 역학을 조사하기 위해 높은 시간 분해능 실험을 수행할 수 있게 해줍니다.

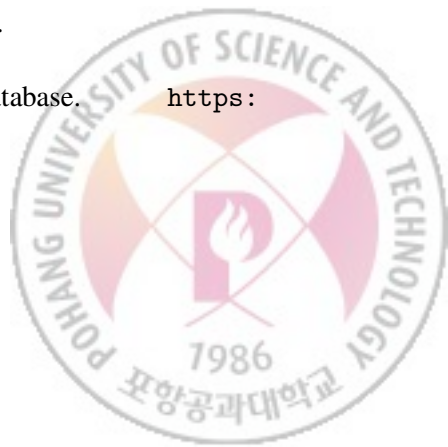
광전자 흘로그래피 실험은 VMI 분광계의 도움으로 수행됩니다. 광전자 흘로그래피는 이전에 단적외선 및 중적외선 다중 주기 레이저를 사용하여 잘 연구되었으며 최근에는 NIR 레이저를 사용하여 연구되었습니다. 우리의 경우 CEP 안정화 1.2 주기 NIR 레이저 펄스와 상호 작용할 때 무작위로 배향된 문자 질소의 광전자 운동량 분포를 조사했으며 이전에 잘 알려진 거미모양과 생선 뼈 모양의 PEMD 패턴을 잘 구분할 수 있었습니다. 이 논문에서는, 아토초 화학 물리학 빔라인을 구축하였습니다. 우리의 셋업에서는 초단파 광원이 생성 및 특성화되었으며 초고속 화학

반응 역학을 연구하는 데 필요한 높은 시간 분해능이 입증되었습니다. 생성된 초단파 레이저 소스는 광전자 홀로그래피 실험에 사용되며, 전자 궤적의 서브사이클 제어 결과 잘 알려진 PEMD 특성을 분리하여 반사이클 레이저 전계 파형의 효과와 의의를 드러냅니다.



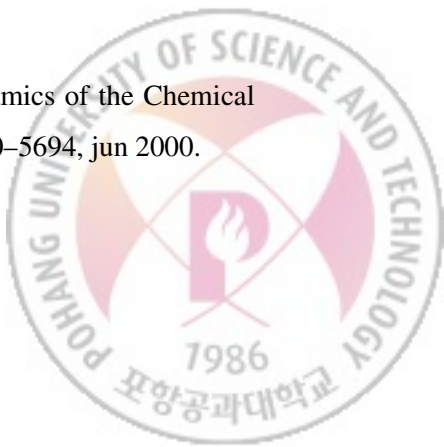
References

- [1] G. Voronov and N. Delone. Many-photon Ionization of the Xenon Atom by Ruby Laser Radiation. *Soviet Journal of Experimental and Theoretical Physics*, 23(1):54, 1966.
- [2] P. Agostini, F. Fabre, G. Mainfray, G. Petite, and N. K. Rahman. Free-free transitions following six-photon ionization of xenon atoms. *Physical Review Letters*, 42(17):1127–1130, 1979.
- [3] L. V. Keldysh. Ionization in the field of a strong electromagnetic wave. *Soviet Journal of Experimental and Theoretical Physics*, 20(5), 11 1964.
- [4] Claude Cohen-Tannoudji and David Guéry-Odelin. *Advances in Atomic Physics*. 2011.
- [5] Thomas Brabec and Ferenc Krausz. Intense few-cycle laser fields: Frontiers of nonlinear optics. *Reviews of Modern Physics*, 72(2):545–591, 2000.
- [6] K.W. DeLong, D.N. Fittinghoff, C.L. Ladera, R. Trebino, G. Taft, A. Rundquist, M.M. Murnane, H.C. Kapteyn, and I.P. Christov. *Frequency-resolved optical gating measurements of ultrashort laser pulses*. 2005.
- [7] Ronald Newbold Bracewell and Ronald N Bracewell. *The Fourier transform and its applications*, volume 31999. McGraw-Hill New York, 1986.
- [8] Zenghu Chang. *Fundamentals of attosecond optics*. 2011.
- [9] Mikhail N. Polyanskiy. Refractive index database. <https://refractiveindex.info>. Accessed on 2021-06-29.

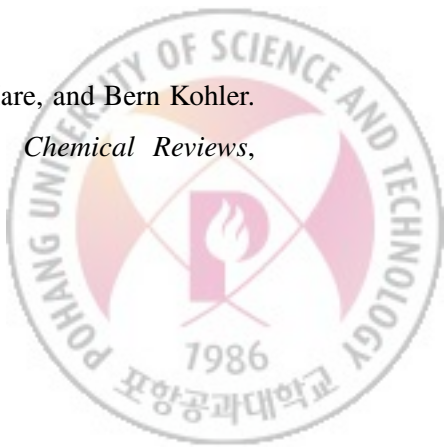


- [10] Robert Szipöcs, Christian Spielmann, Ferenc Krausz, and Kárpát Ferencz. Chirped multilayer coatings for broadband dispersion control in femtosecond lasers. *Optics Letters*, 19(3):201, feb 1994.
- [11] Fabian Lücking, Andreas Assion, Alexander Apolonski, Ferenc Krausz, and Günter Steinmeyer. Long-term carrier-envelope-phase-stable few-cycle pulses by use of the feed-forward method. *Optics Letters*, 37(11):2076, 2012.
- [12] M Piche. Beam reshaping and self-mode-locking in nonlinear laser resonators. *Optics communications*, 86:156–160, 1991.
- [13] D E Spence, P N Kean, and W Sibbett. 60-fsec pulse generation from a self-mode-locked Ti : sapphire laser. *Optical Society of America*, 16(1):42–44, 1991.
- [14] Andreas Vernaleken, Bernhard Schmidt, Theodor W. Hänsch, Ronald Holzwarth, and Peter Hommelhoff. Carrier-envelope frequency stabilization of a Ti:sapphire oscillator using different pump lasers: part II. *Applied Physics B: Lasers and Optics*, 117(1):33–39, 2014.
- [15] Donna Strickland and Gerard Mourou. Compression of amplified chirped optical pulses. *Optics Communications*, 55(6):447–449, 1985.
- [16] Fabian Lücking. Carrier-Envelope Phase Control for the Advancement of Attosecond Pulse Generation. *LMU PhD Thesis*, 2014.
- [17] M. Nissoli, S. De Silvestri, O. Svelto, R. Szipöcs, K. Ferencz, Ch. Spielmann, S. Sartania, and F. Krausz. Compression of high-energy laser pulses below 5 fs. *Optics Letters*, 22(8):522, 1997.
- [18] A. Couairon and A. Mysyrowicz. Femtosecond filamentation in transparent media. *Physics Reports*, 441(2-4):47–189, 2007.
- [19] M. Seo, K. Tsendsuren, S. Mitra, M. Kling, and D. Kim. High-contrast, intense single-cycle pulses from an all thin-solid-plate setup. *Optics Letters*, 45(2), 2020.

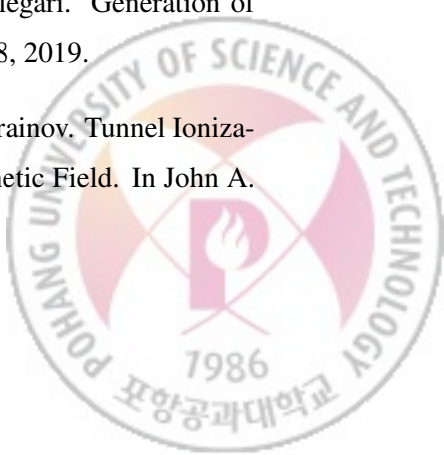
- [20] Rick Trebino, Kenneth W. DeLong, David N. Fittinghoff, John N. Sweetser, Marco A. Krumbügel, Bruce A. Richman, and Daniel J. Kane. Measuring ultra-short laser pulses in the time-frequency domain using frequency-resolved optical gating. *Review of Scientific Instruments*, 68(9):3277–3295, 1997.
- [21] C Iaconis and I A Walmsley. Spectral phase interferometry for direct electric-field reconstruction of ultrashort optical pulses. *Opt. Lett.*, 23(10):792–794, may 1998.
- [22] Francisco Silva, Miguel Miranda, Benjamín Alonso, Jens Rauschenberger, Vladimir Pervak, and Helder Crespo. Simultaneous compression, characterization and phase stabilization of GW-level 14 cycle VIS-NIR femtosecond pulses using a single dispersion-scan setup. *Optics Express*, 22(9):10181, 2014.
- [23] Esmeraldo Escoto, Ayhan Tajalli, Tamas Nagy, and Günter Steinmeyer. Advanced phase retrieval for dispersion scan: a comparative study. *Journal of the Optical Society of America B*, 35(1):8, jan 2018.
- [24] Graham R. Fleming and Mark A. Ratner. Grand challenges in basic energy sciences. *Physics Today*, 61(7):28–33, jul 2008.
- [25] Hans Jakob Wörner, Christopher A. Arrell, Natalie Banerji, Andrea Cannizzo, Majed Chergui, Akshaya K. Das, Peter Hamm, Ursula Keller, Peter M. Kraus, Elisa Liberatore, Pablo Lopez-Tarifa, Matteo Lucchini, Markus Meuwly, Chris Milne, Jacques-E. Moser, Ursula Rothlisberger, Grigory Smolentsev, Joël Teuscher, Jeroen A. van Bokhoven, and Oliver Wenger. Charge migration and charge transfer in molecular systems. *Structural Dynamics*, 4(6):061508, nov 2017.
- [26] Ahmed H. Zewail. Femtochemistry: Atomic-Scale Dynamics of the Chemical Bond. *The Journal of Physical Chemistry A*, 104(24):5660–5694, jun 2000.



- [27] A. Wirth, M. Th Hassan, I. Grguraš, J. Gagnon, A. Moulet, T. T. Luu, S. Pabst, R. Santra, Z. A. Alahmed, A. M. Azzeer, V. S. Yakovlev, V. Pervak, F. Krausz, and E. Goulielmakis. Synthesized light transients. *Science*, 334(6053):195–200, 2011.
- [28] F. Reiter, U. Graf, E. E. Serebryannikov, W. Schweinberger, M. Fiess, M. Schultze, A. M. Azzeer, R. Kienberger, F. Krausz, A. M. Zheltikov, and E. Goulielmakis. Route to attosecond nonlinear spectroscopy. *Physical Review Letters*, 105(24):1–4, 2010.
- [29] Michael Chini, Kun Zhao, and Zenghu Chang. The generation, characterization and applications of broadband isolated attosecond pulses. *Nature Photonics*, 8(3):178–186, 2014.
- [30] Tenio Popmintchev, Ming Chang Chen, Dimitar Popmintchev, Paul Arpin, Su-sannah Brown, Skirmantas Ališauskas, Giedrius Andriukaitis, Tadas Balčiunas, Oliver D. Mücke, Audrius Pugzlys, Andrius Baltuška, Bonggu Shim, Samuel E. Schrauth, Alexander Gaeta, Carlos Hernández-García, Luis Plaja, Andreas Becker, Agnieszka Jaron-Becker, Margaret M. Murnane, and Henry C. Kapteyn. Bright coherent ultrahigh harmonics in the keV x-ray regime from mid-infrared femtosecond lasers. *Science*, 336(6086):1287–1291, 2012.
- [31] S. M. Teichmann, F. Silva, S. L. Cousin, M. Hemmer, and J. Biegert. 0.5-keV Soft X-ray attosecond continua. *Nature Communications*, 7(May):1–6, 2016.
- [32] E. M. Bothschafter, A. Schiffrin, V. S. Yakovlev, A. M. Azzeer, F. Krausz, R. Ernststorfer, and R. Kienberger. Collinear generation of ultrashort UV and XUV pulses. *Optics Express*, 18(9):9173, apr 2010.
- [33] Carlos E. Crespo-Hernández, Boiko Cohen, Patrick M. Hare, and Bern Kohler. Ultrafast Excited-State Dynamics in Nucleic Acids. *Chemical Reviews*, 104(4):1977–2020, apr 2004.

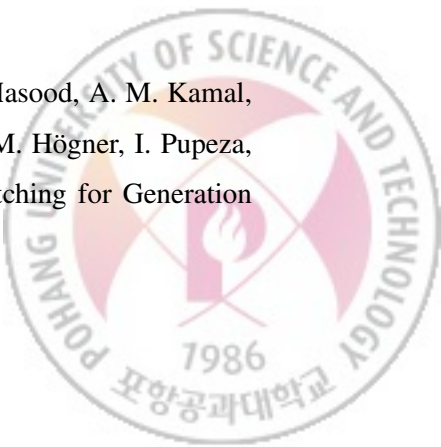


- [34] Thomas Gustavsson, Roberto Imrota, and Dimitra Markovitsi. DNA/RNA: Building Blocks of Life Under UV Irradiation. *The Journal of Physical Chemistry Letters*, 1(13):2025–2030, jul 2010.
- [35] Takao Fuji and Toshinori Suzuki. Generation of sub-two-cycle mid-infrared pulses by four-wave mixing through filamentation in air. *Optics Letters*, 32(22):3330, 2007.
- [36] I Alexeev, a C Ting, D F Gordon, E Briscoe, B Hafizi, and P Sprangle. Characterization of the third-harmonic radiation generated by intense laser self-formed filaments propagating in air. *Optics letters*, 30(12):1503–1505, 2005.
- [37] Charles G. Durfee, Sterling Backus, Henry C. Kapteyn, and Margaret M. Murnane. Intense 8-fs pulse generation in the deep ultraviolet. *Optics Letters*, 24(10):697, 1999.
- [38] Federico Belli, Amir Abdolvand, John C. Travers, and Philip St. J. Russell. Highly efficient deep UV generation by four-wave mixing in gas-filled hollow-core photonic crystal fiber. *Optics Letters*, 44(22):5509, 2019.
- [39] U. Graf, M. Fieß, M. Schultze, R. Kienberger, F. Krausz, and E. Goulielmakis. Intense few-cycle light pulses in the deep ultraviolet. *Optics Express*, 16(23):18956, 2008.
- [40] Mara Galli, Vincent Wanie, Diogo Pereira Lopes, Erik P. Måansson, Andrea Trabattoni, Lorenzo Colaizzi, Krishna Saraswathula, Andrea Cartella, Fabio Frassetto, Luca Poletto, François Légaré, Salvatore Stagira, Mauro Nisoli, Rebeca Martínez Vázquez, Roberto Osellame, and Francesca Calegari. Generation of deep ultraviolet sub-2-fs pulses. *Optics Letters*, 44(6):1308, 2019.
- [41] Maxim V Ammosov, Nikolai B Delone, and Vladimir P Krainov. Tunnel Ionization Of Complex Atoms And Atomic Ions In Electromagnetic Field. In John A.



Alcock, editor, *High Intensity Laser Processes*, volume 0664, pages 138 – 141. International Society for Optics and Photonics, SPIE, 1986.

- [42] A. Couairon, E. Brambilla, T. Corti, D. Majus, O. De, and M. Kolesik. Practitioner's guide to laser pulse propagation models and simulation. *European Physical Journal: Special Topics*, 199(1):5–76, 2011.
- [43] P M Paul, E S Toma, P Breger, G Mullot, F Augé, Ph. Balcou, H G Muller, and P Agostini. Observation of a train of attosecond pulse from high harmonic generation. *Science*, 292(June):1689–1692, 2001.
- [44] T. T. Luu, M. Garg, S. Yu. Kruchinin, A. Moulet, M. Th Hassan, and E. Goulielmakis. Extreme ultraviolet high-harmonic spectroscopy of solids. *Nature*, 521(7553):498–502, 2015.
- [45] Shambhu Ghimire and David A. Reis. High-harmonic generation from solids. *Nature Physics*, 15(1):10–16, 2019.
- [46] Tran Trung Luu, Zhong Yin, Arohi Jain, Thomas Gaumnitz, Yoann Pertot, Jun Ma, and Hans Jakob Wörner. Extreme–ultraviolet high–harmonic generation in liquids. *Nature Communications*, 9(1):1–10, 2018.
- [47] Hung-Wei Sun, Pei-Chi Huang, Yi-Hsuan Tzeng, Jen-Ting Huang, C. D. Lin, Cheng Jin, and Ming-Chang Chen. Extended phase matching of high harmonic generation by plasma-induced defocusing. *Optica*, 4(8):976, 2017.
- [48] M. Lewenstein, Ph Balcou, M. Yu Ivanov, Anne L'Huillier, and P. B. Corkum. Theory of high-harmonic generation by low-frequency laser fields. *Physical Review A*, 49(3):2117–2132, 1994.
- [49] J. Schötz, B. Förg, W. Schweinberger, I. Lontos, H. A. Masood, A. M. Kamal, C. Jakubeit, N. G. Kling, T. Paasch-Colberg, S. Biswas, M. Högner, I. Pupeza, M. Alharbi, A. M. Azzeer, and M. F. Kling. Phase-Matching for Generation

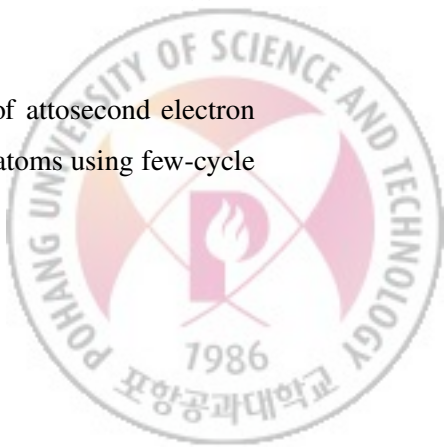


of Isolated Attosecond XUV and Soft-X-Ray Pulses with Few-Cycle Drivers. *Physical Review X*, 10(4):041011, oct 2020.

- [50] Michael Chini, Hiroki Mashiko, He Wang, Shouyuan Chen, Chenxia Yun, Shane Scott, Steve Gilbertson, and Zenghu Chang. Delay control in attosecond pump-probe experiments. *Optics Express*, 17(24):21459, 2009.
- [51] M. Sabbar, S. Heuser, R. Boge, M. Lucchini, L. Gallmann, C. Cirelli, and U. Keller. Combining attosecond XUV pulses with coincidence spectroscopy. *Review of Scientific Instruments*, 85(10), 2014.
- [52] F. Schlaepfer, M. Volkov, N. Hartmann, A. Niedermayr, Z. Schumacher, L. Gallmann, and U. Keller. Phase stabilization of an attosecond beamline combining two IR colors. *Optics Express*, 27(16):22385, aug 2019.
- [53] M. Huppert, I. Jordan, and H. J. Wörner. Attosecond beamline with actively stabilized and spatially separated beam paths. *Review of Scientific Instruments*, 86(12), 2015.
- [54] M. U. Wehner, M. H. Ulm, and M. Wegener. Scanning interferometer stabilized by use of Pancharatnam's phase. *Optics Letters*, 22(19):1455, 1997.
- [55] David W. Chandler and Paul L. Houston. Two-dimensional imaging of state-selected photodissociation products detected by multiphoton ionization. *The Journal of Chemical Physics*, 87(2):1445–1447, 1987.
- [56] André T.J.B. Eppink and David H. Parker. Velocity map imaging of ions and electrons using electrostatic lenses: Application in photoelectron and photofragment ion imaging of molecular oxygen. *Review of Scientific Instruments*, 68(9):3477–3484, 1997.
- [57] N. G. Kling, D. Paul, A. Gura, G. Laurent, S. De, H. Li, Z. Wang, B. Ahn, C. H. Kim, T. K. Kim, I. V. Litvinyuk, C. L. Cocke, I. Ben-Itzhak, D. Kim, and M. F.

Kling. Thick-lens velocity-map imaging spectrometer with high resolution for high-energy charged particles. *Journal of Instrumentation*, 9(5), 2014.

- [58] Y. Huismans, A. Gijsbertsen, A. S. Smolkowska, J. H. Jungmann, A. Rouzée, P. S.W.M. Logman, F. Lépine, C. Cauchy, S. Zamith, T. Marchenko, J. M. Bakker, G. Berden, B. Redlich, A. F.G. Van Der Meer, M. Yu Ivanov, T. M. Yan, D. Bauer, O. Smirnova, and M. J.J. Vrakking. Scaling laws for photoelectron holography in the midinfrared wavelength regime. *Physical Review Letters*, 109(1):1–5, 2012.
- [59] C. Figueira De Morisson Faria and A. S. Maxwell. It is all about phases: Ultrafast holographic photoelectron imaging. *Reports on Progress in Physics*, 83(3), 2020.
- [60] Xue-Bin Bian and André D. Bandrauk. Attosecond Time-Resolved Imaging of Molecular Structure by Photoelectron Holography. *Physical Review Letters*, 108(26):263003, jun 2012.
- [61] Marko Haertelt, Xue Bin Bian, Michael Spanner, André Staudte, and Paul B. Corkum. Probing Molecular Dynamics by Laser-Induced Backscattering Holography. *Physical Review Letters*, 116(13):1–6, 2016.
- [62] Diego G. Arbó, Kenichi L. Ishikawa, Klaus Schiessl, Emil Persson, and Joachim Burgdörfer. Intracycle and intercycle interferences in above-threshold ionization: The time grating. *Physical Review A - Atomic, Molecular, and Optical Physics*, 81(2):3–6, 2010.
- [63] Sebastián D. López and Diego G. Arbó. Holographic interference in atomic photoionization from a semiclassical standpoint. *Physical Review A*, 100(2):1–11, 2019.
- [64] Mitsuko Murakami and Guo Ping Zhang. Observation of attosecond electron dynamics in the photoelectron momentum distribution of atoms using few-cycle laser pulses. *Physical Review A*, 101(5):53439, 2020.



- [65] Ming Hu Yuan, André D. Bandrauk, and Xue Bin Bian. Exploring recollision of ultrafast electrons from photoelectron momentum distributions using single-cycle near-infrared laser pulses. *Physical Review A*, 103(1):1–9, 2021.
- [66] S. Borbély, A. Tóth, D. G. Arbó, K. Tokési, and L. Nagy. Photoelectron holography of atomic targets. *Physical Review A*, 99(1):1–12, 2019.
- [67] L Lehr, T Horneff, R Weinkauf, and E W Schlag. System for Nonresonant Down-hill Charge Transfer in Peptides. pages 8074–8080, 2005.
- [68] Siegfried Lünnemann, Alexander I. Kuleff, and Lorenz S. Cederbaum. Ultra-fast charge migration in 2-phenylethyl-N,N-dimethylamine. *Chemical Physics Letters*, 450(4-6):232–235, 2008.



Acknowledgements

First and foremost, I want to express my gratitude to Prof. Dong Eon Kim, my supervisor, for providing me with the opportunity to learn and conduct research and development in a world-class facility. I'm also grateful for his advice and supervision, as well as his encouragement and support during my PhD studies at POSTECH.

I would like to thank Chul Hoon Kim, Myeongkee Park, and Hyungkook Kim for their contributions to the beamline's construction and various characterization experiments. Without their help, constructing such a large beamline would have been impossible. Many thanks also go to Yunman Lee, who helped with the design of many parts of the beamline and was always willing to assist with any technical issues that arose.

Special thanks go to Alexander Gliserin for his collaboration and support with the implementation of the active phase stabilization for pump-probe experiments. He also taught me a lot about Labview programming. Without his expertise in Labview programming, every experiment in the lab would have been delayed.

Je Hoi Mun's contributions to the third-order harmonic generation experiment, as well as his fruitful discussions and theoretical support on laser-matter interactions, are greatly appreciated. I'm also grateful to Xuanyang Lai, one of our collaborators, for providing us with theoretical support for the photoelectron holography experiments.

Of course, it is impossible not to mention Alexis Chacon's friendly, fascinating, and enlightening physics discussions, as well as his scientific motivation for me.

Soo Hoon Chew (Casey) is also to be thanked for her wonderful, supportive, and healthy lifestyle discussions. In addition, she is a fantastic event planner. Her events always run smoothly and flawlessly. I'm also grateful to Kyungyoung Park (Benjamin) and Jeho Shim for their friendship and endless conversations about everything. Thanks to my colleagues; Yeon Lee, Sungho Choi, Jaeuk Heo, Meenkyo Seo, and other members, for always making the atmosphere in the lab and outside pleasant for me.

Once again, I would like to express my gratitude to Alexander Gliserin and Soo Hoon Chew for their meticulous proofreading and helpful suggestions on the manuscript.

Last but not least, I want to express my gratitude to my friends and family members for their unwavering love and support throughout my PhD studies. Finally, I'd like to thank my wife Tsedennyam for her unwavering support, as well as my daughter Misheelt-Od, who brings me joy and happiness in my life.



Curriculum Vitae

Name: Tsendsuren Khurelbaatar

Birthplace: Uvs province, Mongolia

Education

2014. 09. – 2021. 07. Ph.D. in Physics, POSTECH

2009. 09. – 2011. 06. M.Sc. in Physics, National University of Mongolia

2005. 09. – 2009. 06. B.S. in Physics, National University of Mongolia

Experience

2014. 01. – 2014. 06. Construction and operation of home-made femtosecond oscillator

2014. 09. – 2016. 02. Supercontinuum generation and ultrashort pulse characterization

2016. 03. – 2017. 03. CEP measurements and stabilization after supercontinuum generation output

2017. 01. – 2018. 01. High-order harmonic generation and characterization



2018. 01. – 2020. 01. Constructing an actively phase-stabilized, continuous scan double-layer interferometer with attosecond precision for ultrafast spectroscopy
2018. 03. – 2019. 09. Generation of high-contrast, intense single-cycle pulses using multiple thin plates
2014. 09. – 2021. 01. Development of an attosecond chemical physics beamline



Publication list

1. **Tsendsuren, K.**, A. Gliserin, J. H. Mun, J. Heo, L. Y. Man, and D. E. Kim, Realization of a continuously phase-locked few-cycle deep-UV/XUV pump-probe beamline with attosecond precision for ultrafast spectroscopy. *Applied Sciences* 2021, 11 (15), 6840.
2. **Tsendsuren, K.**, Mun. J., Heo. J., Lee. Y., Kim, D. Few-Cycle, μ J-Class, Deep-UV Source from Gas Media. *Applied Sciences* 2021, 11 (14), 6440.
3. **Tsendsuren, K.**, XuanYang Lai *et.al*, and D. E. Kim , (provisionally entitled) Control of rescattering electron wavepacket with few-cycle laser. 2021, (In preparation).
4. J. Heo, B. Kim, M. Klaiber, **K. Tsendsuren**, H. Christoph, K. Z. Hatsagortsyan, and D. E. Kim, "Quantum diffraction signatures at recollisions in strong field ionization with few-cycle laser pulses", 2021 (to be submitted).
5. Seo, M.; **Tsendsuren, K.**; Mitra, S.; Kling, M.; Kim, D. High-contrast, intense single-cycle pulses from an all thin-solid-plate setup. *Optics Letters* 2020, 45 (2), 367.



© Copyright

”I hereby grant Pohang University of Science and Technology (POSTECH) the right
to make use of my thesis/dissertation for scholarly and educational purposes.”



